Biochemical and Structural Studies of NRBF2: a Critical Autophagy Modulator that Targets the Beclin1-Vps34 Complex

LI NA

PhD

The Hong Kong Polytechnic University

2020

The Hong Kong Polytechnic University

Department of Applied Biology and Chemical Technology

Biochemical and Structural Studies of NRBF2: a Critical Autophagy Modulator that Targets the Beclin1-Vps34 Complex

LI NA

A thesis submitted in partial fulfilment of the requirements

for the degree of Doctor of Philosophy

October 2019

CERTIFICATE OF ORIGINALITY

I hereby declare that this thesis is my own work and that, to the best of my knowledge and belief, it reproduces no material previously published or written nor material which has been accepted for the award of any other degree or diploma, except where due acknowledgement has been made in the text.

Li Na (Signed)

(Name of student)

Abstract

Nuclear receptor binding factor 2 (NRBF2) is a critical modulator of the mammalian class III phosphatidyl-inositol-3 kinase (PI3KC3) complex I. Core members of this complex include the phosphatidyl-inositol-3 kinase Vps34, the serine/threonine kinase Vps15, the scaffolding protein Beclin1 and the Beclin1-binding autophagy enhancer Atg14L. Studies have shown that NRBF2 binds to complex I and promotes cellular autophagic response by enhancing the lipid kinase activity of Vps34. How NRBF2 specifically interacts with complex I but not the UVRAG-containing complex II to promote Vps34-mediated autophagy process is not clear. Here we have conducted biochemical and structural studies of the NRBF2 coiled-coil (CC) domain to elucidate the molecular mechanism of NRBF2-mediated autophagy modulation.

We have determined the crystal structure of NRBF2 CC domain. The structure reveals two helices wrapped around each other in parallel fashion, conforming to the architecture of a canonical coiled-coil dimer. The dimer interface contains multiple leucine-zipper pairings, rendering the dimeric structure highly stable. This structure is in stark contrast to that observed in Atg38, the yeast homolog of NRBF2. The CC domain of Atg38 is an asymmetric dimer, with only one helix being straight and the other bent in the middle. The dimer interface of Atg38 CC domain also contains multiple electrostatically repulsive pairings, likely rendering this structure less stable. It has been reported that Atg38 dimer is only associated with one copy of complex I

while NRBF2 can link two copies to form a large dimeric complex. This difference in stoichiometry for NRBF2- or Atg38-associated complex I may be due to the differential stability of their respective CC domain.

We also conducted a series of cell-based experiments to delineate how the oligomeric state of NRBF2 as determined by its CC domain affects its function in autophagy modulation. Our competitive Co-IP experiments confirm that the CC domain of NRBF2 is not responsible for its specific association with complex I. Instead, the MIT domain of NRBF2 and the C2 domain of UVRAG bind to Vps15 in competitive manner. As a result, NRBF2 can only associate with Atg14L-containing complex I, but not UVRAG-containing complex II.

Additionally, by making mutations and substitutions within the CC domain, we engineered NRBF2 constructs that would adopt monomeric, dimeric and tetrameric state respectively. Co-IP experiments confirm that monomeric NRBF2 is the least competitive against UVRAG in terms of binding to Vps15. Dimeric and tetrameric constructs are noticeably more competitive and help to promote the formation of complex I. Furthermore, in terms of rescuing autophagy activity in NRBF2 knockout cells, monomeric construct is also the least effective while dimeric and tetrameric constructs lead to full recovery and even enhancement of the autophagy activity.

In summary, my thesis work has provided biochemical and structural information

to help understand the functional role of NRBF2 in autophagy regulation. The CC domain of NRBF2 exerts positive influence on complex I by mediating its oligomeric state and promoting its competitiveness against UVRAG-containing complex II. Collectively, these two effects may lead to enhanced activity of complex I to up-regulate the autophagy process.

Acknowledgement

I would like to express my deepest thankfulness to my supervisor Prof. Zhao Yanxiang for her guidance, support, and encouragement during these years. Before joining our lab, my research background about biology was limited, and I was unconfident to pursue a biological Ph.D. degree as a transdisciplinary researcher. Thanks a lot for giving me the opportunity of studying in the lab. Prof. Zhao is glad to communicate with us no matter in research or life. Her patience, creativity, and enthusiasm for science impressed me deeply, and I appreciate what I have learned from her.

Then I want to thank all lab members in Prof. Zhao's lab. Thanks Dr. Li Xiaohua, for her guidance when I entered into the lab and also her preliminary study on NRBF2 project; thanks Dr. Pan Xuehua, for his help in solving the crystal structure; thanks Dr. Wu Shuai, for his guidance in cell assays; thanks Dr. Qiu Xianxiu, Ms. Zhang Xiaozhe and Ms. Yangxian, for your companion and support in my study and life; thanks Ms. Zhang Shuqi and Ms. Chen Jingyi, for dealing with lab routine work. It's really lucky for me to meet all of you, and I will treasure our friendship forever.

I would like to thank Prof. Yue Zhenyu (Mount Sinai School of Medicine) for his preliminary research on NRBF2; thank Prof. Lu Jiahong (University of Macau) for providing N2a WT and NRBF2 KO cell lines. Thanks a lot for your generous support

for my project.

Last, I have to appreciate my dear parents and my elder brother. Thanks a lot for your endless caring and love to support me to pursue my dream.

Table of contents

List of figures and tables

Figures

Tables

Abbreviations

Atg	Autophagy-related gene
β-ME	β-Mercaptoethanol
CCD	Coiled-coil domain
CD	Circular dichroism
Co-IP	Co-immunoprecipitation
E. coli	*Esherichia coli*
EBSS	Earle's Balanced Salt Solution
ER	Endoplasmic reticulum
EM	Electron microscope
FBS	Fetal Bovine Serum
GST	Glutathione-S-transferase
GFP	Green fluorescent protein
HEK293	Human embryonic kidney 293
His	Histidine
IPTG	Isopropyl- β -D thio-galactopyranoside
ITC	Isothermal Titration Calorimetry
LB	Lysogeny broth
LC3	Microtubule-associated protein 1A/1B-light chain 3
LS	Light scattering
L-CPL	Left-handed circularly polarized light

Mw	Molecular weight
MS	Mass spectrometry
MR	Molecular replacement
MIR	Multi isomorphous replacement
MEF	Mouse embryonic fibroblast
MAD	Multiwavelength anomalous diffraction
NRBF2	Nuclear Receptor Binding Factor 2
NMR	Nuclear magnetic resonance
N2a	Neuro-2a
PCR	Polymerase chain reaction
PMSF	Phenylmethanesulfonyl fluoride
PFA	Paraformaldehyde
PBS	Phosphate buffered saline
R-CPL	Right-handed circularly polarized light
SDS-PAGE	Sodium dodecyl sulfate polyacrylamide gel electrophoresis
SEC	Size exclusion chromatography
Sumo	Small ubiquitin-like modifier
SeMet	Selenomethionine
Tris	Tris (hydroxymethyl) aminomethane
Trx	Thioredoxin
UV	Ultraviolet
UVRAG	UV radiation resistance associated gene

Vps	Vacuolar protein sorting
WT	Wild type

Chapter 1: Introduction

1.1 Autophagy is a lysosome-dependent cellular catabolic process serving a plethora of functions

Autophagy is a highly conserved metabolic process that degrades and recycles cellular components through the lysosomal pathway. There are three types of autophagy in mammals: microautophagy, chaperone-mediated autophagy, and macroautophagy (Kiffin *et al.*, 2006). Among these three processes, macroautophagy (hereafter called autophagy) has been investigated most extensively and is the emphasis of this study.

The autophagy process can be divided into five steps, namely, initiation, elongation, autophagosome formation, fusion with lysosome and degradation (Figure 1.1). Firstly, autophagy is initiated in response to cellular stimuli such as starvation or hypoxia. Isolated membrane from endoplasmic reticulum, Golgi apparatus or mitochondrial become nucleated to form cup-like structure termed phagophore. As the phagophore extends and elongates, it begins to engulf cytoplasmic material including misfolded protein, invaded pathogens and damaged organelles. Subsequently, the extending edges of the cup-shaped phagophores fuse and close to form the double-membraned vesicle termed autophagosome. Newly formed autophagosomes are trafficked through the endocytic system and eventually fuse with lysosomes so that the cargo can be degraded and recycled (Meléndez & Levine, 2009).

Autophagy plays an important role in maintenance of cellular homeostasis. For example, autophagy is essential in clearing misfolded proteins and damaged organelles. Autophagy also facilitate nutrient recycling under starvation to promote cell survival (Mathew *et al.*, 2007). Autophagy dysfunction has been implicated in a variety of diseases including neurodegeneration, infection, inflammation and cancer (White, 2012).

The execution and regulation of autophagy in mammals involve several multi-protein complexes, such as the ULK1 complex, the Beclin1-Vps34 complex, the Atg12–Atg5–Atg16Ll complex and the LC3-phosphotidylethanlamine lipid conjugation system (Nakahira & Choi, 2013). Among these complexes, the Beclin1-Vps34 complex has been recognized as an important role in autophagosome formation and maturation by forming multiple subcomplexes with different binding partners (Wirth *et al.*, 2013). This complex is also the focus of my thesis research.

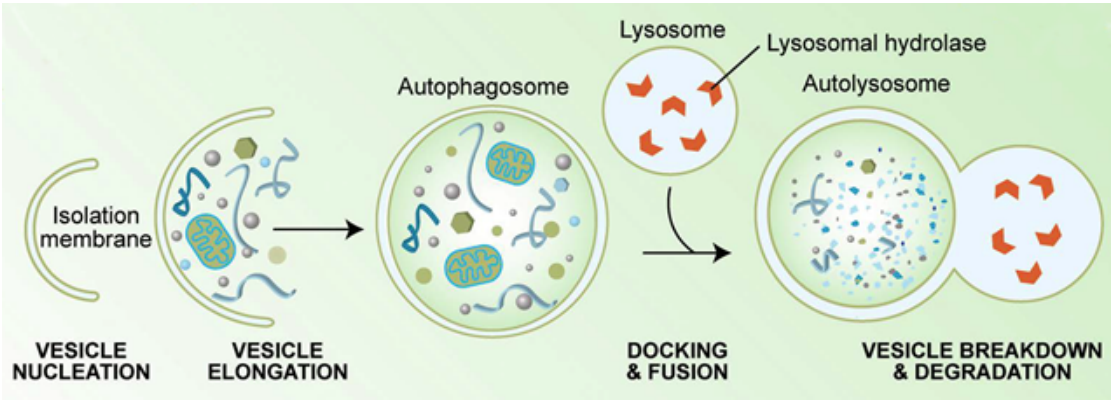

Figure 1.1 Schematic diagram of the autophagy process (Meléndez & Levine, 2009).

1.2 The Beclin1-Vps34 complex is an essential module of the autophagy molecular machinery

While multiple biochemically distinct Beclin1-Vps34 subcomplexes have been identified *in vivo*, all of them contain three invariable core subunits: Vp34, Vps15 and Beclin1 (Figure 1.2A). Vps34, the only identified class III PI 3-kinase, can specifically phosphorylate phosphatidylinositols (PtdIns) to generate phosphatidylinositol 3-phosphates [PtdIns(3)Ps], which are essential to recruit downstream effectors for the nucleation of the phagophore (Jaber & Zong, 2013). Vps15 is the constitutive binding partner of Vps34 and is required for autophagy execution (Anding & Baehrecke, 2014). Beclin1 is also indispensable for the autophagy process. It recruits many cofactors to the Vps34-Vps15 core unit to form many biochemically and functionally distinct Beclin1-Vps34 subcomplexes (Kang *et al.*, 2011). There are two notable examples: Beclin1-Vps34 complex containing Atg14L (PI3KC3 complex I) and Beclin1-Vps34 complex containing UVRAG (PI3KC3 complex II) (Figure 1.2B-C). The PI3KC3 complex I is essential for autophagosome biogenesis at the early stage (Zhong *et al.*, 2009), while complex II facilitates autophagosome maturation at later stages (Kim *et al.*, 2015).

In addition to Atg14L and UVRAG, more than 20 proteins have been identified to bind with Beclin1-Vps34 core complex, some stably and some in transient manner. These proteins, collectively termed 'Beclin1 interactome', interact with Beclin1 to exert regulatory effect on the autophagy process in response to various cellular signals (Kang

et al., 2011).

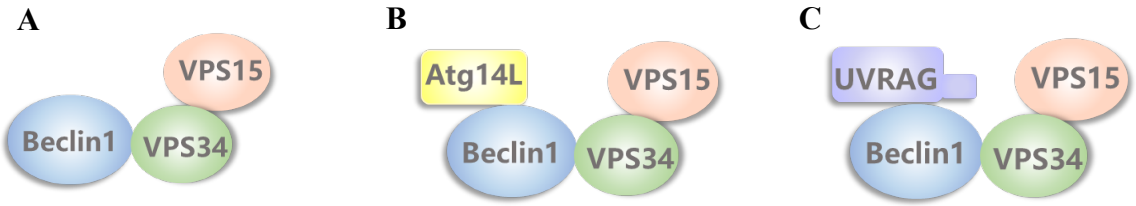

Figure 1.2 Schematic diagram of Beclin1-Vps34 complexes. (A) Three core subunits of Beclin1-Vps34 complexes. (B) The Atg14L containing Beclin1-Vps34 complex: PI3KC3 complex I. (C) The UVRAG containing Beclin1-Vps34 complex: PI3KC3 complex II.

1.3 Structural studies of biochemically distinct Beclin1-Vps34 complexes reveal a common V-shaped architecture

The structural domains of the Beclin1-Vps34 complex components are largely identified (Figure 1.3A). A 4.4 Å crystal structure of the Vps38 (homolog of UVRAG) containing Vps30 (homolog of Beclin1)-Vps34 complex shows that the whole complex is comprised of two arms and a short hook-like base, thus resembling a loosely-connected V shape (Figure 1.3B) (Rostislavleva *et al.*, 2015). The base of the V-shape is formed by the N-termini of Vps30 and Vps38. One arm of the V-shape consists of the kinase domain of Vps15 and the HELCAT domain (helical and kinase domain) of Vps34 tightly packed together. In the other arm the coiled-coil domain (CCD) of Vps30 and Vps38 form an elongated heterodimer and make multiple contacts with Vps15 and Vps34.

The 3D reconstruction model of PI3KC3 complex I obtained by electron microscopy (EM) showed a similar V shape, and its overall conformation and architecture are essentially identical to that of yeast PI3KC3 complex II (Baskaran *et al.*, 2014). Furthermore, EM analysis reveals that the HELCAT domain of Vps34, i.e. one arm of the V-shape, can adopt a range of conformations that resemble large-scale swinging motions relative to the base and other arm of the V-shaped architecture (Figure 1.3C). Such motions suggest that the Beclin1-Vps34 complex is highly dynamic and may fluctuate between the 'open' and 'closed' conformation. The study on the structure of the Beclin1-Vps34 complex is helpful to understand its activity and underlying molecular mechanism.

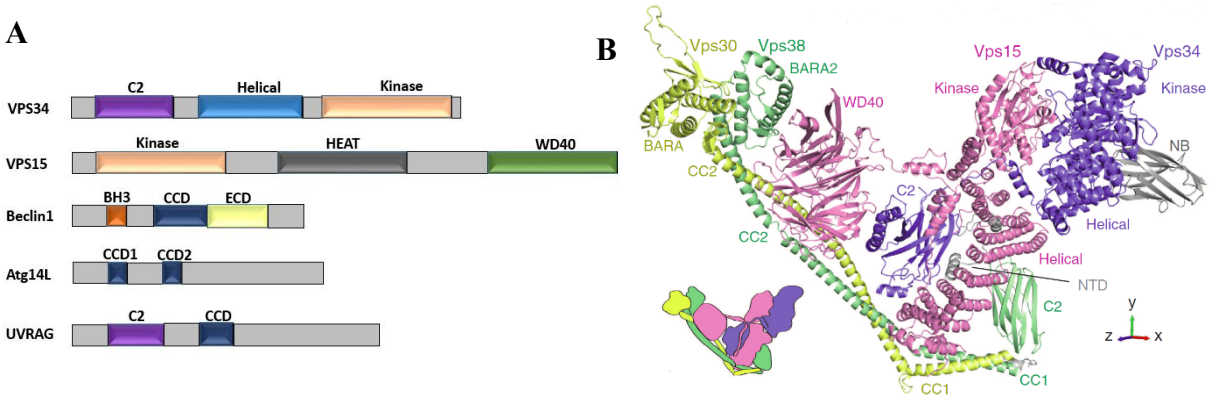

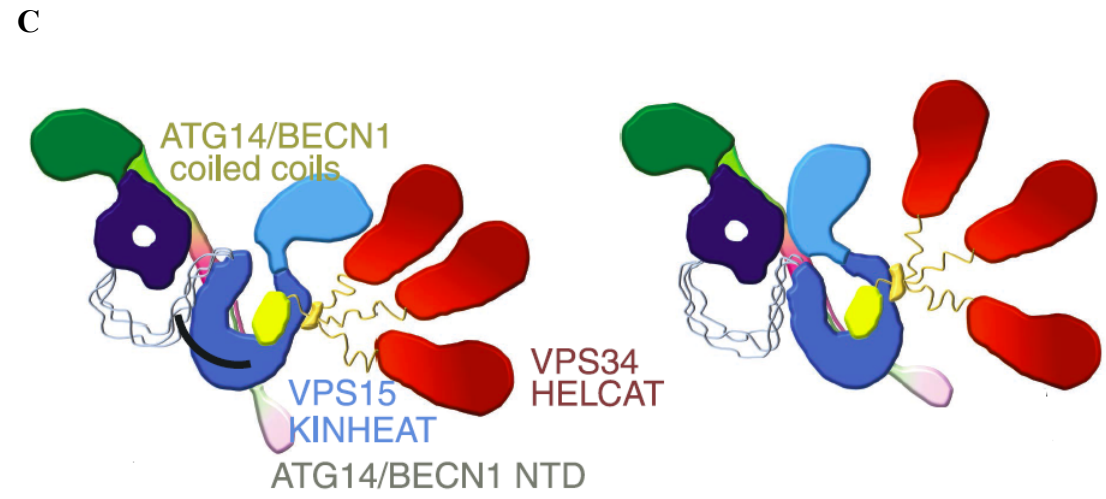

Figure 1.3 Schematic model of the constitution and architecture of the PI3KC3 complexes. (A) Domain structures of proteins in Beclin1-Vps34 complexes. (B) Crystal structure of Vps38 containing Vps30-Vps34 complex, showing the base and two arms (Rostislavleva *et al.*, 2015). (C) Schematic of PI3KC3 complex I describes the pivoting motion of Vps15 KINHEAT and the dynamics of Vps34 HELCAT (Baskaran *et al.*, 2014).

1.4 Nuclear receptor binding factor 2 (NRBF2) is a newly identified component of the Atg14L-containing Beclin1-Vps34 complex I and a positive modulator of autophagy

NRBF2 was initially identified by Takashi Osumi by yeast two-hybrid screening in 1999 (Yasumo *et al.*, 2000). In this study, NRBF2 was identified as the binding partner of peroxisome proliferator-activated receptor K as well as several other nuclear receptors, and the function for NRBF2 was tentatively assigned as the gene activator, when tethered to a heterologous DNA binding domain.

Recently NRBF2 has been identified as an integral component of the Atg14L-containing Beclin1-Vps34 complex I by Co-immunoprecipitation (Co-IP) and liquid chromatography-tandem mass spectrometry (LC-MS/MS) (Zhong *et al.*, 2014,Cao *et al.*, 2014). Additionally, it was reported that the presence of NRBF2 is critical for Atg14L-linked Vps34 lipids kinase activity and autophagy induction. Genetic ablation

of NRBF2 in mouse embryonic fibroblast (MEF) cell line leads to impaired autophagy and increased vulnerability to endoplasmic reticulum (ER) stress. Besides, NRBF2 knockout mice display focal necrosis and ductular reaction in the liver (Lu *et al.*, 2014).

The full-length NRBF2 consists of the N-terminal microtubule-interacting and trafficking (MIT) domain (residue 1-86), an unstructured loop region (residue 87-164) and a C-terminal coiled-coil (CC) domain (residue 165-210) (Figure 1.4 A). As show in Figure 1.4 B, NRBF2 shares low sequence homology with Atg38, the ortholog in yeast, especially in the C-terminal. To date, the structure of MIT domain has been solved (PDB entry 2CRB), showing a three-helix bundle (Figure 1.4 C), while the structure of CC domain remains to be elucidated and the knowledge about the function of NRBF2 is limited. Although the crystal structure of Atg38 C-terminal has been solved (PDB entry 5KC1, Figure 1.4 D), we are curious about the structure of NRBF2 CC domain.

A

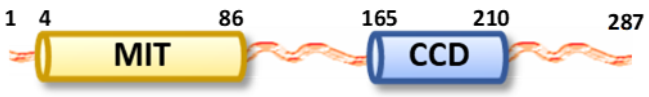

B

```
Yeast Atg38   MSTLAEVYTIIEDAEQECRKGDFTNAKAKYQEAIEVLGPQNENLSQNKLSSDVTQAIDLL 60
Human NRBF2   MEVM---EGPLNLAHQQSRRADRLLAAGKYEEAISCHKKAAAYLSEAMKLTQSEQAHLSL 57
Rat   NRBF2   MEVM---EGPLNLAHQQSRRADRLLAAGKYEEAISCHKKATAYLSEAMKLTQSEQAHLSL 57
Mouse NRBF2   MEVM---EGPLNLAHQQSRRADRLLAAGKYEEAISCHRKATTYLSEAMKLTESEQAHLSL 57
              *.:       :: *.*:.*:.*   * .**:***.        **:    ::  **   *

Yeast Atg38   KQDITAKIQELELLIEKQSS--EENNIGMVNNNMLIGSVIL-NNKSPINGISNARNWDNP 117
Human NRBF2   ELQRDSHMKQLLLIQERWKRAQREERLKAQQNTDKDAAAHLQTSHKPSAE-----DAEGQS 113
Rat   NRBF2   ELQRDSHMKQLLLIQERWKRAKREERLKAQQSTDRDGVPHLQASHRPSED-----SEGQSP 113
Mouse NRBF2   ELQRDSHMKQLLLIQERWKRAKREERLKAQQSTERDGAPHLQAPPRPSED-----AEGQSP 113
              : :  :::::* *: *: .   .*:.:   :..   .   *     *          .

Yeast Atg38   AYQDTLSPINDPLLM---SILNR----LQFNLNN--DIQLKTEGGKNSKNSEMKIN---L 165
Human NRBF2   PLSQKYSPSTEKCLPEIQGIFDRDPDTLLYLLQQKSEPAEPCIGSKAPKDDKTIIEEQAT 173
Rat   NRBF2   LLSQTYIPSTEKRLPEEQGVFDRDPDTLLFLLQQKNEPSEPCIGSKAPKDDKTIIEEQAT 173
Mouse NRBF2   LLSQPYIPSTERRLPEVQGVFDRDPDTLLFLLQQKNEPSEPCIGSKAPKDDKTIIEEQAT 173
                .:   * .:  *    .:::*    * : *::  :      *.*  *:.:  *:

Yeast Atg38   RLEQFKKELVLYEQKKFKEYGM-KIDEITKENKKLANEIGR-----------------L 206
Human NRBF2   KIADLKRH----------VEFLVAENERLRKENKQLKAEKARLLKGPIEKELDVDADFVET 224
Rat   NRBF2   KIAELKRH----------VEFLVAENERLRKENKQLKAEKARLLKGPAEKELDVDADFVEK 224
Mouse NRBF2   KIADLKRH----------VEFLVAENERLRKENKQLKAEKARLLKGTAEKELDVDADFVEK 224
              :: ::*:.          *: : : :.: ****:*  * .*

Yeast Atg38   RE---------------RWDSLVESAKQRRDKQKN------------------------ 226
Human NRBF2   SELWSLPPHAETATASSTWQKFAANTGKAKDIPIPNLPPLDFPSPELPLMELSEDILKGF 284
Rat   NRBF2   SELWGLPPHSDTATASSTWQKFAANTGKAKDIPIPNLPPLDFPSPELPLMELSEDILKGF 284
Mouse NRBF2   SELWGLPSHSESAAASSTWQKFAANTGKAKDIPIPNLPPLDFPSPELPLMELSEDILKGF 284
               *               *:.:. .: : :*

Yeast Atg38   ---  226
Human NRBF2   MNN  287
Rat   NRBF2   MND  287
Mouse NRBF2   MND  287
```

C

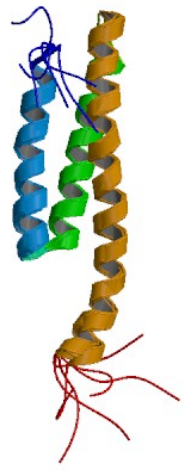

D

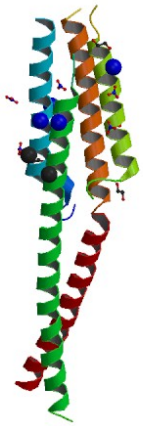

Figure 1.4 Sequence homology and structural similarity between NRBF2 and Atg38. (A) Diagram of the domain structure of NRBF2. (B) Multiple sequence alignment of NRBF2 and Atg38 using Clustal (http://www.ebi.ac.uk/Tools/msa/clustalo/). (C) The structure of NRBF2 MIT domain. (D) The structure of Atg38 N-terminal.

1.5 Objectives

As a newly identified fifth component of the Atg14L-containing Beclin1-Vps34 complex I with implicated physiological role in liver protection, NRBF2 is regarded as a critical modulator of multiple Vps34-dependent membrane trafficking processes including autophagy. However, the molecular details of how NRBF2 binds specifically to the Atg14L-containing complex I but not the UVRAG-containing complex II; and how the recruitment of NRBF2 to complex I leads to elevated autophagic activity is still not clear.

Two recently published studies have provided some useful, although slightly contradictory information on how NRBF2 is incorporated into the Atg14L-containing complex I. The study by Young et. al. (Young *et al.*, 2016) shows that addition of full-length NRBF2 to *in vitro* reconstituted Atg14L-containing complex I leads to the formation of a large NRBF2-complex I assembly with 2: 2 stoichiometry. Additionally, single-particle EM reveals that NRBF2 is positioned at the base of the V-shaped

architecture of complex I. Thus a model of dimeric NRBF2-complex I assembly, with one NRBF2 dimer linking 2 molecules of complex I, was proposed (Figure 1.5 A).

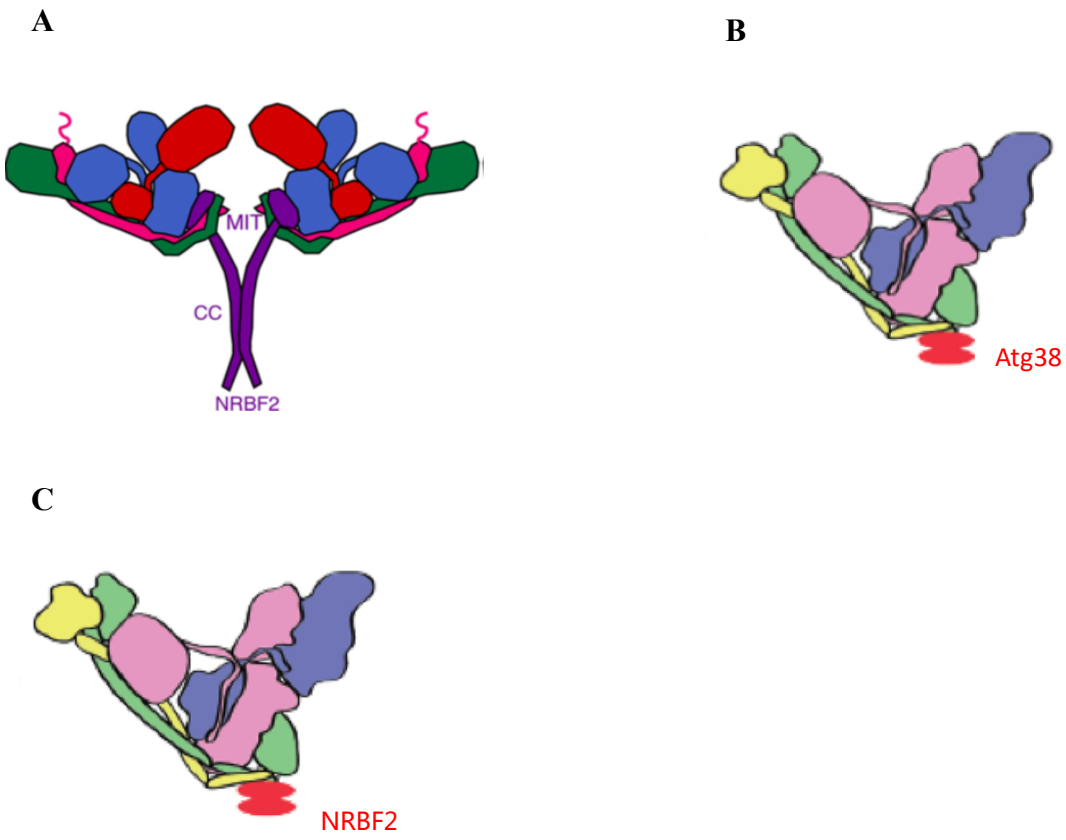

Figure 1.5 Proposed models for NRBF2 containing PI3KC3 complex I. (A) NRBF2 containing PI3KC3 complex I with 2: 2 stoichiometry. One NRBF2 homodimer holds two PI3KC3 complex I together by MIT domains to form a decameric PI3KC3 complex I (Young *et al.*, 2016). (B) Atg38 containing PI3KC3 complex I with 2: 1 stoichiometry. (C) NRBF2 containing PI3KC3 complex I with 2: 1 stoichiometry. One NRBF2 homodimer binds to one PI3KC3 complex I.

The study by Ohashi et. al. (Ohashi *et al.*, 2016) characterized the stoichiometry of both human and yeast complex I, with or without NRBF2/Atg38. Their data show

that in the yeast system, mixing Atg38 with the tetrameric complex I leads to the formation of a larger complex with the stoichiometry of 2: 1, i.e. one Atg38 homodimer is associated with a tetrameric complex I (Figure 1.5 B). In the human system, the stoichiometry of the NRBF2-complex I assembly seems to depend on the abundance of NRBF2. Excessive amount of complex I will favor formation of the NRBF2-complex I assembly with 2: 2 stoichiometry, i.e. similar to the model proposed by Young et. Al (Young *et al.*, 2016). However, if NBRF2 is in excessive, then the resulting NRBF2-complex I assembly can adopt either 2: 2 or 2: 1 stoichiometry (Ohashi *et al.*, 2016). The model of NRBF2-complex I with 2: 1 stoichiometry (Figure 1.5 C) was also proposed by another paper published (Young *et al.*, 2019) after my thesis was prepared, as it was found that NRBF2-MIT homodimer is required for full PI3KC3-C1 activation.

While both studies have proposed models to explain how NRBF2/Atg38 interacts with complex I, neither was able to pinpoint the interaction sites between NRBF2/Atg38 and complex I. The first study used hydrogen–deuterium exchange coupled to mass spectrometry (HDX-MS) and negative-stain electron microscopy single-particle EM analysis to map NRBF2 to the base of the V-shaped complex I (Young *et al.*, 2016). The second study (Ohashi *et al.*, 2016) used similar HDX-MS experiments to show that NRBF2 MIT domain may bridge the CC domains of Atg14L and Beclin1 located on one arm of the V-shaped complex I, thus contradicting the first study. Furthermore, given that HDX-MS experiments were carried out using *in vitro* reconstituted samples, the findings may not apply to the interaction between NRBF2

and complex I *in vivo*.

To further our mechanistic understanding of the NRBF2-complex I assembly and NRBF2-mediated autophagy regulation, we propose to carry out in-depth biochemical and structural studies of NRBF2 to not only evaluate the existing models but also uncover novel aspects of the NRBF2-complex I assembly. Our research objectives are as following:

Objective 1: Characterization of the oligomeric state of NRBF2

Given the importance of NRBF2 homodimer in the proposed models of NRBF2-complex I assembly, we will first characterize the oligomeric state of NRBF2, both *in vitro* and *in vivo*. Both full-length NRBF2 and individual domains will be characterized.

Objective 2: Structural studies of the NRBF2 CC domain

We plan to determine the crystal structure of the NRBF2 CC domain to delineate the molecular details of its coiled-coil interface. This investigation is relevant because the crystal structure of Atg38 CC domain reported by Ohashi et. al. shows an asymmetric homodimer with multiple destabilizing interactions at the interface (Ohashi *et al.*, 2016). As NRBF2 is proposed to dimerize the highly dynamic complex I, a stable CC domain seems more suitable. Our structural study will thus provide the crucial validation.

Objective 3: Biochemical investigation of possible NRBF2-Beclin1 and NRBF2-Atg14L interactions

In the two NRBF2 containing complex I models proposed so far, both Beclin1 and Atg14L have been implicated in direct interaction with NRBF2. However, these two models differ in terms of which specific domains are involved. We plan to conduct thorough biochemical investigation of this important issue. For NRBF2 MIT domain, we will investigate whether it interacts with the N-terminal regions of Beclin1 and Atg14L. For NRBF2 CC domain, we will investigate whether it binds to the coiled-coil regions of Beclin1 and Atg14L.

Objective 4: Cell-based analysis to assess the impact of NRBF2 on complex I *vs.* complex II

NRBF2 specifically associates with the Atg14L-containing Beclin1-Vps34 complex I, but not its mutually exclusive competitor UVRAG-containing complex II. The molecular mechanism of such specificity is not known. We plan to conduct a series of competitive Co-IP experiments to assess how NRBF2 preferably strengthen the assembly of complex I, but not complex II.

Objective 5: Cell-based studies to investigate the functional significance of NRBF2 CC domain in autophagy regulation

Using the biochemical and structural data findings of Objective 1 and 2 as guidance, we will generate NRBF2 constructs with modified CC domain that have either disrupted or strengthened self-oligomerization. The impact of these different oligomeric states on autophagy will be assessed using a series of cell-based autophagy assays and imaging studies.

In summary, we hope our thorough biochemical and structural studies of NRBF2 will provide valuable information to further improve our understanding of NRBF2-mediated autophagy regulation. This study is particularly relevant for the autophagy field because the regulatory strategy employed by NRBF2 may be applicable to the many other recently identified autophagy modulators that also target the Beclin1-Vps34 complex. Our findings may also help to inform future strategies to manipulate autophagy for disease-modifying therapies.

Chapter 2: Methodology

2.1 Cloning

2.1.1 Plasmid construction

Target gene was cloned into certain vector by ligation independent cloning which is comprised of two steps. Firstly, target gene that contains ends with 16~18-base overhanging with the expression vector was created and amplified by polymerase chain reaction (PCR). The 1st round PCR products were purified by agarose gel and then be used as primers for the 2nd round PCR, where responding vector was applied as template. After *DpnI* (a restriction enzyme which digests methylated DNA, Thermo Scientific) digestion at 37°C for 12 hours, the 2nd round PCR products were prepared for later transformation.

2.1.2 Transformation

Transformation refers to the process that exogenous DNA is introduced into cells in a state of competent. The procedure is as follow: PCR products or plasmid and competent cells were mixed with pipette in Eppendorf tube, then the tube was placed on ice for 20-30min. Followed by performing heat shock at 42.5°C for 90s. Next, the tube was transferred on ice again. After adding 500μl LB media (without antibiotic), the competent cell grew in 37°C shaking incubator at 250rpm for 45min-1h. Lastly, competent cells were plated onto LB agar plate which contains corresponding antibiotic and incubated overnight at 37°C.

2.2 Over-expression of recombination protein in *E. coli*

How to obtain soluble target protein is the first challenge in the study of protein structure and function, so the optimization of protein expression system is really critical at the initial stage of this object.

Firstly, parallel small-scale expression was conducted to screen expression conditions, including vectors, temperature and isopropyl β-D-1-thiogalactopyranoside (IPTG) concentration. The procedure of expression is as follow:

① Growing overnight cultures. A single colony that contains recombination vector was picked and then used to inoculate 500μl of LB media (with appropriate antibiotic). The single colony grew in 37°C shaking incubator at 250rpm overnight.

② The overnight cultures were diluted 1: 100, then grew at 37°C for 2-3 hours until OD600 reached 0.6-0.8.

③ IPTG, the commonly used inducer, was added to induce protein expression. The cultures before and after IPTG induction were analyzed by sodium dodecyl sulfate polyacrylamide gel electrophoresis (SDS-PAGE) to test the protein expression level. Different concentration of IPTG (0.1-1mM) and induction temperature (16°C, 30°C, 37°C) were investigated in this step.

④ After induction, cultures were harvested at 6000rpm for 15min. Culture pellets were stored at -80°C.

⑤ The culture pellets were lysed with lysis buffer (in our lab, Tris buffer and His binding buffer were usually used) that freshly added β-Mercaptoethanol (β-ME) and phenylmethanesulfonyl fluoride (PMSF), and then sonicated at 50% amplitude for 20min. Then the sonicated cultures were centrifuged at 12500rpm, 4°C for 25min. The clear supernatant and pellet were analyzed by SDS-PAGE to test the solubility of target protein.

Once the optimized expression system was definite, similar procedure was performed for large-scale expression. Target protein was extracted from harvested cultures by sonication. After centrifuging at 18000rpm for 2 hours, the clear supernatant was filtered with 0.22μm membrane for later purification.

2.3 Purification

2.3.1 Affinity chromatography

Affinity chromatography is the most powerful purification technique to separate target proteins from crude extracts, as it involves the highly specific binding between molecules. In our lab, Ni^{++} affinity column (GE Healthcare) was commonly used in this step, as it has specific binding interaction with recombination protein with His_6-tag,

namely, fusion protein. Once the charge interaction between histidine and nickel was disrupted by imidazole, histidine-tagged recombination protein was eluted out from the column. General purification procedure is as follow:

① Ni^{++} affinity column was washed with 5 column volumes of Milli Q water, followed by 5 column volumes of elution buffer, then equilibrated with at least 5 column volumes of binding buffer.

② The filtered supernatant was loaded on the equilibrated affinity column. For best results, a flow rate of 1ml/min was recommended to use during sample loading.

③ After sample loading, the column was washed with at least 15 column volumes of binding buffer to remove non-specific binding impurities until no material remains in the effluent.

④ The fusion protein was eluted with elution buffer, and protein-containing fractions were collected according to UV absorbance curve. Normally, 5 column volumes of elution buffer are enough for protein elution.

⑤ The eluted fractions were concentrated by centrifugation with a centrifugal filter (Millipore) and then changed into buffer without imidazole to lower the concentration of imidazole.

2.3.2 Removal of fusion tag

To remove fusion tag, protease was applied to cleave the specific site between target protein and fusion tag. The eluted fraction containing fusion protein was added with protease and placed on the roller at 4°C overnight for digestion. Next, the digested sample was reloaded onto affinity column, fusion tag and incomplete digested fusion protein bound with affinity column again while target protein and protease flowed out with washing buffer. Wash fractions were analyzed by SDS-PAGE to control purity and be concentrated for later gel filtration.

2.3.3 Gel filtration chromatography.

Gel filtration chromatography, also known as size-exclusion chromatography, is a chromatography method that separates molecules by their size. The principle of gel filtration chromatography is that smaller molecules are trapped in the pores of porous matrix packed in gel column, which indicates smaller molecules have to through the column by a longer path through pores of beads, while larger molecules pass by the proses easily and flow through the column within a shorter time.

The concentrated sample was applied to a HiLoad 16/600 Superdex 75 pg column (GE Healthcare) and was eluted at 1ml/min by washing buffer. Fractions were collected according to the changes of UV absorbance and all fractions were tested by SDS-PAGE for correct selection of desired protein.

2.3.4 Concentration measurement

① Measuring OD_{280}. Measure the absorbance at 280nm is one of the most usually used approaches to quantify protein, because proteins containing tyrosine and tryptophan have absorbance maxima at 280nm. Since the relationship of absorbance and protein concentration is linear, the concentration of pure protein with known extinction coefficient can be easily calculated according to the measured absorbance.

② Bradford method. Bradford method is based on the phenomenon that maximum absorbance of Coomassie Brilliant Blue G-250 shifts from 465nm and 595nm when the dye binds with protein. According to the standard curve generated from bovine serum albumin with known concentration, the concentration of unknown protein sample can be determined.

2.3.5 Storage of protein

Purified and concentrated protein was divided into small aliquots and frozen in liquid nitrogen, and subsequently stored in -80°C for long term storage.

2.4 Biophysical and biochemical analysis

2.4.1 Mass spectrometry (MS)

Mass spectrometry is a critical and reliable technique for protein structural analysis due to its convenience and sensitivity. Once the target protein with high purity is obtained, mass spectrometry can be used to identify the exact molecular weight of protein. Mass spectrometry can also provide amino acid sequence information of peptides, this application is particularly important in the identification of degraded protein or unknown sample. Furthermore, mass spectrometry is powerful in the analysis of protein modifications, including phosphorylation and ubiquitination (Zhang *et al.*, 2010).

2.4.2 Light scattering

Light scattering is a powerful technique to determine protein size and estimate populations of protein aggregates. When the laser hits protein, the light scatters in different directions, and the intensity of scattering light is unstable, because of the Brownian motion of particles. This technique measures the fluctuation of scattering intensity, so as to calculate the diffusion coefficient of particles and subsequently determine the size distribution (Jachimska *et al.*, 2008). In this project, the size exclusion chromatography-light scattering-UV (SEC-LS-UV) system was employed to detect the oligomeric state of the protein. This system provides a powerful platform to identify the stoichiometry of protein samples through the combination of concentration data provided by UV detector and light scattering signals. The general procedure is as follows: 30-100μg protein was applied to a Superdex 200 10/300 GL column (GE

Healthcare) which had been equilibrated with the buffer that was used to store target protein. The injected volume was about 500μl and the flow rate was 0.5ml/min. The UV absorbance was detected at 280nm while the light scattering signal was measured at 662nm, and the final data were analyzed by software ASTRA (Wyatt technology).

2.4.3 Nuclear magnetic resonance (NMR) spectroscopy

NMR involves in the spin of atom nuclei (Günther, 2013). According to the spin quantum number (I), atom nuclei can be divided into three types: the nucleus with both even numbers of protons and neutrons (I=0, overall spin is zero and NMR inactive); the nucleus with odd mass number (I=1/2, such as ^{1}H, ^{13}C, ^{15}N, ^{31}P); the nucleus with even mass number and odd number of protons and neutrons (I=1, such as ^{14}N). ^{1}H, ^{13}C, ^{15}N are the most important NMR active nuclei in the biochemistry field. When the compound with NMR active nuclei is placed in a strong magnetic field, the tiny magnetic field caused by the spin of nuclei is aligned with or opposed to the strong external magnetic field. The nucleus undergoes the transition from spin aligned state (lower energy level) to spin opposed state (higher energy level) after absorbing energy provided by external electromagnetic radiation with specific resonance frequency. By detecting the absorption signals, an NMR spectrum which can be used to analyze the chemical environment of different nucleus and bonding between nuclei is obtained. Information about the distance between nuclei provides a map for the overall structure of a molecule. Nowadays, NMR has been developed as a powerful technique to

determine the structure of proteins both in liquid and solid states. Furthermore, the NMR study on the dynamics of protein samples in the solution helps to investigate the function of proteins in physiological conditions as well as protein-protein interaction (Hong *et al.*, 2012).

In order to obtain isolable protein with ^{15}N for NMR assay, the bacteria was incubated in M9 minimal media, in which $^{15}NH_4Cl$ was the sole source of nitrogen. 5× M9 salts, $MgSO_4$ and $CaCl_2$ solutions were autoclaved, while glucose and $^{15}NH_4Cl$ solutions were sterilized by filtering with 0.22μm filter before mixing with other components. The colony was picked and incubated in LB media at 37°C for 12 hours, then diluted 1: 100 into 1L M9 minimal media. The bacteria grew in M9 minimal much more slowly than that in LB media, and it took about 12-14 hours to reach OD_{600} of 1.0. Next, 0.8mM IPTG was added to induce protein expression, and 7ml glucose solution together with 1.7ml $^{15}NH_4Cl$ solution were supplemented to provide sufficient nutrient for bacteria growth. After 8 hours induction in 30°C, the bacteria was harvested at 6000rpm for 15min. The purification procedure of ^{15} N-labeled protein is similar to that of normal protein. The recipes of the M9 minimal media and M9 salts are listed below respectively:

M9 minimal media (per liter)	
5× M9 salts	200ml
1M $MgSO_4$	2ml
0.1M $CaCl_2$	1ml
20% Glucose	20ml
20% $N^{15}H_4Cl$	5ml
Sterile H_2O	Up to 1L

M9 salts (5×, per liter)	
$Na_2HPO_4.7H_2O$	64g
KH_2PO_4	15g
NaCl	2.5g
Sterile H_2O	Up to 1L

2.4.4 Circular dichroism (CD) spectroscopy

CD spectroscopy is a commonly used technique to detect the secondary structure of proteins. When circularly polarized light passes through the optical active compound, the absorption of left-handed circularly polarized light (L-CPL: Al) and that of right-handed circularly polarized light (R-CPL: Ad) are different. Measuring the difference in absorption ΔA (Al-Ad) is the basis of CD spectroscopy. A primary application of this technique is to detect the secondary structure of proteins. CD spectra at different wavelengths (from 180nm to 260nm) can be used to analyze different secondary structure types, including alpha helices, beta sheets, and random coils. For example，α-helix contains two negative bottoms at 222nm and 208nm with same intensity and a positive band at 193nm; while a negative bottom at 218nm and a positive peak at 195nm indicates an antiparallel β-sheet; and disordered proteins (random coil) displays very

low ellipticity above 210nm and a negative band around 195nm (Greenfield, 2006). Another application of CD spectroscopy is to observe the conformational changes of proteins with environmental factors (such as pH, temperature and denaturants), so as to identify the physiochemical properties of proteins.

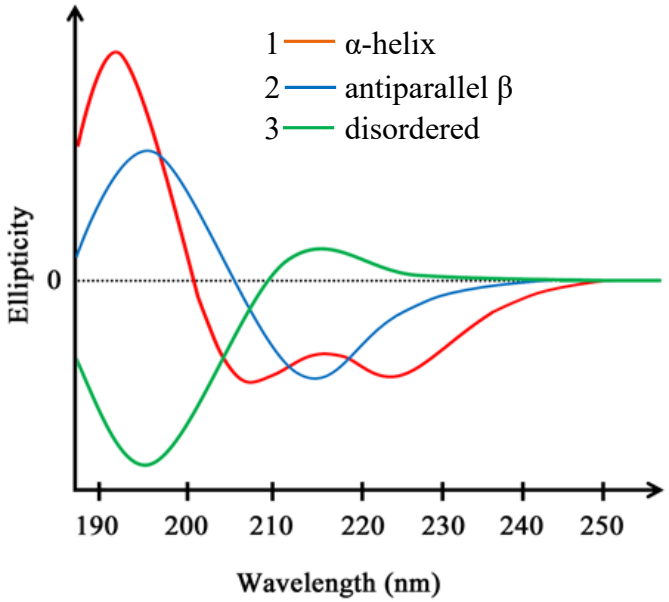

Figure 2.1 CD spectrum of three basic secondary structures of a polypeptide chain (α-helix, β-sheet and random coil).

2.4.5 Isothermal titration calorimetry (ITC)

ITC is a physical technique used to investigate direct molecular interactions quantitatively. By measuring the heat transfer during a molecular binding reaction, a series of binding parameters including enthalpy changes (ΔH), binding affinity (Ka), and stoichiometry (n) can be obtained simultaneously. There are two cells in an

isothermal titration calorimeter, namely, a reference cell which contains water and sample cell. When binding occurs, the heat released or absorbed causes the difference in temperature between these two cells. Heat sensors detect the difference and deliver feedback to activate the heaters, so as to maintain equal temperatures between these two cells. During a practical experiment, the ligand loaded in a syringe is titrated into the sample cell in a predetermined volume and time under the control of an accurate injection device. The heat change that occurs in each injection is measured by the heat sensor and output in the real-time data curve (Figure 2.2). Through software analysis, complete thermodynamic parameters can be obtained from the curve in a single experiment. There are no special requirements such as fluorescent labels or tags for ITC samples, which allows ITC to become a powerful approach to investigate direct interaction between biomolecules and identify binding partners (Pierce *et al.*, 1999).

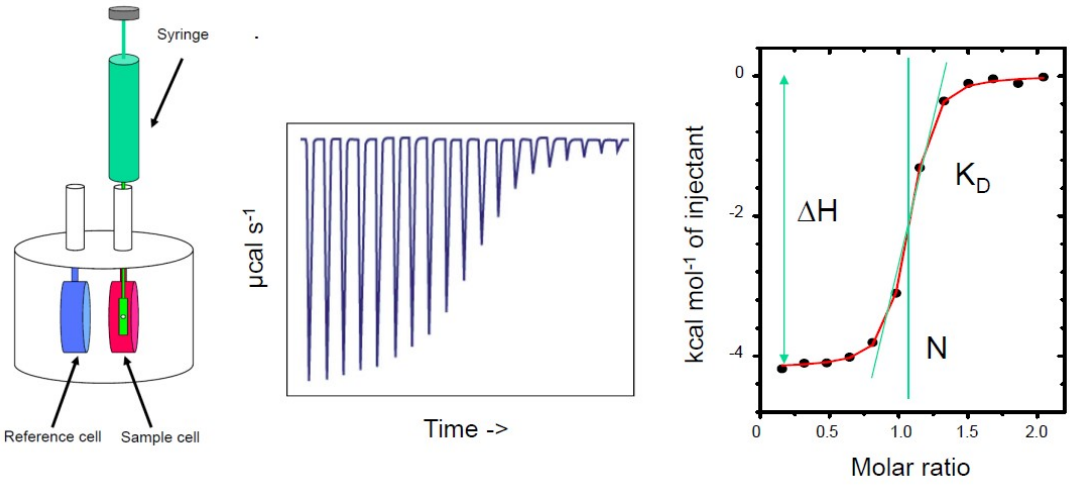

Figure 2.2 Schematic of ITC equipment and the result of a typical ITC experiment. (http://www.malvern.com/)

2.4.6 Pull down

Pull-down assay is a widely used method to determine the physical protein-protein interaction *in vitro*. The principle of pull-down assay involves capturing a 'bait' protein by the immobilized ligands on the beads via affinity tags (e.g., histidine, GST, maltose binding protein, etc.) or antibodies to generate a secondary affinity support, which is subsequently incubated with the 'prey' protein. The 'bait-prey' complex is then analyzed by various approaches, including SDS-PAGE, western blot, and MS, etc., so as to confirm the interaction between the 'bait' protein and the 'prey' protein or discover the potential target proteins.

2.5 X-ray crystallography

X-ray crystallography, NMR and cryo-EM have been widely used to solve the protein structure recently. Among of these techniques, X-ray crystallography is the most commonly used approach with the highest resolution for determining the spatial arrangement of atoms in the crystal. When a beam of X-rays encounters the crystalline atoms, the X-rays are diffracted, as the wavelengths of X-rays are similar to typical interatomic distances. By analyzing the diffracted X-ray, a three-dimensional electron density map in the crystal is obtained. Based on this electron density map, the positions and chemical bonds of atoms in the crystal, namely, the crystal structure can be determined.

2.5.1 Crystallization trials

To obtain a crystal with high quality is the first step of applying X-ray to analyze the structure of the protein. In this project, we used the hanging drop vapor diffusion method for protein crystallization. The general procedure is as follows: 1μl protein solution and 1μl reagent were mixed and then placed on a siliconized coverslip, and the well of a 24-well hanging drop tray was filled with 500μl corresponding reagent to form a larger reservoir. Next, the coverslip was inverted and covered on the vaseline ring around the edge of the well. By gently pressing, the well was sealed completely and the tray was then incubated in 16℃ for crystallization. As the concentration of the reagent in the hanging drop is 1/2 of that in the reservoir, water vapor leaves the drop for the reservoir to achieve equilibrium and then the concentrations of protein and reagent in the drop increase with time. If a suitable crystallization solution is provided, the crystal forms in the hanging drop following 3 steps: the saturation of protein solution, supersaturation and nucleation, crystal growth. Crystal screen kits (Hampton research) which contain various solution conditions (such as different salts, precipitants, and pH) are applied to screen crystallization conditions. Further optimization on crystallization conditions is conducted on the basis of screening results to obtain a crystal with high quality for X-ray diffraction.

2.5.2 Data screen and collection

Subsequently, the single crystal with a certain size (> 0.1mm) was mounted to the

X-ray machine for assessing the crystal quality and optimizing the parameters for data collection such as crystal-to-detector distance, oscillation step, and exposure time. Before mounting the crystal on the machine, cryoprotection is possibly required to avoid the formation of the 'ice-ring' surrounding the crystal if the crystallization solution which the crystal grew from lacks the cryoprotectants. For the initial collection, the crystal-detector distance is adjusted according to the diffraction resolution to make sure neither the diffraction pattern covers the whole detector nor exceed the edge of the detector. The exposure time is associated with the intensities of the diffraction spots, proper exposure time is required for obtaining good signal/noise ratio as well as avoiding the incurrence of radiation damage. In terms of the oscillation step, the range is set at 0.5-1.5°. Once the qualified crystal has been determined after initial screening according to the diffraction pattern and pre-indexing, a whole set of data will be collected for structure determination.

2.5.3 Phasing

After data collection, the raw diffraction data were subsequently processed to improve their consistency for solving the structure following 4 steps: indexing, cell refinement, integration and scaling.

The electron density map is the end result of an X-ray structural determination, and it as a function of position x, y, z is the Fourier transform of the structure factor

F*(hkl)*:

$$\rho(xyz) = \frac{1}{V}\sum_{h}\sum_{k}\sum_{l} |F(hkl)|\exp[-2\pi i(hx + ky + lz)] + i\alpha(hkl).$$

Structure factor amplitude |F*(hkl)*| is proportional to the square root of the measured intensities, while the phase angle α*(hkl)* is missing in the experiment. To solve the phase problem, there are 3 major approaches used in practice: multi isomorphous replacement (MIR) that introducing heavy atoms into crystals, molecular replacement (MR) that deducing the unknown structure by applying the known structure of the homologous protein as initial model, and multiwavelength anomalous diffraction (MAD) by comparing structure factors collected at different wavelengths. In this project, because the structurally similar homolog is not available, we tried to solve the phase problem by MIR and MAD respectively.

For MIR, the heavy atoms are introduced by soaking the crystal in the solution containing heavy metal or co-crystallization. The heavy atom derivatives and the native crystal are isomorphous, as they share the same unit cell parameters and space group. Differences in diffraction intensity between the native and derivative data sets can be used to identify the location of heavy atoms by direct method or Patterson function, so as to determine the structural factors and phase angle.

MAD is a powerful method for determinations of novel biological structures at atomic level based on the phase information provided by anomalous scattering. Heavy

atoms scatter X-rays anomalously at wavelengths near their absorption edges. Comparing the diffraction pattern collected at the wavelength near the absorption edge of the heavy atom and that at a wavelength away from the absorption edge, the phase information can be extracted. The selenomethionine (SeMet) was incorporated into proteins by replacing the sulfur atoms with selenium atoms, which act as strong scatters to produce anomalous signal, so as to solve the phase problem via MAD method.

2.5.4 Model building and refinement

After data processing and phase determination, the initial electron density map was obtained, and then protein sequence was inputted into the electron density map to build the approximate model. The initial model usually contains some errors because of the limited resolution and inaccurate phase, so refinement is required for the improvement. The aim of the refinement is to optimize the structural parameters such as bond length and bond angle, so as to obtain the maximum agreement between the observed diffraction pattern and that calculated by Fourier transformation from the approximate model. Normally multiple cycles of model building -refinement-rebuilding are required. The R-factor (R_{work}) is a measure of the quality of the atomic model obtained after refinement by evaluating the agreement between the simulated diffraction pattern and the experimentally-observed diffraction pattern. While R_{free} is used to assess possible over-interpreting of the data. Unlike R_{work}, R_{free} is calculated from 5% ~ 10% randomly chosen intensities which are not used during refinement.

Normally, R_{free} is slightly higher than R_{work} during intermediate stages of refinement, but these two values should be similar in the final stages, because the correct model should predict all the data with uniform accuracy.

2.6 Cell-based experiments

2.6.1 Co-IP

HEK293T cells were employed for Co-IP assay to investigate the interaction between NRBF2 and other members in the PI3KC3 complex in this project. The procedure of Co-IP assay is as followed: The plasmids were transiently transfected into HEK293T cells at around 60%-70% confluency by using lipofectamine 3000 (Thermo Fisher scientific) according to the protocol provided by the manufacture. After 24-48 hours, the transfected cells were washed by Phosphate buffered saline (PBS) buffer and lysed by extraction buffer (25mM HEPES, pH 7.5, 10mM MgCl2, 150mM NaCl, 1mM EDTA.2Na, 1% Nonidet P-40, 1% Triton X-100 and 2% glycerol) with freshly added protease inhibitor cocktail (Roche). The whole cell lysate was then centrifuged at 10,000rcf for 15min to obtain the supernatant which was subsequently incubated with anti-FLAG magnetic beads (Sigma) overnight at 4°C. The beads were washed with extraction buffer 5 times and then eluted with 20μl 2× Laemmli sample buffer. After boiling for 10min, the samples were loaded in SDS-PAGE and analyzed by western blot.

2.6.2 Confocal

To assess the effects of NRBF2 on regulating autophagy, we used confocal microscope to characterize the co-localization of NRBF2 to LC3 puncta. The HeLa cell stably expressing GFP-LC3 was employed for the imaging study. Briefly, the HeLa cell was cultured in the confocal dish (SPL) by using Dulbecco's Modified Eagle's Medium (DMEM) supplemented with 10% fetal bovine serum (FBS), and penicillin (100U/ml)/streptomycin solution (100μg/ml). Then the plasmids of mCherry vector, mCherry-tagged NRBF2 WT or mutants were transfected respectively into the HeLa cell. After 24-48 hours, the HeLa cells were treated with rapamycin (100nM) for 3 hours for inducing autophagy. Cells were fixed with 4% paraformaldehyde (PFA), washed with PBS 5 times and then observed by the confocal microscope to investigate the colocalization of NRBF2 to GFP-LC3 puncta.

Chapter 3: Characterization of NRBF2 oligomeric state

3.1 Design of NRBF2 constructs for biochemical and structural studies

To facilitate our biochemical and structural studies, we have designed three NRBF2 constructs. NRBF2-FL (residues 4-210) represents almost the full-length NRBF2 protein except for the C-terminal region. NRBF2-MIT (residues 4-86) represents the N-terminal MIT domain and NRBF2-CCD (residues 165-210) represents the C-terminal CC domain. Detailed information for each construct is listed in Table 3.1.

Table 3.1 Three NRBF2 constructs for biochemical and structural studies

Construct	Length	Theoretical molecular weight
NRBF2-FL	4-210	24029.2Da
NRBF2-MIT	4-86	10026.4Da
NRBF2-CCD	165-210	5686.4Da

3.2 Expression and purification of NRBF2 constructs

Briefly, the expression and purification of recombinant NRBF2-FL is as follows: For the expression vector, pETSUMO plasmid with SUMO fusion tag and 6*His affinity tag is used. NRBF2-FL is inserted into ApaI and EcoRI restriction site after the T7 promoter. For the expression protocol, bacteria transfected with pETSUMO-

NRBF2-FL plasmid was incubated at 37°C until OD_{600} reached 0.6-0.8 and, then induced by addition of 0.3mM IPTG. After further incubation at 30°C for 5-6 hours, the bacteria were harvested by centrifugation at 6000rpm for 15min. For the purification process, bacteria pellet was lysed after sonication for 20min at 55% amplitude in the lysis buffer of His binding. The lysate was subject to centrifugation at 20,000rpm for 90 minutes. The supernatant was loaded onto nickel-charged IMAC column and the fusion protein was eluted by using a gradient of 55-500mM imidazole.

Next, desired fractions were mixed, concentrated and changed into Tris buffer (50mM Tris and 150mM NaCl, pH 8.0). After digested by HRV 3C protease at 4℃, the protein was reloaded onto nickel-charged IMAC column, HRV 3C protease and the target protein without fusion tag was washed out by Tris buffer as expected and then centrifuged for later gel filtration purification. As shown in Figure 3.1 C, after gel filtration, NRBF2-FL with high purity was obtained finally.

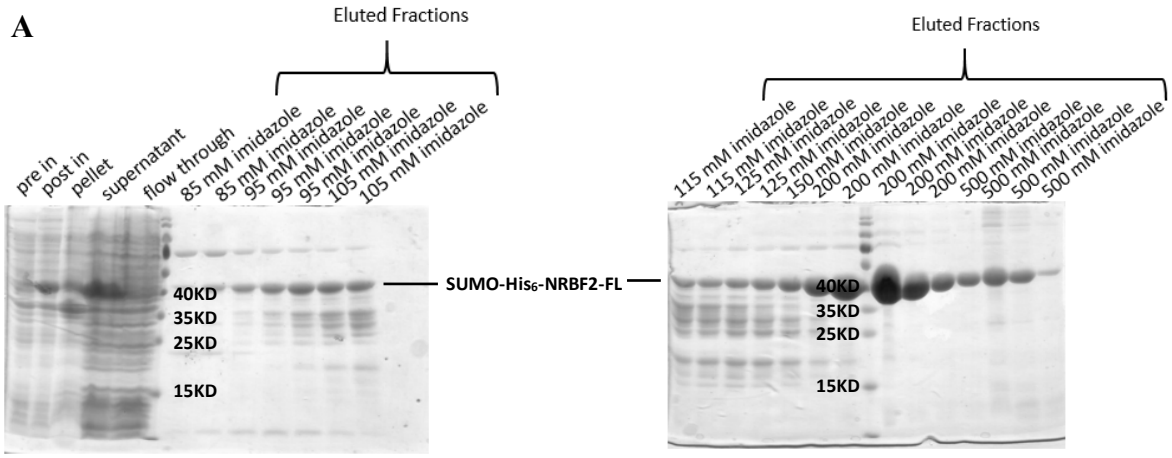

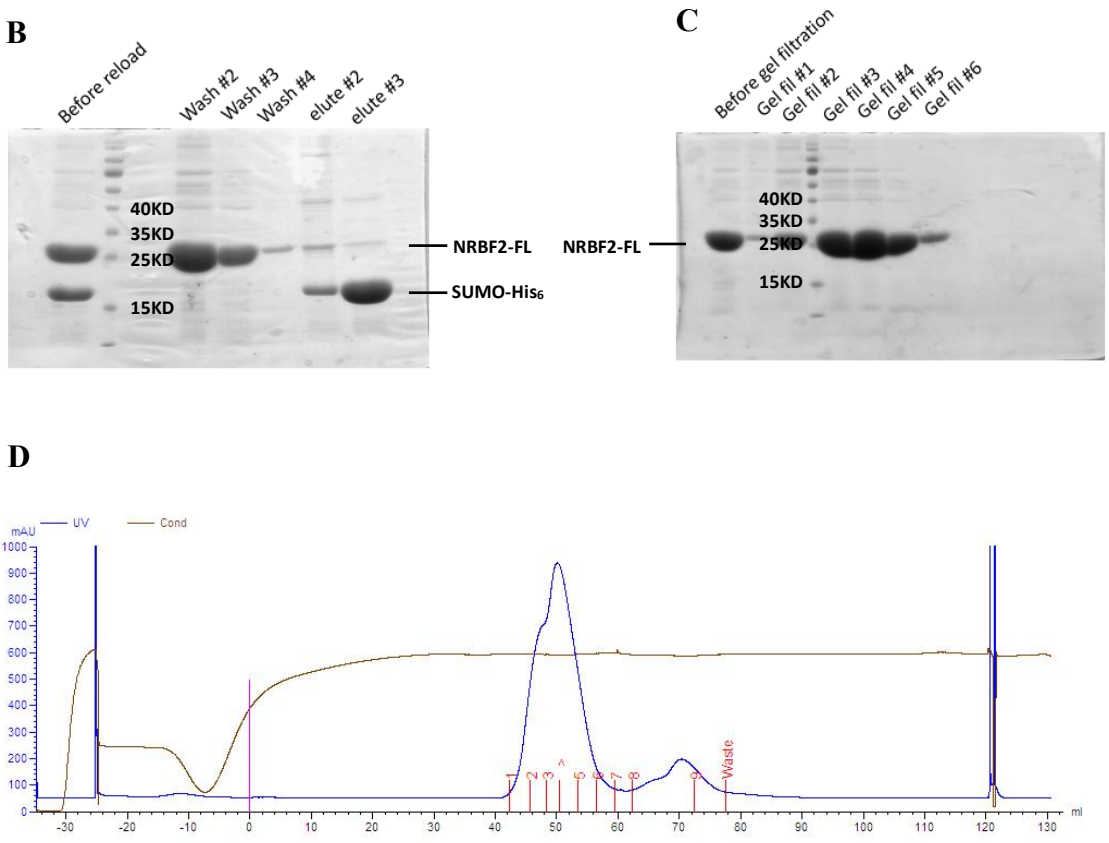

Figure 3.1 The purification of NRBF2-FL. (A) SDS-PAGE to characterize the expression level and purification of NRBF2-FL after affinity chromatography. Pre in: the whole cell lysate before IPTG induction; post in: the whole cell lysate after IPTG induction; pellet: the pellet of cell lysate after centrifugation; supernatant: the supernatant of cell lysate after centrifugation; flow through: the protein didn't bind with affinity column during loading sample. Fusion protein was eluted with a gradient of 55-500mM imidazole. **(**B) SDS-PAGE of NRBF2-FL after removing the fusion tag by HRV 3C protease. Target protein existed in wash fractions, while SUMO tag was eluted by elution buffer. (C) SDS-PAGE of NRBF2-FL after gel filtration. (D) The profile of gel filtration.

Compared with NRBF2-FL, the expression condition of NRBF2-MIT is the same, while there is small difference in purification procedures. The fusion protein was eluted directly with elution buffer rather than gradient concentrations of imidazole (Figure 3.2).

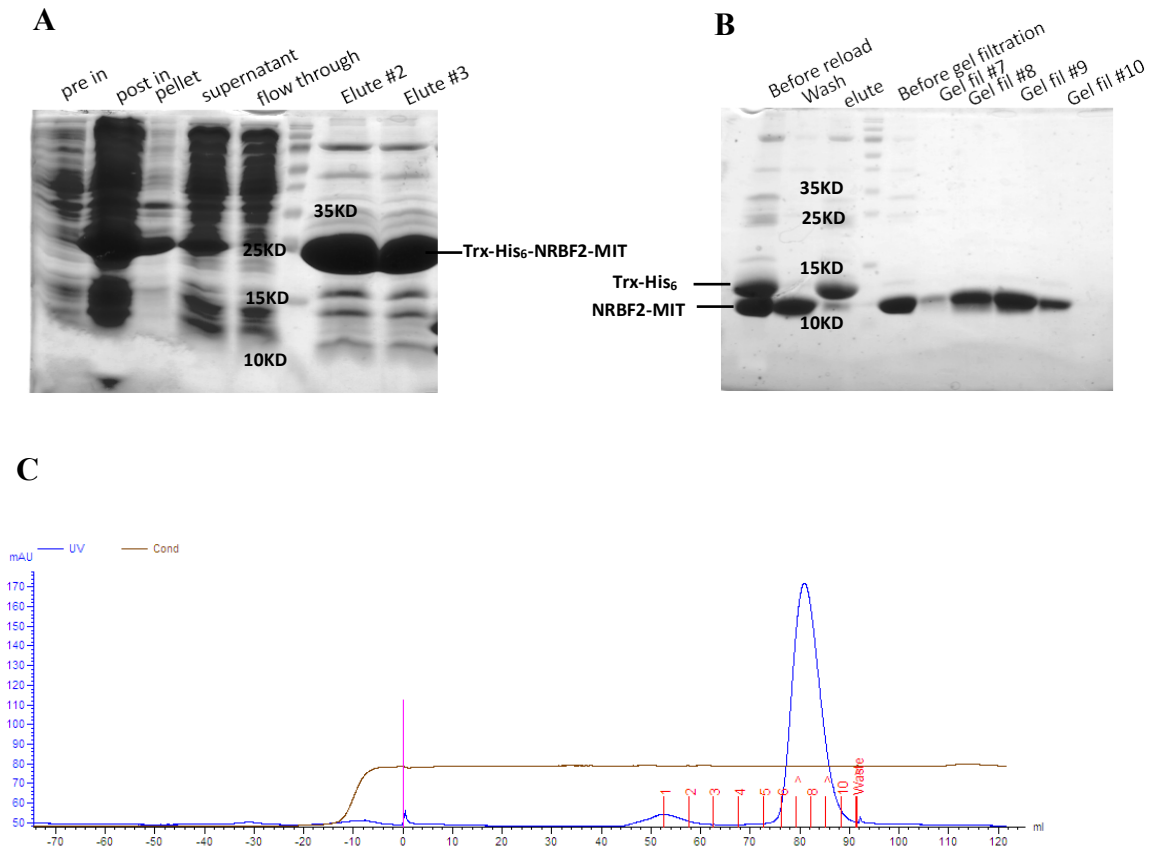

Figure 3.2 The purification of NRBF2-MIT. (A) SDS-PAGE to characterize the expression level and purification of NRBF2-MIT after affinity chromatography. Pre in: the whole cell lysate before IPTG induction; post in: the whole cell lysate after IPTG induction; pellet: the pellet of cell lysate after centrifugation; supernatant: the supernatant of cell lysate after centrifugation; flow through: the protein didn't bind with affinity column during loading sample. Fusion protein was eluted with His elution buffer containing 500mM imidazole. (B) SDS-PAGE of NRBF2-MIT after removing the fusion tag and after gel filtration. The fusion protein Trx-His_6-NRBF2-MIT was

digested by HRV 3C protease and then reloaded onto the nickel-charged IMAC column, NRBF2-MIT flowed out by Tris buffer and existed in wash fractions, while Trx-His_6 tag was eluted by elution buffer. The wash fractions were subsequently concentrated and loaded onto gel column. (C) The profile of gel filtration.

The expression and purification of NRBF2-CCD followed the same procedure as used for NRBF2-MIT. The SDS gels (Figure 3.3) show that the expression level of NRBF2-CCD is high and the solubility is good. It should be noticed that NRBF2 has little UV observance due to the absence of tryptophan, tyrosine and phenylalanine residues. Because of this, the setting for the UV monitor on the FPLC system was adjusted accordingly to detect the weak signal of purified NRBF2-CCD.

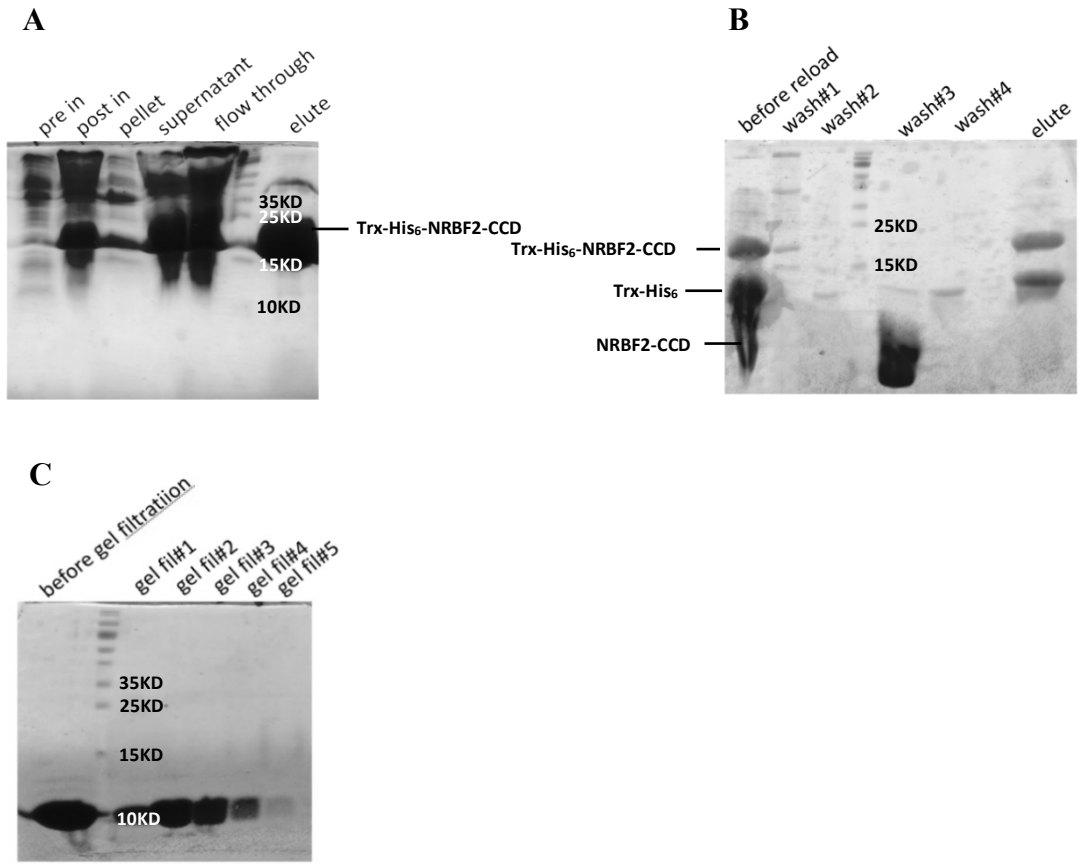

D

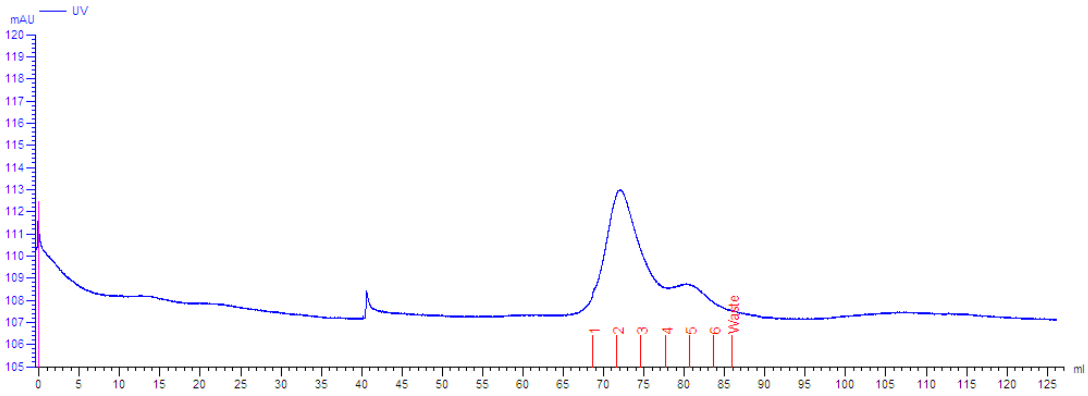

Figure 3.3 The purification of NRBF2-CCD. (A) SDS-PAGE to characterize the expression level and purification of NRBF2-CCD after affinity chromatography. Pre in: the whole cell lysate before IPTG induction; post in: the whole cell lysate after IPTG induction; pellet: the pellet of cell lysate after centrifugation; Supernatant: the supernatant of cell lysate after centrifugation; flow through: the protein didn't bind with affinity column during loading sample. Fusion protein was eluted with His elution buffer containing 500mM imidazole. (B) SDS-PAGE of NRBF2-CCD after removing the fusion tag by HRV 3C protease and then reloaded onto the nickel-charged IMAC column, NRBF2-CCD flowed out by Tris buffer and existed in wash fractions, while Trx-His_6 tag and undigested fusion protein were eluted by elution buffer. The wash fractions were subsequently concentrated and loaded onto gel column. (C) SDS-PAGE of NRBF2-CCD after gel filtration. (D) The profile of gel filtration.

3.3 MS analysis of NRBF2 constructs

After purification, the molecular weights of these NRBF2 constructs were

identified by MS. The mass spectrum shows measured molecular weight of NRBF2-FL, NRBF2-MIT, and NRBF2-CCD are 24031.0Da, 10027.0Da and 5685.0Da respectively, which are nearly equal with their theoretical values (24029.2Da, 10026.4Da and 5686.6Da), suggesting the target proteins with high purify have been obtained (Figure 3.4).

A

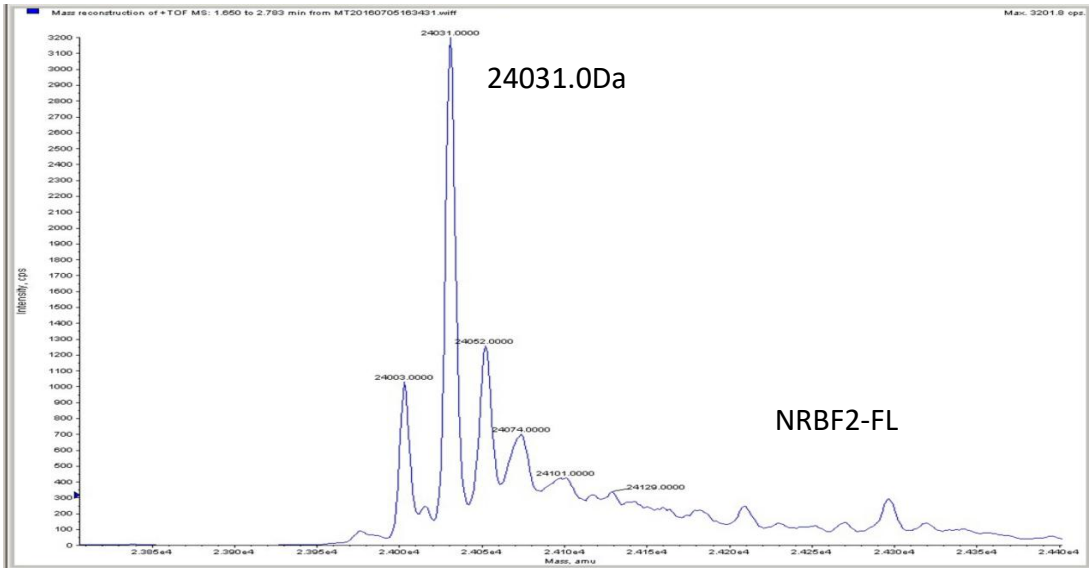

B

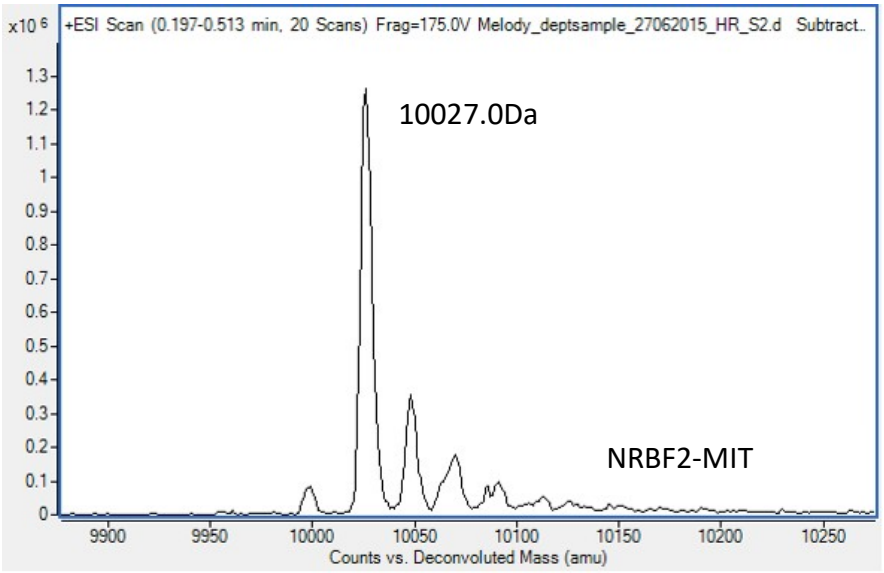

C

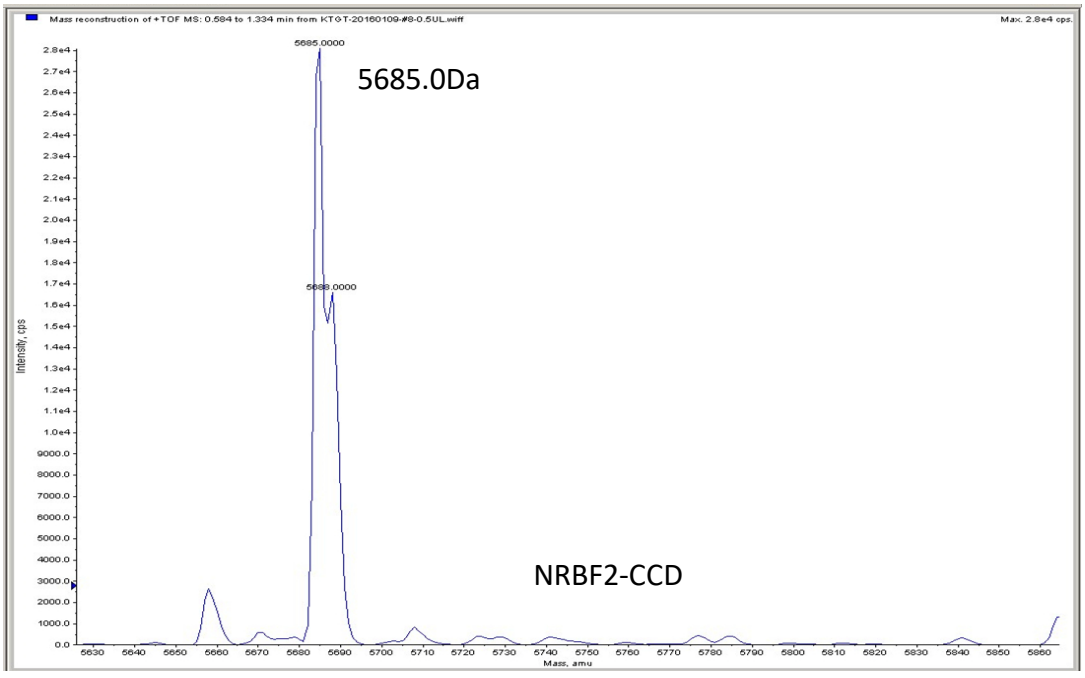

Figure 3.4 Mass spectra of NRBF2 constructs.

3.4 The CC domain of NRBF2 is responsible for its homodimerization

Subsequently, light scattering assay and Co-IP assay were employed to characterize the oligomeric states of NBRF2 constructs *in vitro* and *in vivo* respectively.

Light scattering data show the calculated molecular weight of NRBF2-FL is about 50kDa (Figure 3.5 A), i.e. about twice its theoretical value, indicating that NRBF2-FL forms a homodimer *in vitro.* In contrast, the measured molecular weight of NRBF2-MIT is quite close to its theoretical molecular weight (Fig 3.5 B), so we conclude that NRBF2-MIT forms a monomer in solution. In order to overcome the weak UV absorbance of NRBF2-CCD, two tyrosine were added to the N terminus of NRBF2-CCD through recombinant DNA technology. The theoretical extinction coefficient of the modified NRBF2-CDD at 280nm is 0.496 and the theoretical molecular weight is 6.012kDa (calculated by ExPASy ProtParam tool, http://web.expasy.org/protparam/). The molecular weight estimated by light scattering is about 13.1kDa, suggesting that NRBF2-CCD forms a homodimer in solution (Figure 3.5 C). Combining the light scattering data of NRBF2-FL, NRBF2-CCD and NRBF2-MIT described above, we can conclude that the CC domain of NRBF2 is responsible for its dimerization *in vitro*.

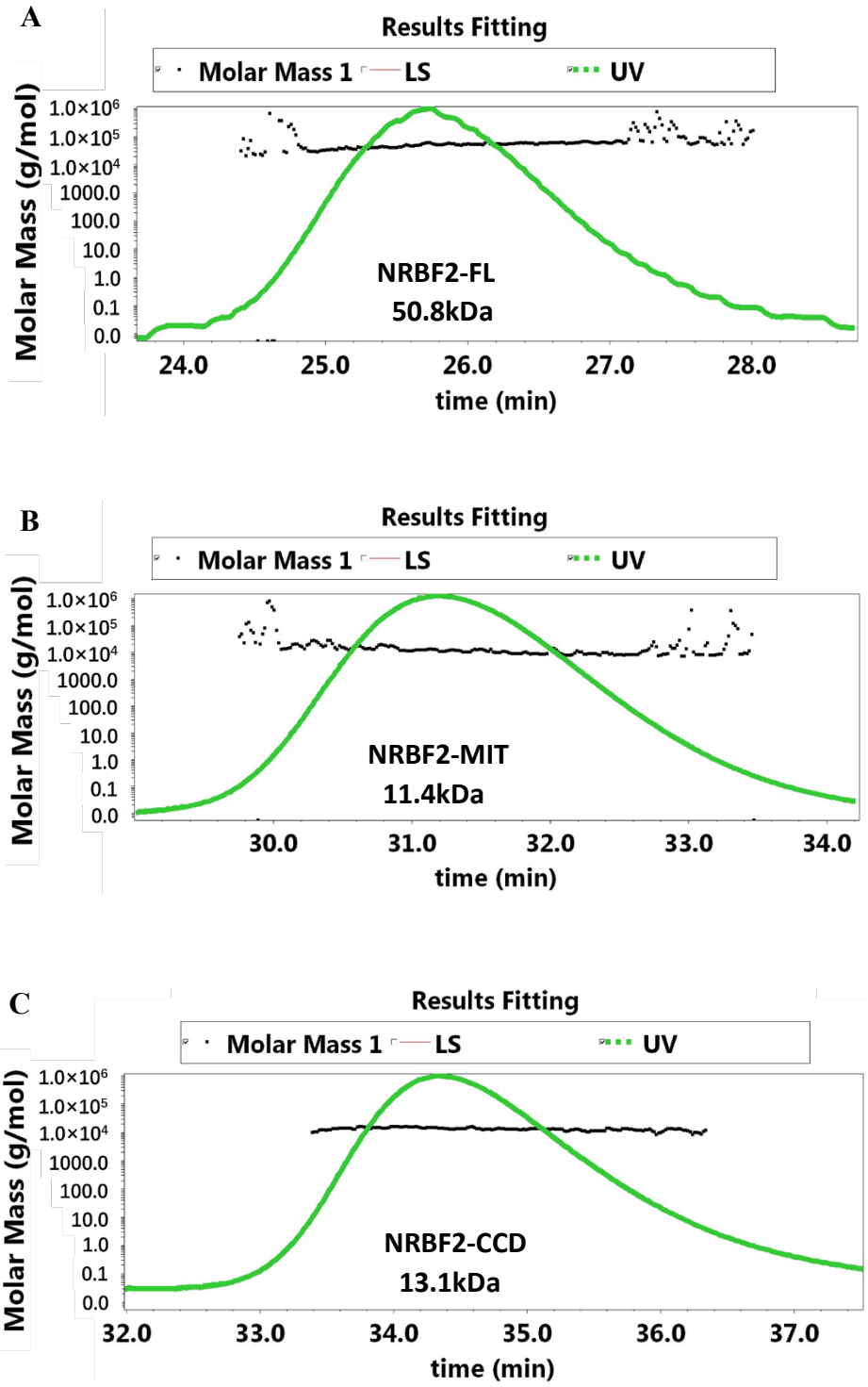

Figure 3.5 The Light scattering profiles of NRBF2 constructs. (A) Light scattering profile of NRBF2-FL, the measured molecular weight is 50.8kDa, indicating NRBF2-FL forms a homodimer. (B) Light scattering profile of NRBF2-MIT, the measured molecular weight is 11.4kDa, indicating NRBF2-MIT forms a monomer. (C) Light

scattering profile of NRBF2-CCD, the measured molecular weight is 13.1kDa, indicating NRBF2-CCD forms a homodimer.

To furtherly investigate whether the CC domain of NRBF2 is responsible for its self-association *in vivo*, the plasmids of NRBF2-FL, NRBF2-d-MIT, and NRBF2-d-CCD with GFP tag and Flag tag were transfected into HEK293T cells. After 48 hours of expression, the cells were collected and lysed for subsequent Co-IP assay. The results are shown in Figure 3.6. As we expected, the GFP-NRBF2-FL can be pulled down by Flag-NRBF2-FL, and the deletion of MIT domain has no effect on the self-association of NRBF2, while the self-association of NRBF2 is almost completely abolished when the CC domain is deleted. Taken together, the light scattering assay and Co-IP show the CC domain of NRBF2 is essential and sufficient for its self-association *in vitro* and *in vivo*.

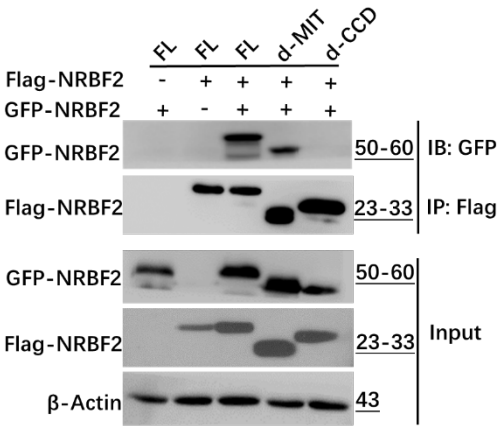

Fig 3.6 Co-IP assay suggests the MIT domain is not required for the self-association of NRBF2, while the CC domain is indispensable.

3.5 NRBF2-CCD homodimer is highly stable

CD spectroscopy was conducted to investigate the secondary structure and thermal stability of NRBF2-CCD. The CD spectrum of NRBF2-CCD at 20°C displays a large band with negative ellipticities at 222nm and 208nm, which is characteristic of coiled-coils (Newman & Keating, 2003). When temperature increases to 40°C furtherly, the CD spectrum doesn't show obvious changes, while the negative ellipticities at 222nm and 208nm both decrease when the temperature reaches 60°C (Figure 3.7 A), indicating the disruption of CC structure. The Tm (thermal transition temperature) value of NRBF2-CCD estimated by CD spectroscopy is about 70°C (Figure 3.7 B), suggesting the homodimer is stable at physiological temperature.

A

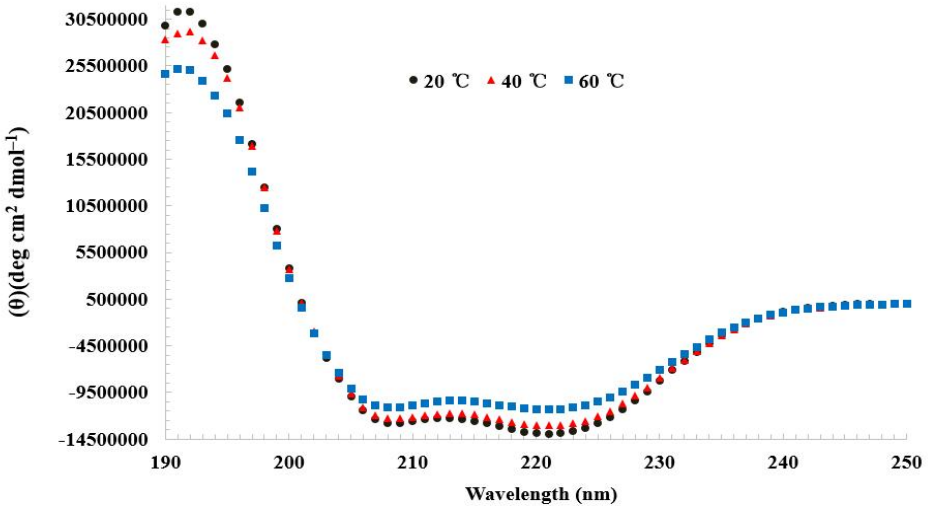

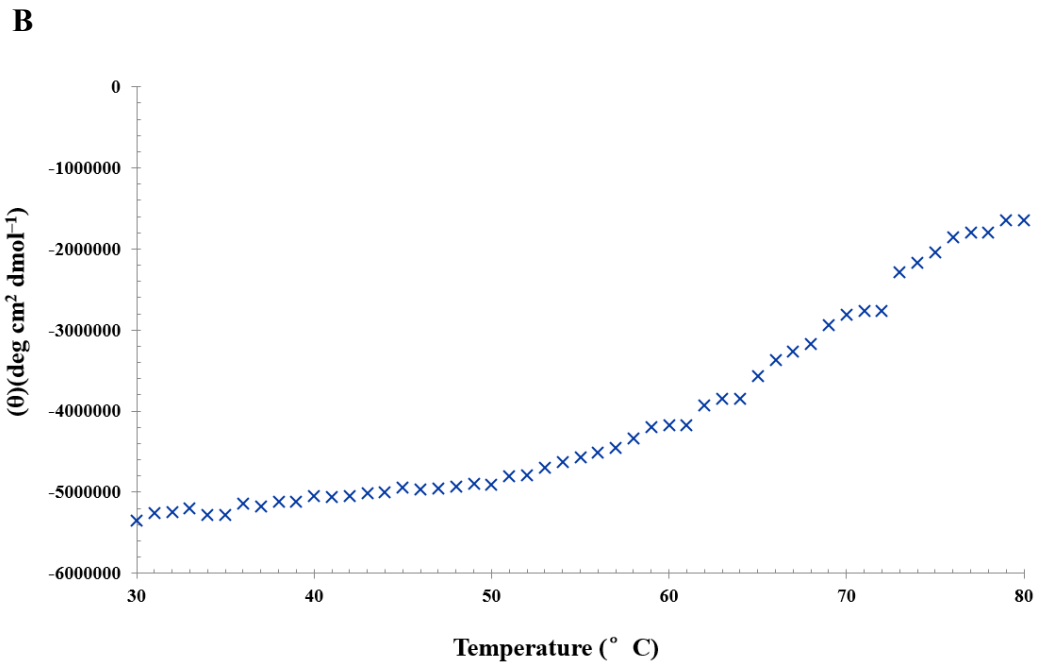

Figure 3.7 CD spectra of NRBF2-CCD. (A) CD spectra of NRBF2-CCD at different temperatures (20°C, 40°C and 60°C). The CD spectrum changed until the temperature increased to 60°C. (B) The temperature-dependent CD spectrum of NRBF2-CCD at 222nm, and the Tm value of NRBF2-CCD is around 70°C.

Additionally, isothermal titration calorimetry (ITC) experiments were conducted to further investigate the stability of the NRBF2-CCD. The dilution ITC experiment involves titrating a concentrated protein sample into the sample cell containing buffer alone. By detecting heat absorbed due to the disassociation of oligomerized protein, the dissociation constant Kd can be calculated. The concentrated NRBF2-CCD was titrated into Tris buffer (50 mM Tris and 150 mM NaCl, pH 8.0). The ITC curve (Figure 3.8 A) shows stable absorption of heat, and it is totally different from the typical ITC dissociation data (Figure 3.8 B), suggesting there is no dimer ⇌ monomer equilibrium

during the dilution of NRBF2-CCD. Next, the interaction between NRBF2-CCD and Beclin1-CCD or Atg14L-CCD was investigated respectively. As shown from the ITC profiles, there are no interactions between NRBF2-CDD and either Beclin1-CCD or Atg14L-CCD, indicating the CC domain of NRBF2 does not involve in its interactions with other members in PI3KC3 complex I, which is consistent with the previous report. Taken together, these data indicate the CC domain is only responsible for the dimerization of NRBF2, and the NRBF2-CCD homodimer is highly stable.

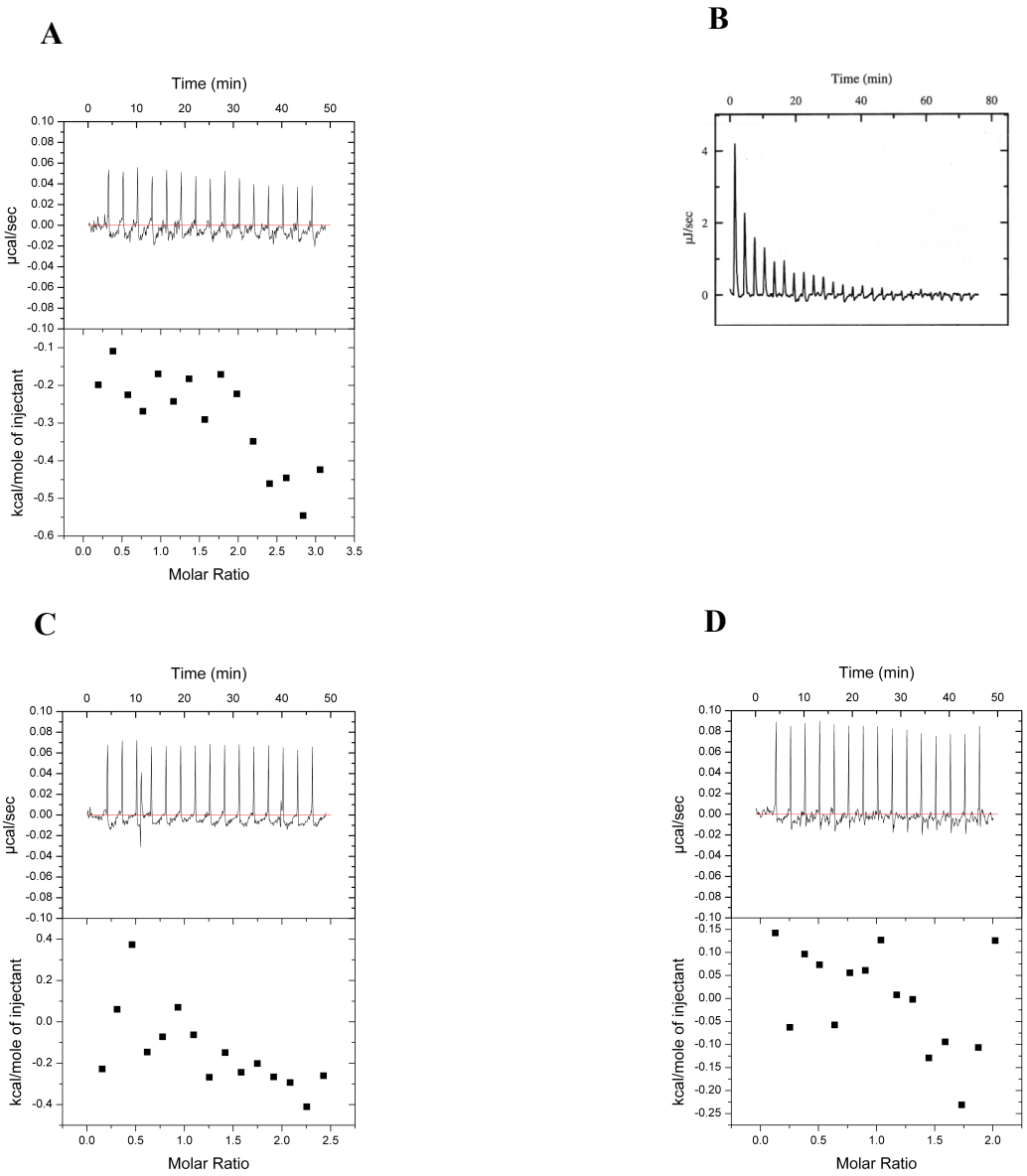

Figure 3.8 ITC assays suggest the NRBF2-CCD is highly stable. (A) ITC profile of titrating NRBF2-CCD to Tris buffer. The stable absorption of heat suggest NRBF2-CCD didn't dissociate when be diluted in the buffer. (B) A typical ITC curve for the disassociation of insulin dimers in buffer (Lovatt *et al.*, 1996). (C) ITC profile of titrating NRBF2-CCD to Atg14L-CCD. (D) ITC profile of titrating NRBF2-CCD to Beclin1-CCD.

Chapter 4: Structural studies of NRBF2-CCD

4.1 Crystallization of NRBF2-CCD under high-salt condition

Hanging drop vapor diffusion method was conducted to generate the crystal of NRBF2-CCD, and the kits from Hampton Research Company, including crystal screen, crystal screen 2, and Index, were used for initial screening. After optimization, high quality crystals were obtained by using reservoir solution with 3.916M NaCl and 0.1M Tris buffer (pH 7.0) (Figure 4.1 A). The crystal was subsequently tested by our in-house X-ray machine, and the diffraction pattern shows the packing of the native crystal is well-ordered and the resolution is around 2.2Å (Figure 4.1 B). The space group of the native crystal is C2221 with unit cell dimension of (84.43Å, 132.80Å, 87.26Å, 90°, 90°, 90°) (Table 4.1). Calculations of Matthew's coefficient confirms that there are 8 copies of NRBF2-CCD in the asymmetric unit. Such high copy number imposes challenge in terms of structure determination by either molecular replacement or heavy metal derivative phasing.

Table 4.1 Crystallographic data processing and refinement statistics

	Native	**Se-Met**
Data collection		
Space group	$C222_1$	$P2_12_12_1$
Cell dimensions		
a, b, c (Å)	84.53, 132.81, 87.290	57.83, 86.44, 103.69
α, β, γ (°)	90, 90, 90	90, 90, 90
Resolution (Å)	87.29-2.25 (2.37-2.25)	66.39-3.20 (3.37-3.20)
Rsym or Rmerge *	0.051 (0.148)	0.059 (0.146)
I/σI *	33.7 (14.7)	30.2 (14.4)
Completeness (%) *	100 (99.8)	98.7 (99.9)
Redundancy	12.4 (12.0)	13.2 (13.9)
Refinement		
Resolution (Å)	43.68-2.25	
No. reflections	22420	
Rwork/Rfree	0.219/0.256	
No. atoms		
Protein	2971	
Ligand/ion	N/A	
Water	279	
B-factors ($Å^2$)		
Main chain	28.996	
Side chain	36.695	
Water	34.986	
R.m.s deviations		
Bond length (Å)	0.016	
Bond angle (°)	1.873	

^ Numbers in parenthesis define the highest resolution shell of data.

* Numbers in parenthesis are the statistics for the highest resolution shell of data.

MIR, also called the heavy-atom method, is a commonly used approach to solve the phase problem. In this method, heavy metal atoms are introduced into the crystal as strong scatters by soaking or co-crystallization. The addition of heavy atom does not affect the conformation of the crystal, so the native crystal and its heavy-atom derivative are isomorphic. According to the difference of diffraction pattern between the native crystal and the isomorphic derivative, the initial estimates of the phase can be obtained.

In order to obtain heavy metal derivatives of NRBF2-CCD, crystals were grown in the same reservoir solution with additional 625μM $KAuCl_4$. However, no heavy atoms were detected in the derivative data set. It is possible that the high salt concentration (~4M NaCl) in the crystallization condition interfered with the diffusion of heavy metal ions.

We then turned to optimizing another crystal form grown from lower salt condition (Index reagent 2: 2.0M ammonium sulfate and 0.1M sodium acetate trihydrate, pH 4.5) (Figure 4.1 C). After adjusting the concentration of salt and pH value, single crystals were obtained under the condition of 2.0M ammonium sulfate and 0.1M sodium acetate trihydrate (pH 5.0) (Figure 4.1 D). However, the diffraction of crystal grown in this condition is poor, we then decided to optimize the construct of NRBF2-CCD to obtain crystals with better quality or suitable for heavy metal derivatization.

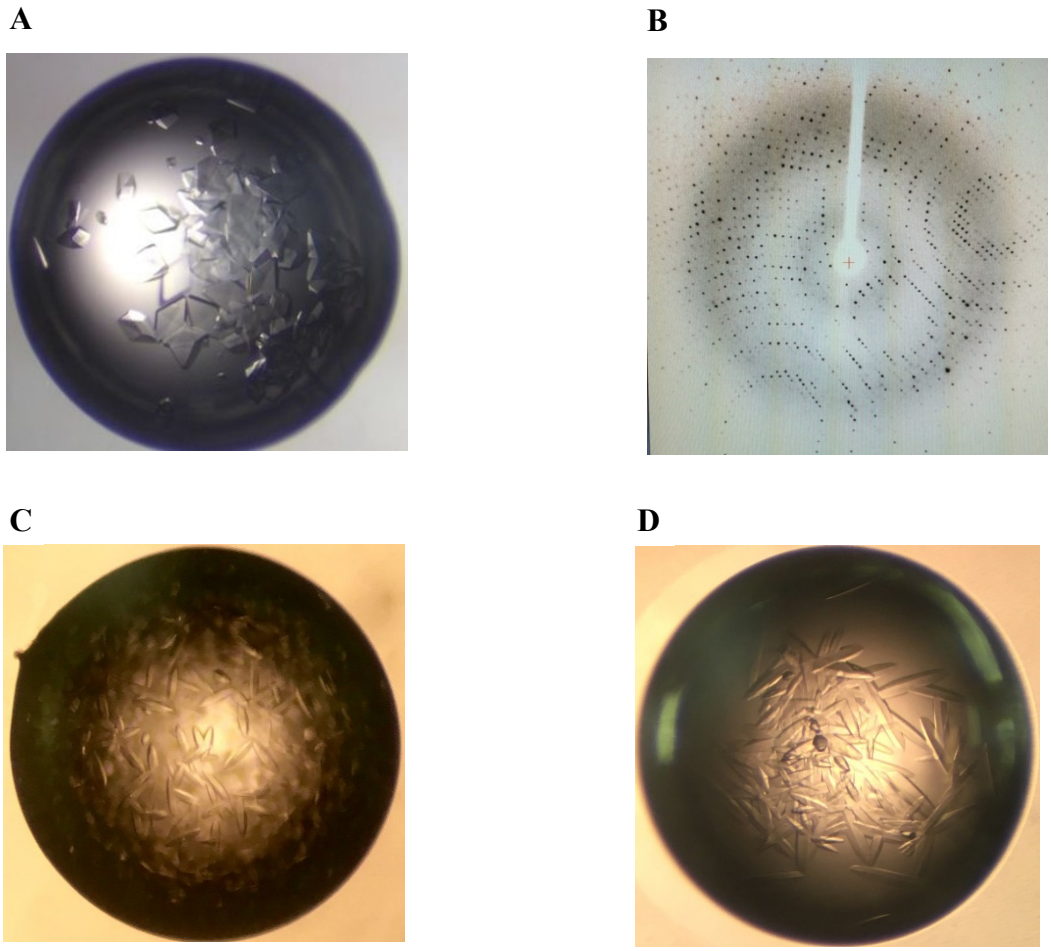

Figure 4.1 NRBF2-CCD crystals and the corresponding diffraction pattern. (A) Crystals grown from 3.916M NaCl and 0.1M Tris buffer (pH 7.0). (B) Corresponding X-ray diffraction image of crystal in figure A. (C) Crystals grown from the low salt condition: Index reagent 2 (2.0M ammonium sulfate and 0.1M sodium acetate trihydrate, pH 4.5). (D) Crystals grown from 2.0M ammonium sulfate and 0.1M sodium acetate trihydrate (pH 5.0).

4.2 Optimized constructs of NRBF2-CCD for crystallization

The preliminary construct of NRBF2-CCD (residue 165-210) was designed on the

basis of previous cell biology data (Lu *et al.*, 2014). As this construct failed to yield crystals suitable for heavy metal derivatization, several new constructs of NRBF2-CCD were designed with the expectation of solving this problem.

Table 4.2 Optimized NRBF2-CCD constructs (improve-1-3) for structural studies

Construct	length	Theoretical molecular weight
NRBF2-CCD-improve-1	162-210	6044.9Da
NRBF2-CCD-improve-2	162-208	5886.8Da
NRBF2-CCD-improve-3	165-210, F184Q	5667.5Da

Compared to the initial construct, there are only small adjustments in the sequence length of the first and the second construct, and for the third constructs, the hydrophobic F184 was mutated to hydrophilic Q184. We expected the small changes in sequence length and this site mutation are effective to improve the packing and arrangement of the crystal. These 3 new constructs were expressed in *E. coli* and purified following the general procedure described in the methodology. The freshly purified proteins were subsequently used for crystallization condition screening. However, the NRBF2-CCD-improve-1 and NRBF2-CCD-improve-2 failed to produce crystals under any screening condition. Crystals only grew from the third construct (Figure 4.2), and then these crystals were tested by our in-house X-ray machine, but all crystals show poor diffractions.

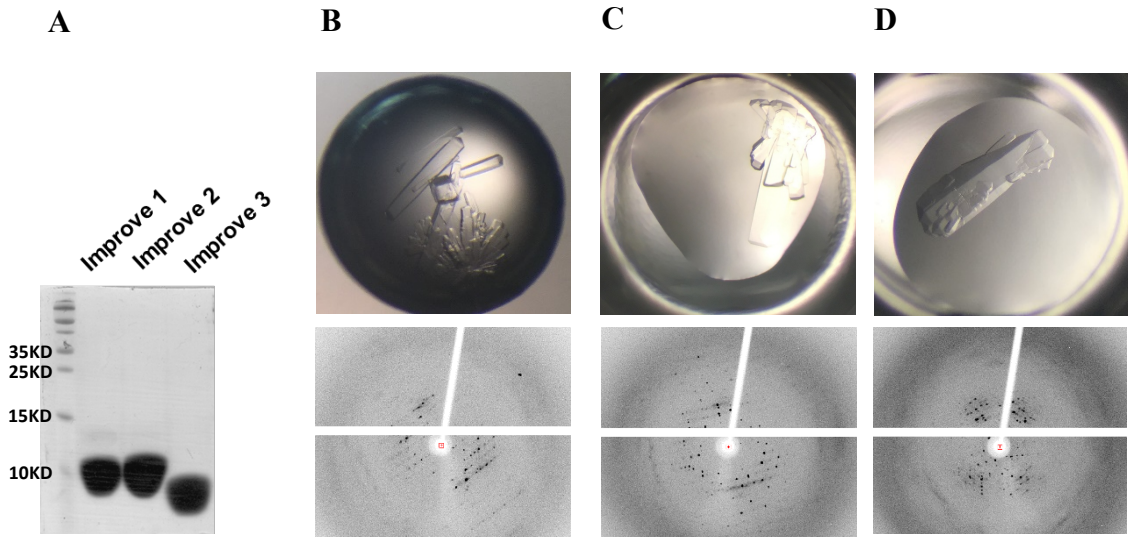

Figure 4.2 The crystals of NRBF2-CCD -Improve-3 show poor diffraction. (A) SDS-PAGE of purified proteins. (B) The crystal grown from Index reagent 1 (2.0M ammonium sulfate, 0.1M citric acid pH3.5) and its diffraction pattern. (C) The crystal grown from Index reagent 2 (2.0M ammonium sulfate and 0.1M sodium acetate trihydrate, pH 4.5) and its diffraction pattern. (D) The crystal grown from Crystal screen reagent 2. (2.0M Ammonium sulfate 0.1M sodium acetate trihydrate pH4.6) and its diffraction pattern.

Given these three NRBF2-CCD constructs (improve 1-3) failed to yield high-quality crystals under low salt condition, another three new constructs (improve 4-6) that extend the CC domain to longer range were designed in the hope to obtain crystals with better diffraction pattern.

Table 4.3 Optimized NRBF2-CCD constructs (improve 4-6) for structural studies

Construct	length	Theoretical molecular weight
NRBF2-CCD-improve-4	129-210	9699.06Da
NRBF2-CCD-improve-5	165-226	7492.51Da
NRBF2-CCD-improve-6	165-287	14097.03Da

During protein purification procedure, it was found that improve-5 and improve-6 showed degraded bands on SDS-PAGE gels, thus we suspected these two constructs were not stable. To confirm this assumption, the thermo stability of these three constructs was tested by leaving the protein samples at room temperature for 5 days and then checking possible degradation by SDS gels. The result showed that construct improve-4 was stable over five days, while the constructs improve-5 and improve-6 started to degrade after 7 hours with a band of ~ 4kDa showing on the SDS gel. This trend continued over the following days and ~50% degradation was observed for both constructs by the 5th day (Fig. 4.3). Given that improve-5 and -6 are essentially improve-4 with C-terminal extension, we suspect that the added C-terminal fragment is not part of the CC domain and instead highly flexible, thus prone to degradation and not suitable for crystallization. Construct improve-4 was chosen for crystallization screening. However, no crystals were obtained even after extensive screening.

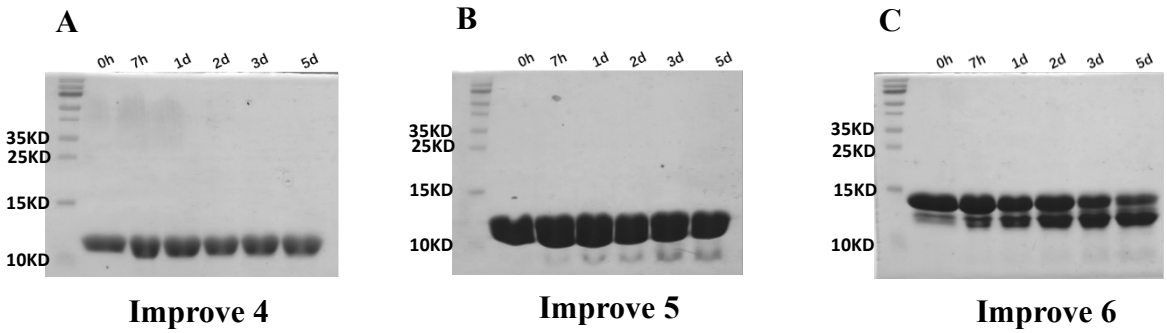

Figure 4.3 Thermo stability test of NRBF2-CCD-improve 4-6. The proteins were placed in the room temperature for 7h, 1d, 2d, 3d and 5d respectively, and then be analyzed by SDS-PAGE. The more amount of degraded band indicates the lower thermo stability.

In summary, a lot of works were carried out to optimize the construct of NRBF2-CCD with the aim to obtain high-quality crystals under low-salt condition. However, we failed to get crystals with good diffraction, and we decided to devote the effort to obtain selenomethionyl protein crystals grown from high-salt condition for NRBF2-CCD (residue 165-210) construct. With SeMet substitution, the phase problem can be solved by the standard MAD method.

4.3 Phase determination of NRBF2-CCD

As we failed to solve the phase problem by using MIR, another method MAD was employed to determine the phase. SeMet substitution is a general method for introducing anomalously scattering atoms into a recombinant protein. Selenium and

Sulfur are both chalcogens in the periodic table and they have similar chemical properties, so the methionine can be replaced completely by SeMet through culturing *E. coli* in medium which provides SeMet as the only source of methionine while the protein structure and function does not change. Given there is no methionine residue within NRBF2-CCD, we firstly designed two mutants L178M and L192M by mutating one leucin residue at *d* position to methionine residue respectively, as both leucin and methionine are hydrophobic residues. The selenomethionyl NRBF2-CCD proteins were purified following the standard procedure, and sufficient amount was obtained for subsequent crystallization trial (Figure 4.4). However, these two mutants failed to produce crystals under any screening condition. Subsequently we turned to mutate Q171 and Q198 at the N/C terminal of NRBF2-CCD to methionine respectively with the expectation of obtaining crystals with high quality.

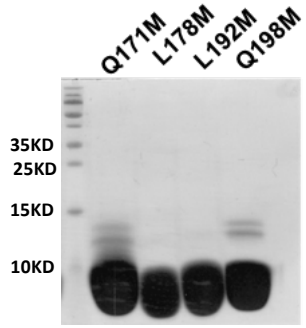

Figure 4.4 SDS-PAGE of four purified selenomethionyl NRBF2-CCD proteins.

The Q171M mutant yielded crystals after the initial crystallization screening, and the best crystals grew from 0.1M Bis-Tris, pH 5.5, 3.8M NaCl (Figure 4.5 A). The crystal was then tested by the in-house X-ray machine, and the diffraction resolution is around 3.8Å (Figure 4.5 B). Although the resolution of this SeMet derivative is not high

enough, we still tested the crystal at Shanghai Synchrotron Radiation Facility (SSRF) at the wavelength of 0.97946 Å, and collected datasets for phasing determination, and the resolution is up to 3.0Å (Figure 4.5 C).

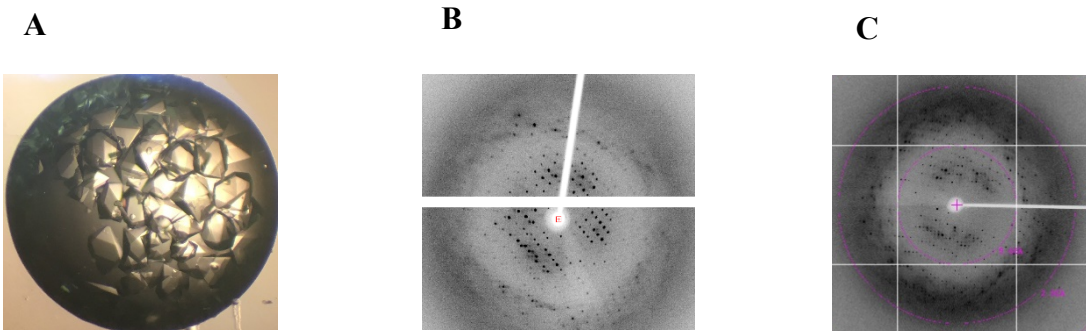

Figure 4.5 Crystals of selenomethionyl NRBF2-CCD Q171M mutant and the corresponding diffraction patterns. (A) Crystals of selenomethionyl NRBF2 Q171M mutant. (B) The diffraction pattern of the SeMet derivative tested by in house X-ray system. (C). The diffraction pattern of the SeMet derivative tested by synchrotron X-ray source.

The datasets were integrated by iMosflm (Leslie, 2006), and then scaled by SCALA (Evans, 2006) in CCP4 package. Statistics are summarized in Table 4.1. The Autosol and Autobuild in Phenix (Adams *et al.*, 2002) were employed to solve the initial phase and model, and eight selenium atoms were identified in an asymmetric unit. The R_{work} of model is 0.466, suggesting the quality of this model is poor. Subsequently, the optimized model was achieved by molecular replacement via Phaser MR program (McCoy *et al.*, 2007) in CCP4 package with the native dataset as reference. After several rounds of refinement by REFMAC (Murshudov *et al.*, 1997) and manual correction by COOT (Emsley & Cowtan, 2004), the final structure was achieved with

R_{work} = 0.219 and R_{free} = 0.256. The CCP4 mg package was employed for preparing the structure figures.

4.4 The structure of NRBF2-CCD

The crystal structure of NRBF2-CCD reveals a parallel coiled-coil homodimer with two helices wrapped around each other. The length of the homodimer is around 62 Å (Figure 4.6 A). Besides, the electrostatic potential map shows the amount of negative-charged residues and that of the positive-charged residues is similar (Figure 4.6 B).

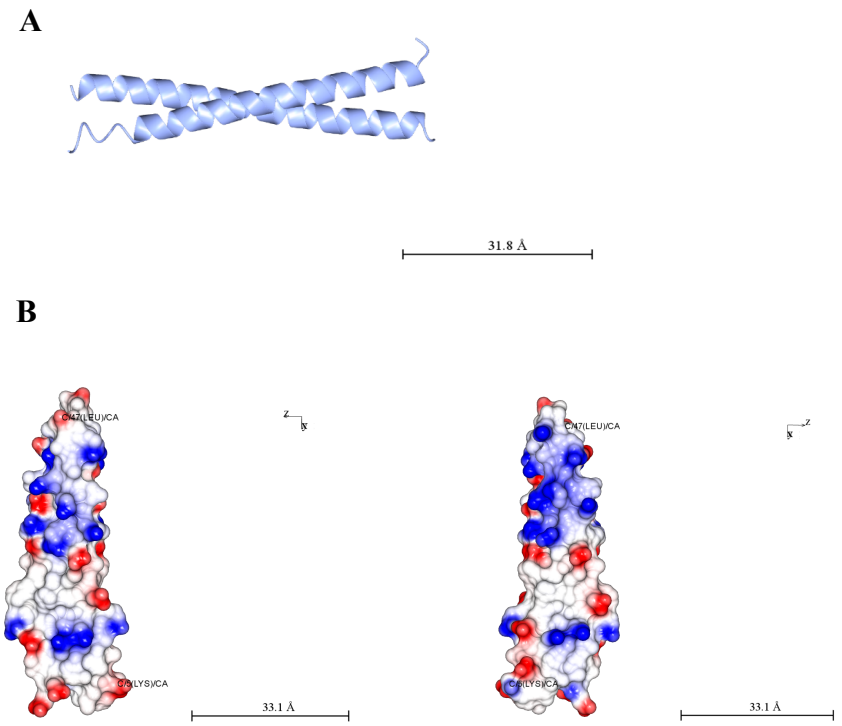

Figure 4.6 The crystal structure of NRBF2-CCD. (A) The parallel homodimeric crystal structure of NRBF2-CCD. (B) The distribution of electrostatic charges on NRBF2-CCD homodimer surface.

The NRBF2-CCD dimer interface displays the canonical pattern of parallel coiled-coil. The amino acid residues at *a* and *d* positions within the heptad repeat motif form *a-a'* and *d-d'* pairings through hydrophobic interaction to stabilize the homodimer interface (Figure 4.7).

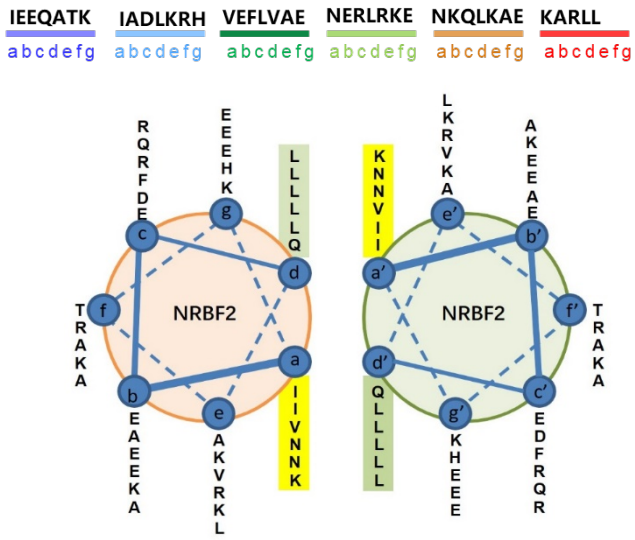

Figure 4.7 Helical wheel presentation of the NRBF2 coiled-coil homodimer interface.

Analysis of the NRBF2-CCD dimer interface reveal molecular features that account for the highly stability of NRBF2-CCD homodimer. Among the 12 *a-a'* and *d-d'* pairings, 8 pairs (I168-I168, I175-I175, L178-L178, V182-V182, L185-L185, L192-L192, L199-L199, L206-L206) are canonical pairings with hydrophobic amino acid residues. Notably, 5 pairs of these 8 canonical pairings are so-called 'perfect' leucin zippers which strongly stabilize the parallel coiled-coil interface (Figure 4.8 A). Besides, NRBF2-CCD contains 3 'imperfect' *a-a'* and *d-d'* pairings with polar residues (Q171-Q171, N189-N189, N196-N196) that may moderately stabilize the coiled-coil interface

by forming hydrogen bonds (Figure 4.8 B). There is one electrostatically repulsive pairing (K203-K203') that may destabilize the homodimer interface (Figure 4.8 C) The structural information of NRBF2-CCD obtained from the interface is consistent with our previous findings based on light scattering and CD spectra, which suggest the CC domain of NRBF2 is a highly stable dimer.

A

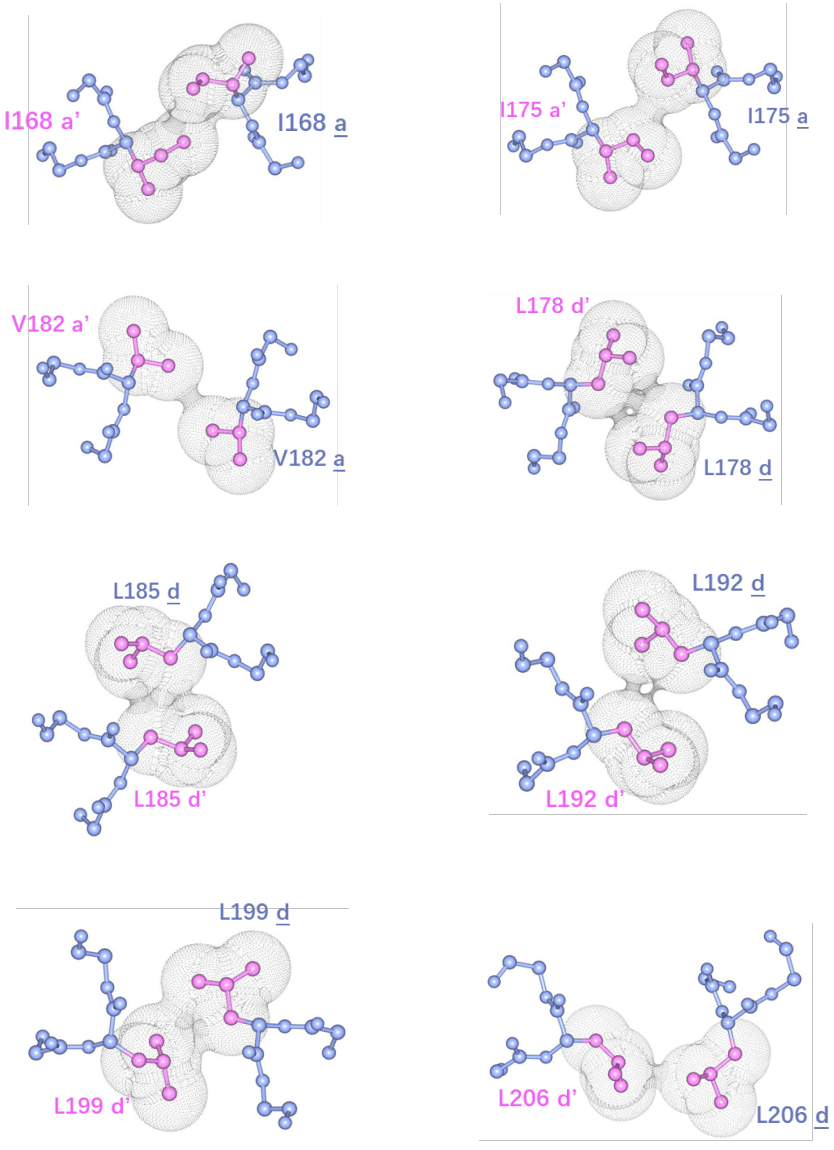

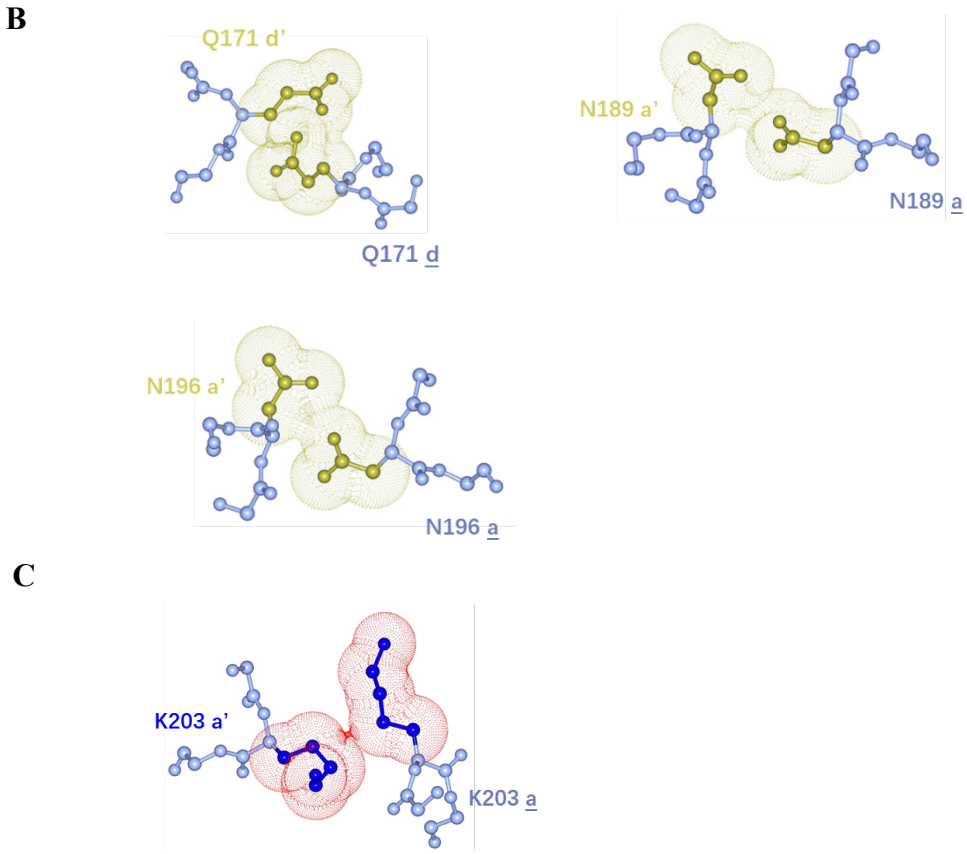

Figure 4.8 Close-up view of the hydrophobic and electrostatic pairings of structure. (A) Close-up view of 8 canonical *a-a'* and *d-d'* pairings on the NRBF2-CCD homodimer interface. Each residue is illustrated in ball-and-stick model. Main-chain atoms are colored light blue and side-chain atoms are colored pink. The *a-a'* and *d-d'* pairings are illustrated by van der Waals spheres depicting the side-chain. (B) Close-up view of 3 'imperfect' *a-a'* and *d-d'* pairings on the NRBF2-CCD homodimer interface. Each residue is illustrated in ball-and-stick model. Main-chain atoms are colored light blue and side-chain atoms are colored golden. The *a-a'* and *d-d'* pairings are illustrated by van der Waals spheres depicting the side-chain. (C) Close-up view of 1 electrostatically repulsive *a-a'* pairing on the NRBF2-CCD homodimer interface. Main-chain atoms are colored light blue and side-chain atoms are colored dark blue.

The *a-a'* pairing is illustrated by van der Waals spheres depicting the side-chain.

The crystal structure of the CC domain of Atg38, the yeast homolog of NRBF2, has been reported by a previous study (Ohashi *et al.*, 2016) (Figure 4.9). Among the 9 *a-a'* and *d-d'* pairings within the Atg38 homodimer interface, 6 *a-a'* and *d-d'* pairings are canonical pairings (F182-182F, Y185-Y185, I192-I192, L199-L199, I203-I203, W210-W210). However, 2 pairings (K188-K188, R207-R207) contain amino acid residues with same charges that repel each other, and 1 pairing is mis-aligned (N195-196E). These 3 pairings are not beneficial for the stability of the coiled-coil homodimer assembly. Comparison of the NRBF2 and Atg38 structures, especially counting the canonical *vs.* non-canonical pairings at the dimer interface, suggests that NRBF2 CC domain is likely to be more stable than that for Atg38.

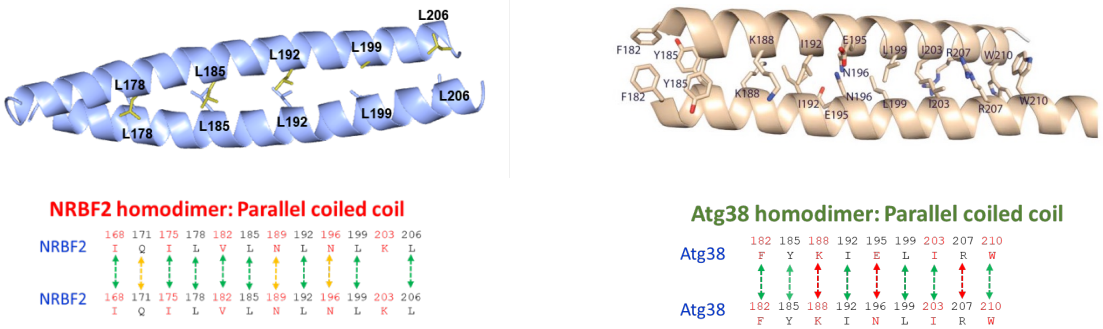

Figure 4.9 Atomic details of *a-a'* and *d-d'* pairings at the interface of NRBF2 homodimer and Atg38 homodimer.

4.6 Key residues for NRBF2-CCD self-association

According to the structural information obtained from the crystal, five leucine pairs (178L, 185L, 192L, 199L and 206L) at the dimer interface were identified as the key interactions to stabilize the NRBF2-CCD homodimer. Several monomeric mutants that replace the leucine residues with alanine were designed to test whether these leucine pairs observed in the crystal structure were indeed critical for the homodimeric state of NRBF2-CCD *in vitro* and *in vivo.* Firstly, the mutants were expressed in *E. coli*. and then purified followed the same procedure with the wild type (Figure 4.10 A). Subsequently, light scattering was employed to analyze the oligomeric state of these proteins. The results (Figure 4.10 B&C) show the measured molecular weights of the double mutants (NRBF2-CCD L178A_L185A and L199A_L206A) both are around 13kDa, which are about twice their theoretical values, indicating the double mutations are not enough to disrupt the homodimer formation. In contrast, the measured molecular weight of the triple (3A) and penta (5A) mutants (L178A_L185A_L192A and L178A_L185A_L192A_L199A_L206A) is close to the value for monomeric state (Figure 4.10 D&E). These results suggest that replacing three or more of the key leucine residues is sufficient to abolish the self-association mediated by the NRBF2 CC domain. In summary, the Leu-to-Ala mutational studies show that the NRBF2-CCD homodimer is highly stable *in vitro*. At least three leucine pairs are required to be mutated for the disruption of NRBF2-CCD homodimer.

A

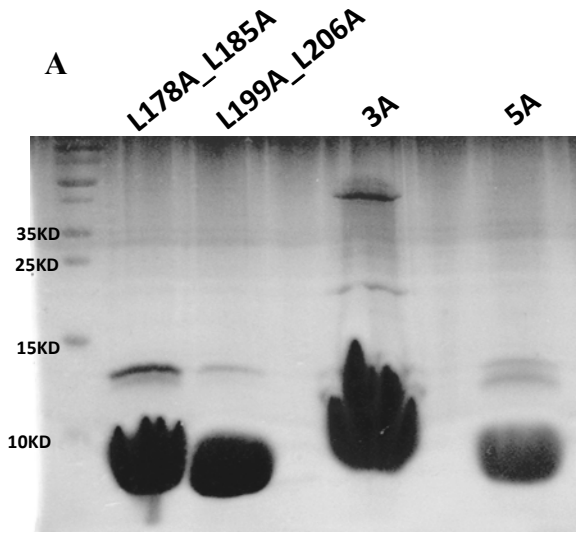
L178A_L185A
L199A_L206A
3A
5A
35KD
25KD
15KD
10KD

B

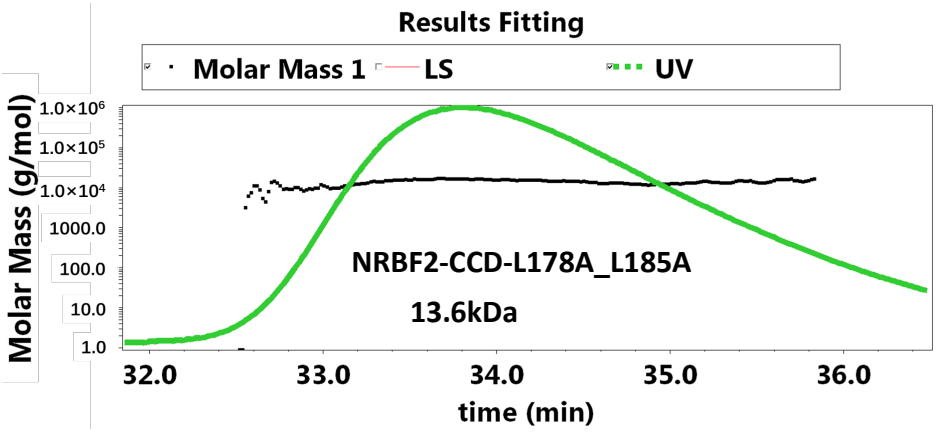
Results Fitting
Molar Mass 1
LS
UV
Molar Mass (g/mol)
1.0×10⁶
1.0×10⁵
1.0×10⁴
1000.0
100.0
10.0
1.0
NRBF2-CCD-L178A_L185A
13.6kDa
32.0
33.0
34.0
35.0
36.0
time (min)

C

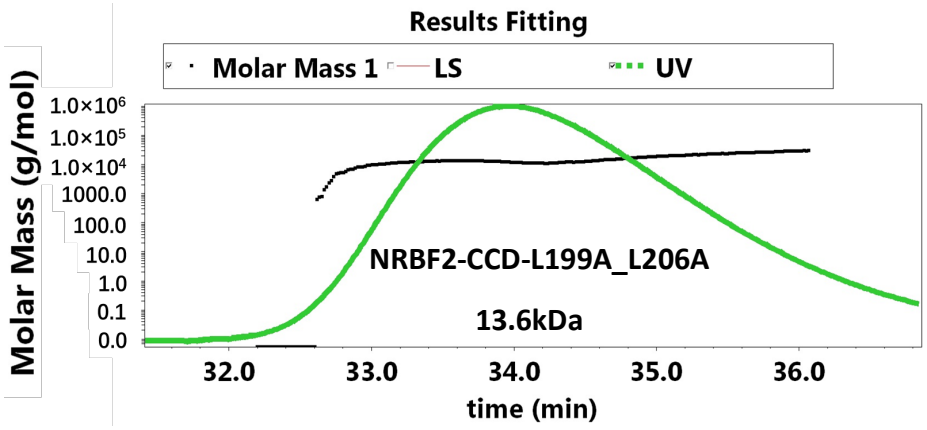
Results Fitting
Molar Mass 1
LS
UV
Molar Mass (g/mol)
1.0×10⁶
1.0×10⁵
1.0×10⁴
1000.0
100.0
10.0
1.0
0.1
0.0
NRBF2-CCD-L199A_L206A
13.6kDa
32.0
33.0
34.0
35.0
36.0
time (min)

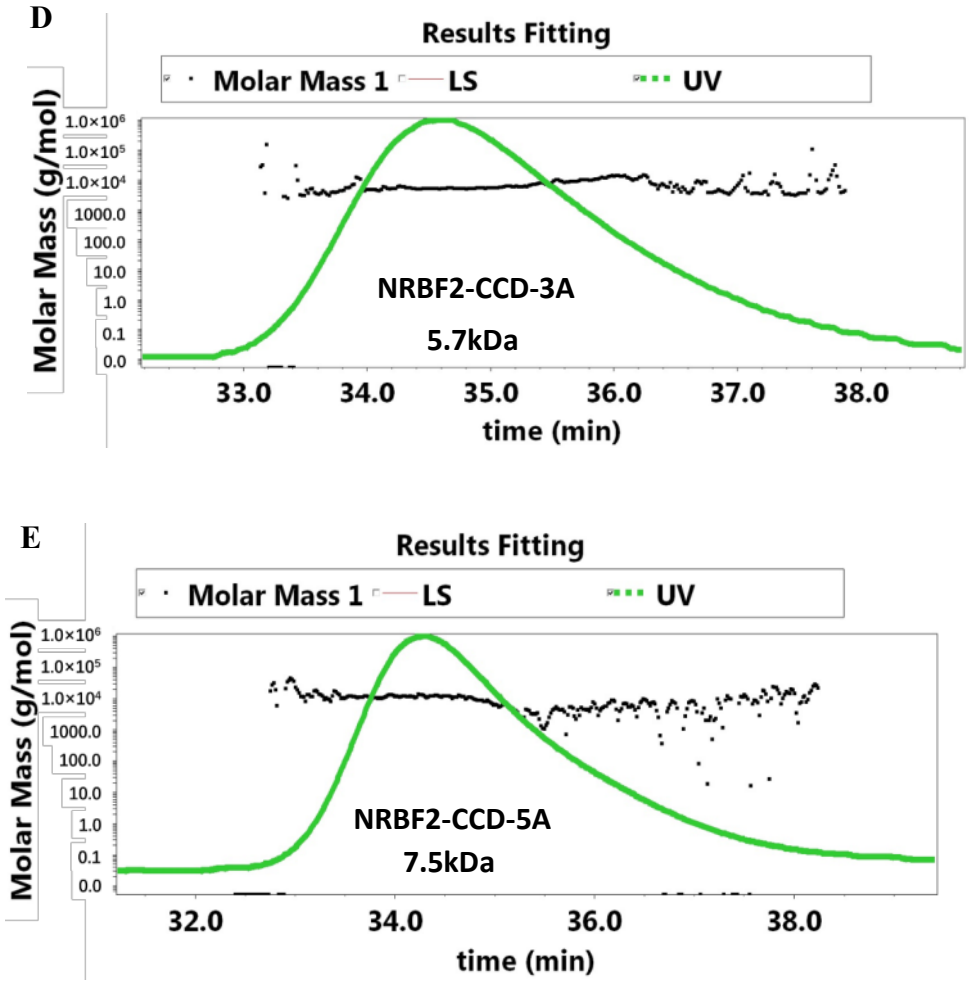

Figure 4.10 The light scattering profiles of NRBF2 monomeric mutants. (A) The SDS-PAGE of purified NRBF2-CCD mutants. (B-E) Characterization the oligomeric states of NRBF2-CCD mutants by light scattering.

In terms of *in vivo* assay, these constructs were inserted into the vectors with Flag tag or GFP tag respectively, and then were transfected into HEK293T cells. After 48 hours expression, the cell was collected and lysed for Co-IP assay with anti-Flag followed by immunoblotting with anti-GFP. As shown in Figure 4.11, the double mutant L199A_L206A can still self-associate like the wild type construct, while surprisingly, the self-association of another double mutant L178A_L185A was weakened significant

in vivo. For the triple and quintuple mutants, the self-association of NRBF2-CCD is completely abolished, which is consistent with the light scattering data described previously.

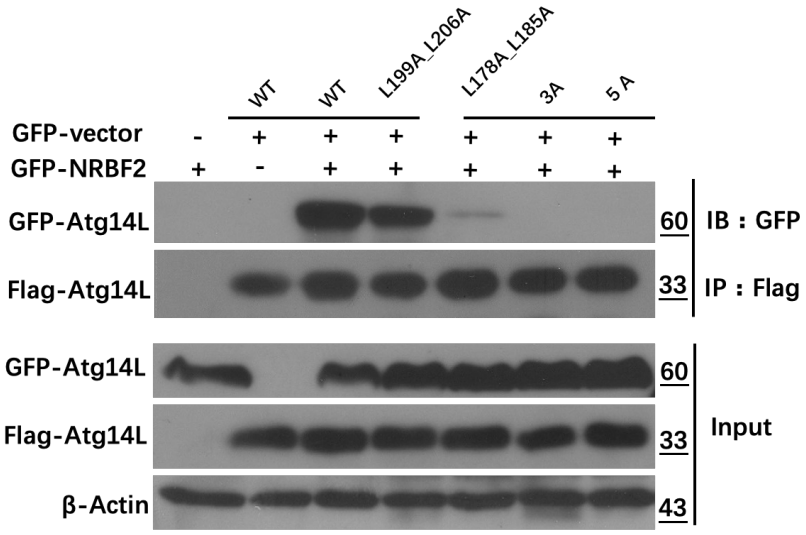

Figure 4.11 Characterization the self-association of NRBF2-CCD mutants by Co-IP assay.

Chapter 5: Biochemical investigation of possible NRBF2-Beclin1 and NRBF2-Atg14L interactions

As we introduced previously, several studies have shown that NRBF2 only binds to the Atg14L-containing PI3KC3 complex I but not the UVRAG-containing PI3KC3 complex II. Besides, Co-IP assay and HDX results suggest that Atg14L and Beclin1 are two potential binding partners for NRBF2, with their N termini as likely binding sites (Young *et al.*, 2016,Ohashi *et al.*, 2016). To furtherly confirm the binding partners of NRBF2, we decided to investigate the direct interaction between NRBF2 and Atg14L/Beclin1 using biochemical methods such as ITC.

5.1 Investigating the direct interaction between NRBF2-FL and Atg14L/Beclin1.

ITC is the primary technique employed to investigate possible interaction between NRBF2 and Beclin1/Atg14L. Multiple constructs were generated, including NRBF2-FL (residue 4-210), Atg14L N-terminal (residue 1-95) and Beclin1 N-terminal (residue 1-105). Before each ITC experiment, recombinant protein for each construct was purified and diluted by Tris buffer (50mM Tris, 150mM NaCl, pH 8.0) to the proper concentration (normally, the concentration of the protein sample in syringe is 750μM, while the concentration for the protein in the sample cell is 50μM). After degassing by high speed centrifugation (13000rpm for 5min), 40μl protein sample was loaded in syringe and 280μl of the potential binding partner was injected into sample cell. Experimental parameters, such as stirring speed, injection number and volume, were

set according to user manual (ITC 200, Malvern).

Firstly, the interaction between NRBF2-FL and Atg14L-1-95/Beclin1-1-105 was investigated by ITC. As shown in Figure 5.1, the ITC profiles suggest NRBF2-FL has no interaction with either Atg14L-1-95 or Beclin1-1-105.

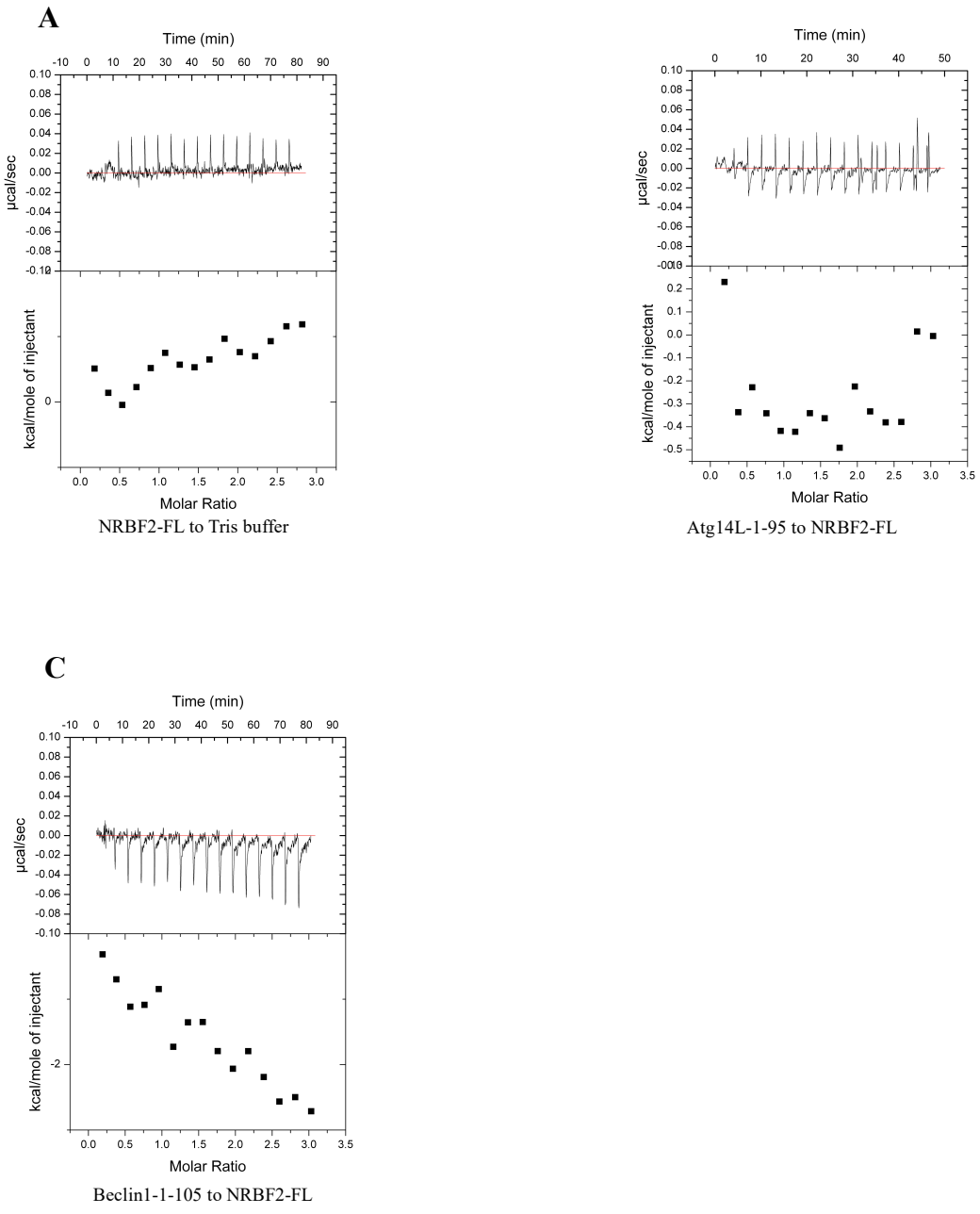

Figure 5.1 Characterization the interaction between NRBF2-FL and

Atg14L/Beclin1 N-terminal by ITC. (A) ITC profile of titrating NRBF2-FL to Tris buffer. (B) ITC to characterize the interaction between NRBF2-FL and Atg14L-1-95. (C) ITC to characterize the interaction between NRBF2-FL and Beclin1-1-105.

Given that the first trial failed to confirm the interaction between NRBF2 and the N-termini of Beclin1 or Atg14L, we decided to conduct systematic mapping of Atg14L an Beclin1 to identify the regions responsible for the binding to NRBF2. For this purpose, a series of Atg14L and Beclin1 constructs have been subsequently designed and expressed in *E. coli* (Figure 5.2). The purification of these constructs followed a general procedure described above. It was found that some of them were insoluble or precipitated after removing fusion tag (indicated by black lines in Figure 5.2), while other constructs (indicated by blue lines in Figure 5.2) were purified successfully. Subsequently, ITC assays were conducted following the similar procedure and parameters described previously to probe the interaction between NRBF2-FL and these constructs. All together, over 12 rounds of ITC experiments were carried out but none showed any interaction between NRBF2-FL and the different Atg14L or Beclin1 constructs. To save space, the detailed ITC profiles are not listed.

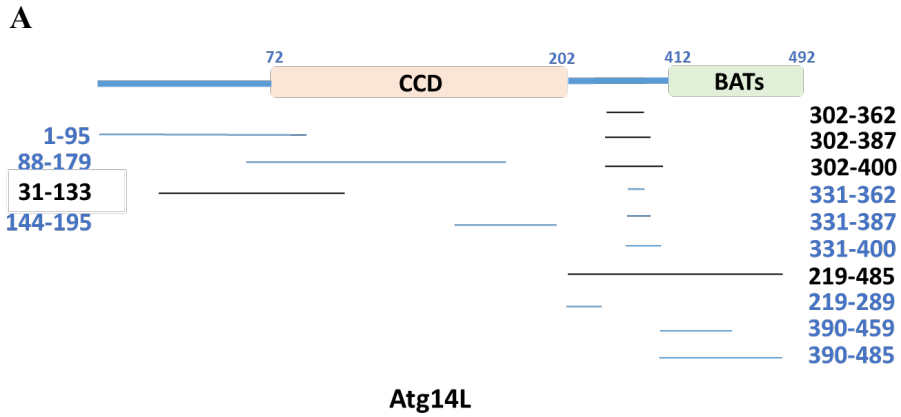

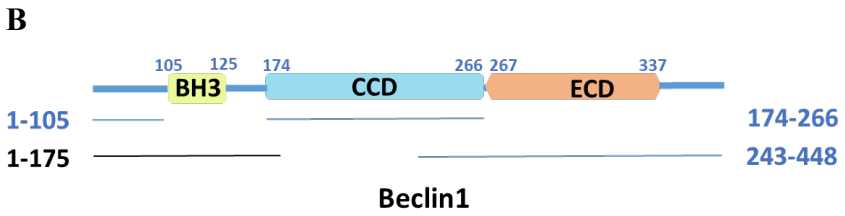

Figure 5.2 Constructs designed for protein-protein interaction experiments. Blue lines indicate constructs have been purified successfully; otherwise the constructs are indicated by black lines. (A) Atg14L constructs designed for protein-protein interaction experiments. (B) Beclin1 constructs designed for protein-protein interaction experiments.

5.2 Investigating the direct interaction between NRBF2-MIT and Atg14L/Beclin1

Although our ITC data suggested there was no interaction between NRBF2-FL and Atg14L/Beclin1, we still probed the interaction between NRBF2-MIT and Atg14L/Beclin1. This is because the MIT domain of NRBF2 has been reported to be required for binding to Atg14L. Also it is possible the NRBF2-FL construct may have some folding problems that rendered it unfit for binding to Atg14L (Lu *et al.*, 2014). Recombinant protein for NRBF2 MIT domain was purified and its interaction with the N-terminal of Atg14L (residue 1-95) or Beclin1 (residue 1-105) was investigated by ITC. Unfortunately, the ITC profile showed there is no interaction between NRBF2-MIT and Atg14L-1-95 or Beclin1-1-105.

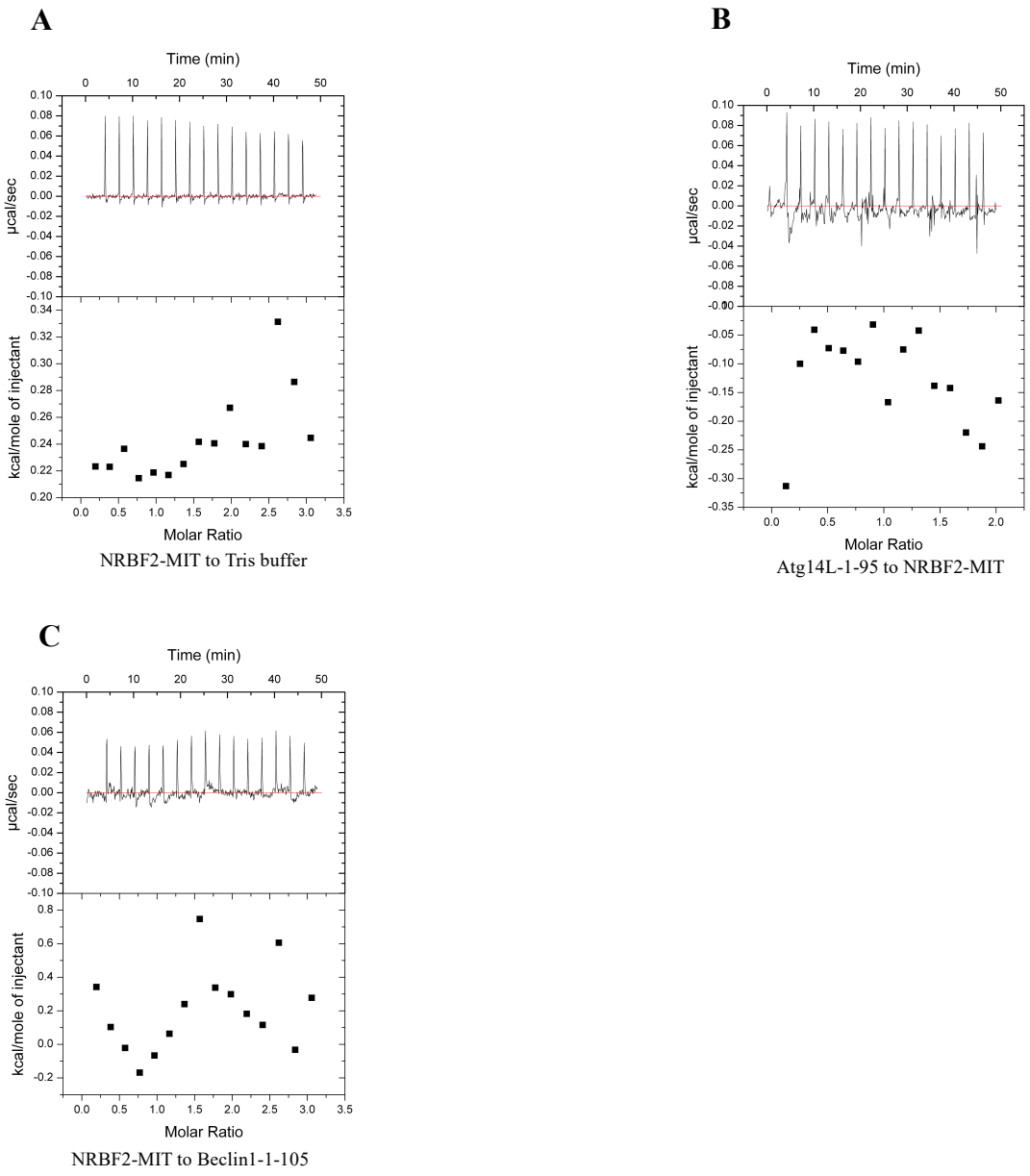

Figure 5.3 Characterization the interaction between NRBF2-MIT and Atg14L/Beclin1 N-terminal by ITC. (A) ITC profile of titrating NRBF2-MIT to Tris buffer. (B) ITC to characterize the interaction between NRBF2-MIT and Atg14L-1-95. (C) ITC to characterize the interaction between NRBF2-MIT and Beclin1-1-105.

We then proceeded to characterize the interaction between NRBF2-MIT and Atg14L-1-95 by NMR. This is because we reason that ITC assay is only appropriate if

the protein-protein interaction involves measurable enthalpy change (ΔH). If the interaction between NRBF2-MIT and Atg14L-1-95 is based on hydrophobic packing and doesn't involve significant heat exchange, then the ITC method would not detect this interaction with good sensitivity. In contrast, NMR titration can measure the chemical perturbations caused by even weak protein-protein interactions. Thus to thoroughly investigate the NRBF2-Atg14L interaction, we decided to give this method a try. Isotopically ^{15}N-labeled recombinant protein of Atg14L-1-95 was generated by growing bacteria in M9 minimal media containing $^{15}NH_4Cl$. The detailed M9 expression procedure has been described in the methodology part (2.4.3). Before data collecting, the purified ^{15}N-labeled Atg14L-1-95 was dissolved in buffer containing 10% D_2O, and the final concentration of protein sample was about 0.15mM. Firstly, the ^{1}H-^{15}N HSQC spectrum of ^{15}N-labeled Atg14L-1-95 alone was collected (Figure 5.4 A). Next, NRBF2-MIT was titrated into ^{15}N-labeled Atg14L-1-95 until the mixture reached the molar ratio of 1: 1. The HSQC spectrum after titration was then collected and compared to that before titration to search for chemical shifts (Figure 5.4 A). Our data shows that the HSQC spectra of Atg14L-1-95 before and after NRBF2-MIT titration are nearly identical, suggesting almost no direct interactions between these two proteins (Figure 5.4 A). Similar results were obtained when the molar ratio of NRBF2-MIT: Atg14L-1-95 was increased from 1: 1 to 8: 1 (Figure 5.4 B). Taken together, the NMR results suggest there is no interaction between Atg14L-1-95 and NRBF2-MIT.

A

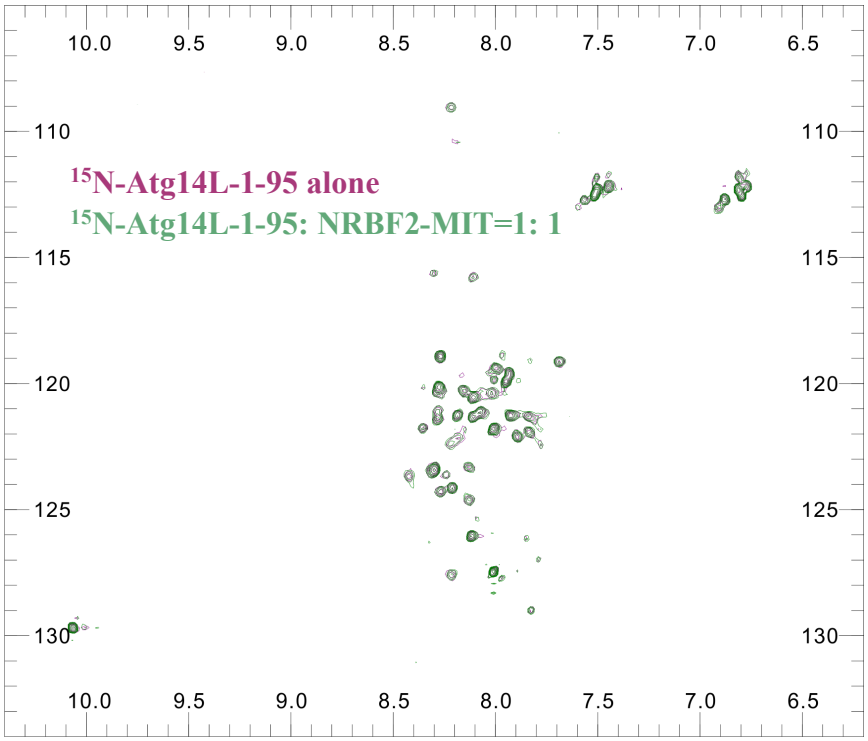

B

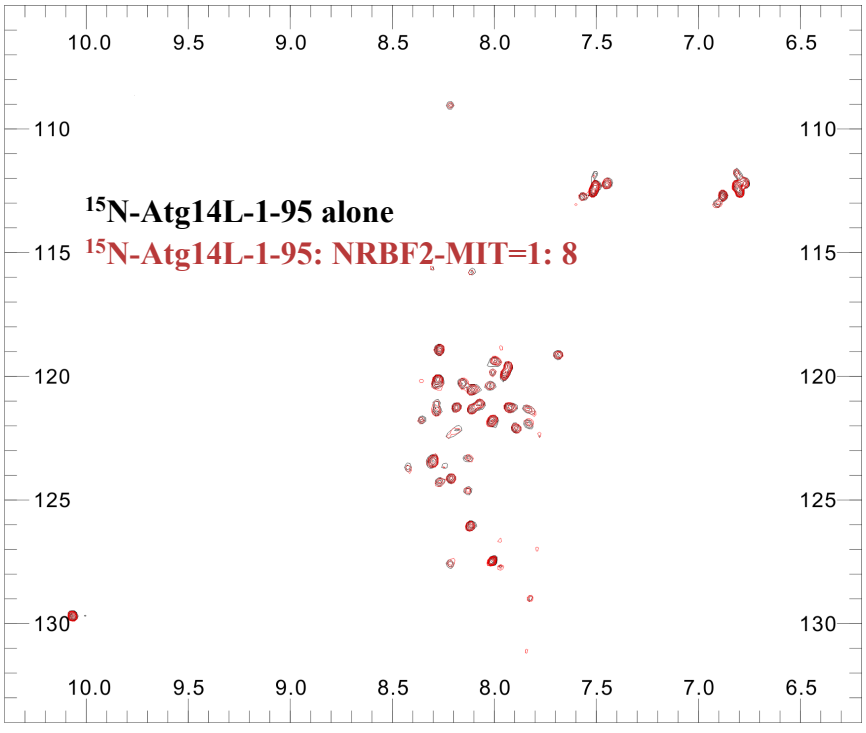

Figure 5.4 Characterization the interaction between NRBF2-MIT and Atg14L by ^{1}H-^{15}N NMR. (A) ^{1}H-^{15}N NMR spectra of ^{15}N-labeled Atg14L-1-95 alone (purple spots)

and that of after titrating with NRBF2-MIT (green spots) (^{15}N-labeled Atg14L-1-95: NRBF2-MIT=1: 1, molar ratio). (B) ^{1}H-^{15}N NMR spectra of ^{15}N-labeled Atg14L-1-95 alone (black spots) and that of after titrating with NRBF2-MIT (red spots) (^{15}N-labeled Atg14L-1-95: NRBF2-MIT=1: 8, molar ratio).

5.3 Investigate the interaction between NRBF2 and phosphorylated Atg14L N-terminal

Given it was failed to find the interaction between NRBF2 and the N-terminal of Beclin1 or Atg14L by ITC assay and NMR spectrum, we were curious whether post-translational modification for Atg14L is required for its binding to NRBF2. Several studies have reported that upon starvation signal, the N-terminal region of Atg14L, would become phosphorylated to promote autophagy (Park *et al.*, 2016,Wold *et al.*, 2016). Thus, five Atg14L mutants (residues1-95, S61E, S83E, S61E_S83E, T48E_T49E_T54E, 5E) that mimic phosphorylation by replacing the threonine residue or serine residue with the glutamate residue were generated for assessing their interaction with NRBF2 by ITC assay. However, as shown in Figure 5.5, we still failed to detect the interaction between these Atg14L constructs and NRBF2-FL, as well as NRBF2-MIT, suggesting that phosphorylation status of Atg14L N-terminal is not related to its interaction with NRBF2.

A

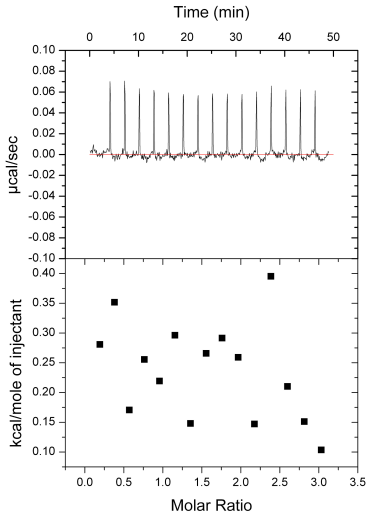

ATG14L-1-95 S61E to NRBF2-FL

B

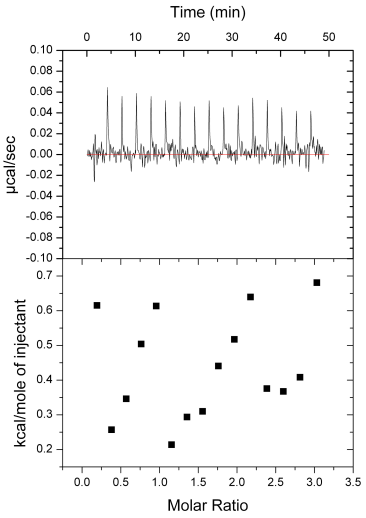

ATG14L-1-95 S83E to NRBF2-FL

C

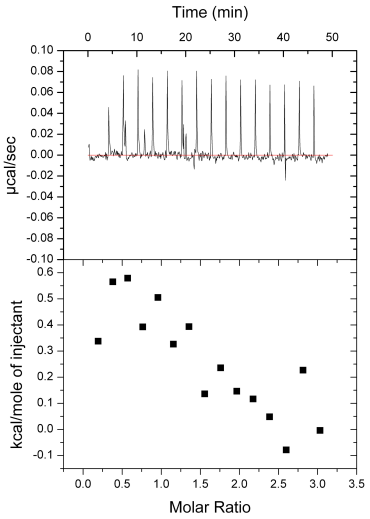

ATG14L-1-95 S61E_S83E to NRBF2-FL

D

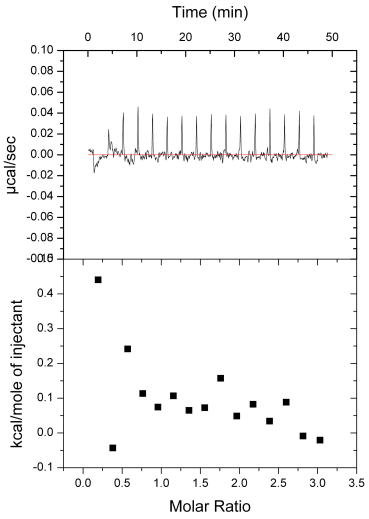

ATG14L-1-95 T48E_T49E_T54E to NRBF2-FL

E

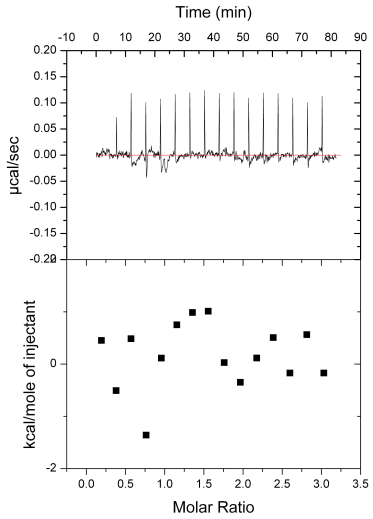

ATG14L-1-95 5E to NRBF2-FL

F

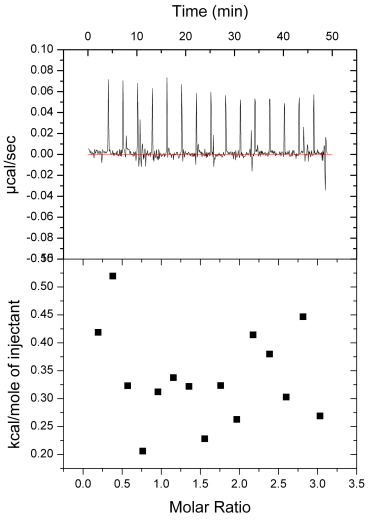

ATG14L-1-95 S61E to NRBF2-MIT

G

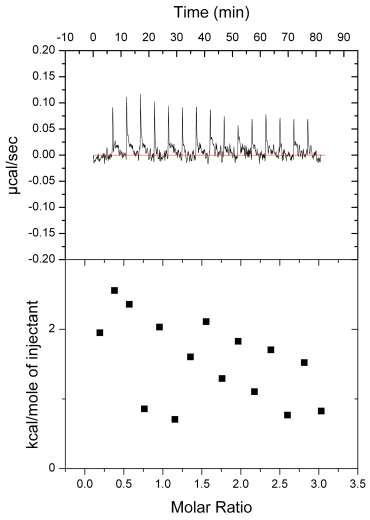

ATG14L-1-95 S83E to NRBF2-MIT

H

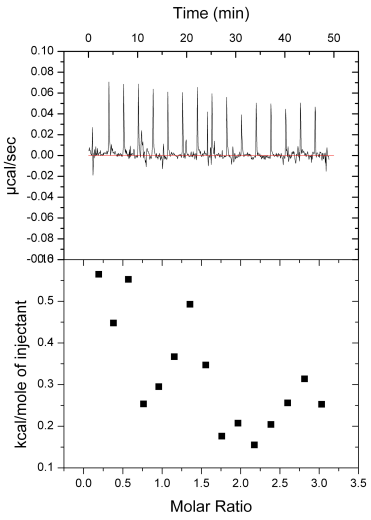

ATG14L-1-95 S61E_S83E to NRBF2-MIT

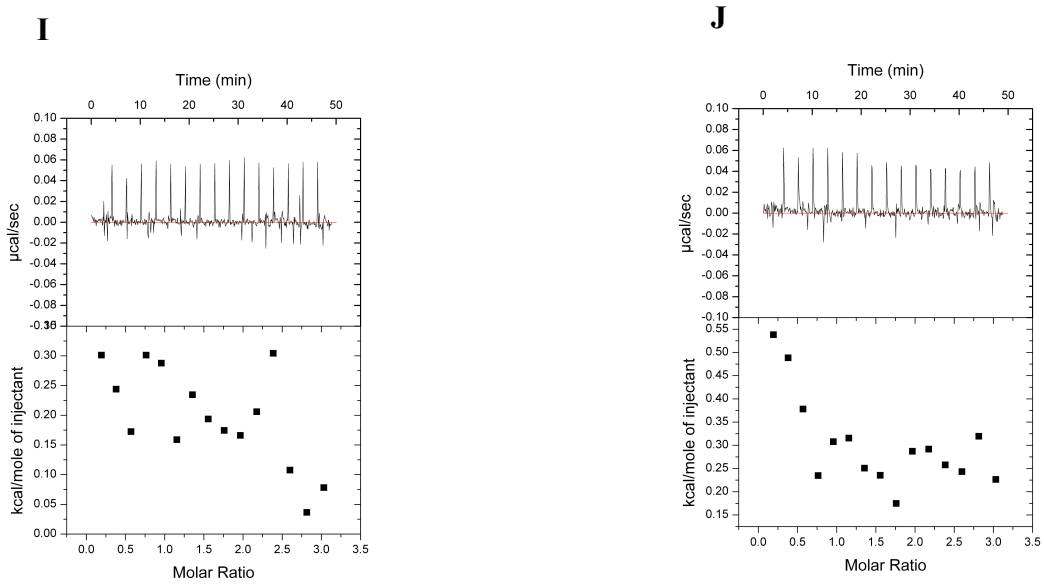

Figure 5.5 Characterization the interaction between NRBF2 and phosphorylated Atg14L N-terminal by ITC. (A-E) The ITC profiles of titrating phosphorylated Atg14L constructs to NRBF2-FL, suggesting there is no interaction between these Atg14L constructs and NRBF2-FL. (F-J) The ITC profiles of titrating phosphorylated Atg14L constructs to NRBF2-MIT, suggesting there is no interaction between these Atg14L constructs and NRBF2-MIT.

Taken together, in this chapter, we generated a large collection of NRBF2, Atg14L and Beclin1 constructs and employed multiple experimental methods including ITC and NMR titration to characterize possible interaction between NRBF2 and Atg14L as well as Beclin1 *in vitro*. Despite our hard work, we failed to confirm either the NRBF2-Beclin1 interaction or the NRBF2-Atg14L interaction.

A major goal of this project is to understand the molecular mechanism of how

NRBF2 specifically associates with the Atg14L-containing PI3KC3 complex I but not the UVRAG-containing complex II. Our initial hypothesis was that NRBF2 might have direct and specific interaction with Atg14L, thus acting as a secondary modulator of the Atg14L-containing PI3KC3 complex I. However, our studies in this chapter has ruled out this possibility.

During the course of our study, two papers related to structural studies of NRBF2 and the yeast homolog Atg38 were published. The NRBF2 paper by Young *et al.* didn't confirm the NRBF2-Atg14L interaction (Young *et al.*, 2016). Instead it used negative stain EM studies to show that NRBF2 is positioned at the base of the V-shaped complex I in close proximity to Vps15 and Vps34. Additionally, the position of NRBF2 within the complex I is similar to that occupied by the C2 domain of UVRAG in complex II. Thus an alternative hypothesis to explain why NRBF2 only associates with complex I but not complex II might be the mutual exclusivity between NRBF2 and UVRAG. In particular, both NRBF2 and UVRAG might compete for the same binding region at the base of V-shaped architecture of PI3KC3 complex. However, because of the low-resolution data from the negative stain EM analysis, the NRBF2 paper couldn't identify the exact binding site of NRBF2 at the base of the V-shaped architecture of complex I. It is possible that either Vps15 or Vps34 alone or both of them are involved in NRBF2 association. Furthermore, HDX data from both the NRBF2 paper and the Atg38 paper by Ohashi *et al.* showed that multiple regions of Vps34 and Vps15 would have their HDX exchange rate affected by NRBF2 binding. Additionally, these affected regions

are not exclusively located on the base of the V-shaped architecture, some of them are located at the kinase domain of Vps34 or helical domain of Vps15 (Ohashi *et al.*, 2016).

Combining our negative ITC and NMR data with the findings from the NRBF2 paper by Young *et al.* and Ohashi *et al.*, we revised our hypothesis that NRBF2 specifically interacts with the Atg14L-containing PI3KC3 complex I because NRBF2 competes with the C2 domain of UVRAG in terms of interacting with Vps34 and/or Vps15 at the base of the V-shaped architecture of PI3KC3 complex. As a result, NRBF2 is only suitable for the Atg14L-containing complex I but not the UVRAG-containing complex II.

With the revised hypothesis, we then proceeded to conduct cell-based experiments to confirm our new proposal. The findings are reported in the following chapter.

Chapter 6: Cell-based analysis to assess the impact of NRBF2 on complex I *vs.* complex II

Based on our studies in the previous chapters, we have revised our hypothesis why NRBF2 specifically binds to Atg14L-containing Beclin1-Vps34 complex I, but not UVRAG-containing complex II. We reason that NRBF2 may compete with UVRAG in terms of binding to Vps15 within the core unit of Beclin1-Vps34 complex. In particular, NRBF2 and the C2 domain of UVRAG may associate with the same region of Vps15, hence leading to mutual exclusivity. To test our hypothesis, we have conducted a series of Co-IP experiments using constructs covering both full-length and individual domains of NRBF2 and UVRAG.

6.1 NRBF2 and UVRAG are competitive binding partners for Vps15

6.1.1 UVRAG outcompetes NRBF2 in terms of binding to Vps15

Flag-tagged NRBF2 and GFP-tagged UVRAG were transiently transfected into HEK293T cells for assessing their binding affinity for endogenous Vps15 and Vps34. Our data shows that both Vps15 and Vps34 can be pulled down by NRBF2, either in presence or absence of UVRAG over-expression. However, the level of Vps15 immunoprecipitated by NRBF2 decreased upon UVRAG overexpression, while the level of Vps34 remained largely the same (Figure 6.1 A). These results suggest that NRBF2 competes with UVRAG for binding to Vps15, but not Vps34. We also

conducted similar Co-IP experiments using Flag-tagged UVRAG to pull down endogenous Vps15. Our results reveal that over-expression of NRBF2 had little effect on the amount of Vps15 pulled down by UVRAG (Figure 6.1 B). This data suggests that NRBF2 cannot outcompete UVRAG in terms of binding to endogenous Vps15.

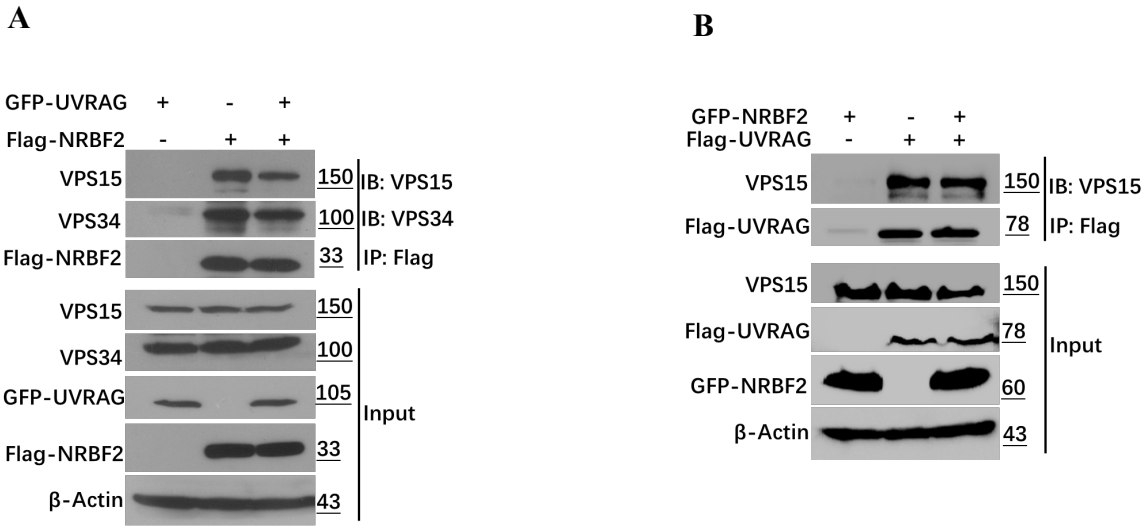

Figure 6.1 Characterization *in vivo* potency of binding endogenous Vps15 between NRBF2 and UVRAG by competitive Co-IP assay.

6.1.2. Loss of the UVRAG C2 domain weakens its competitive advantage over NRBF2

As the Co-IP data has confirmed that UVRAG competes with NRBF2 for binding Vps15, we next proceed to investigate which domain of UVRAG is responsible for such competition. According to the cryo-EM structure of NRBF2-containing PI3KC3 complex I (Young *et al.*, 2016), NRBF2 is located at the base of the V-shaped complex I, close to the N termini of Beclin1 and Atg14L. Comparing to the structure of UVRAG-

containing PI3KC3 complex II, it seems that NRBF2 MIT domain occupies the same position as UVRAG C2 domain, so it is possible that UVRAG competes with NRBF2 for binding Vps15 through its C2 domain. To test this hypothesis, the GFP-tagged constructs of UVRAG wild type (WT) and C2 domain deletion (d-C2) were co-transfected with Flag-tagged NRBF2 to HEK293T cells and their competitive binding to endogenous Vps15 was assessed by Co-IP. The results show that, over-expression of UVRAG-WT reduced the amount of Vps15 pulled down by NRBF2, while no such reduction was observed under over-expression of UVRAG-d-C2 (Figure 6.2). This data confirms that the C2 domain of UVRAG is indispensable for the competitive advantage of UVRAG over NRBF2.

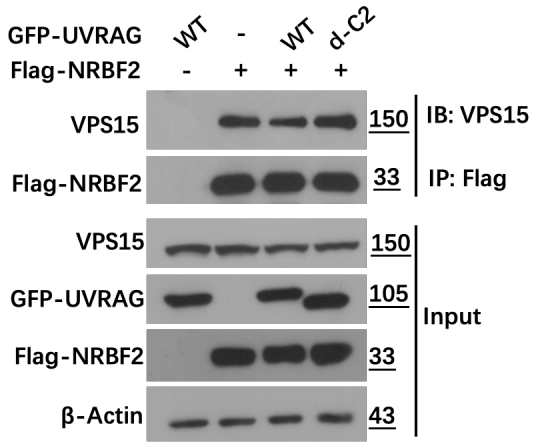

Figure 6.2 Characterization the functional domain of UVRAG C2 domain for binding to Vps15 by competitive by Co-IP assay.

6.1.3 Mutations in the UVRAG CC domain to weaken the Beclin1-UVRAG interaction render UVRAG uncompetitive against NRBF2

Previous studies from our lab have shown that Atg14L and UVRAG compete for Beclin1 binding via their respective CC domains (Li *et al.*, 2012). Additionally, our crystal structure of the Beclin1-UVRAG coiled-coil complex reveals a heterodimeric interface consisting of multiple 'leucine-zipper' pairings between Beclin1 and UVRAG. Furthermore, the competitive advantage of UVRAG over Atg14L in terms of Beclin1 binding can be gradually weakened by mutating the leucine residues of UVRAG at the Beclin1-UVRAG interface (Wu *et al.*, 2018). We wonder if the competition between UVRAG and Atg14L for Beclin1 would also affect the competition between UVRAG and NRBF2 for Vps15.

To answer this question, we decided to make use of the UVRAG-1E and UVRAG-6E mutants generated in our previous study (Wu *et al.*, 2018). For UVRAG-1E, one leucine residue Leu246 was mutated to glutamate. For UVRAG-6E, six leucine residues Leu232, Leu239, Leu246, Leu250, Leu264, Leu271 were all mutated to glutamate. Previous ITC and Co-IP results confirmed that UVRAG-1E was largely similar to UVRAG-WT in terms of binding affinity to Beclin1 *in vitro* and competitive advantage over Atg14L *in vivo*. In contrast, UVRAG-6E showed no binding to Beclin1 *in vitro* and lost competitive advantage over Atg14L *in vivo*.

To probe the relationship between UVRAG-Atg14L competition and UVRAG-

NRBF2 competition, we co-transfected Flag-tagged NRBF2 with GFP-tagged UVRAG-WT, UVRAG-1E and UVRAG-6E respectively. The competition between NRBF2 and different UVRAG constructs in terms of binding to endogenous Vps15 was assessed by Co-IP. Our results show that the amount of endogenous Vps15 pulled down by NRBF2 is significantly reduced upon over-expression of UVRAG-WT or UVRAG-1E, similar to our findings in previous chapters. However, over-expression of UVRAG-6E didn't reduce the amount of Vps15 pulled down by NRBF2, suggesting that the UVRAG-Atg14L competition over Beclin1 directly affects the UVRAG-NRBF2 competition for Vps15 (Figure 6.3). In fact, the UVRAG-Atg14L competition over Beclin1 likely dominates over the UVRAG-NRBF2 competition for Vps15.

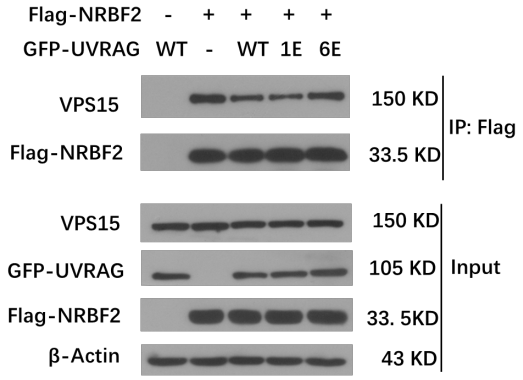

Figure 6.3 Characterization *in vivo* potency of binding endogenous Vps15 between UVRAG mutants and NRBF2 by competitive Co-IP assay.

.

6.2 The MIT domain of NRBF2 is indispensable for its binding to Vps15

We subsequently investigated the roles of different structural domains of NRBF2 in regulating its interaction with Vps15. Accordingly, the NRBF2 constructs that delete

the CC domain (NRBF2-d-CCD) and the MIT domain (NRBF2-d-MIT) were generated respectively. Then Flag-tagged NRBF2-WT, NRBF2-d-CCD, NRBF2-d-MIT, and GFP- tagged UVRAG were respectively transfected into HEK293T cells for assessing their interaction between endogenous Vps15 by Co-IP assay. As shown in Figure 6.4 A, NRBF2-d-MIT almost failed to pull down endogenous Vps15. For the NRBF2-d-CCD construct, it did pull down endogenous Vps15 but the amount is noticeably reduced as compared to NRBF2-WT. Similar trend was observed in presence of UVRAG overexpression, but the amount of Vps15 pulled down by NRBF2-WT and NRBF2-d-CCD constructs was further reduced because of the UVRAG competition (Figure 6.4 B). Taken together, these data indicate that the MIT domain of NRBF2 is absolutely required for Vps15. In contrast, the CC domain of NRBF2 is dispensable for Vps15 binding although it can enhance the abundance of this interaction.

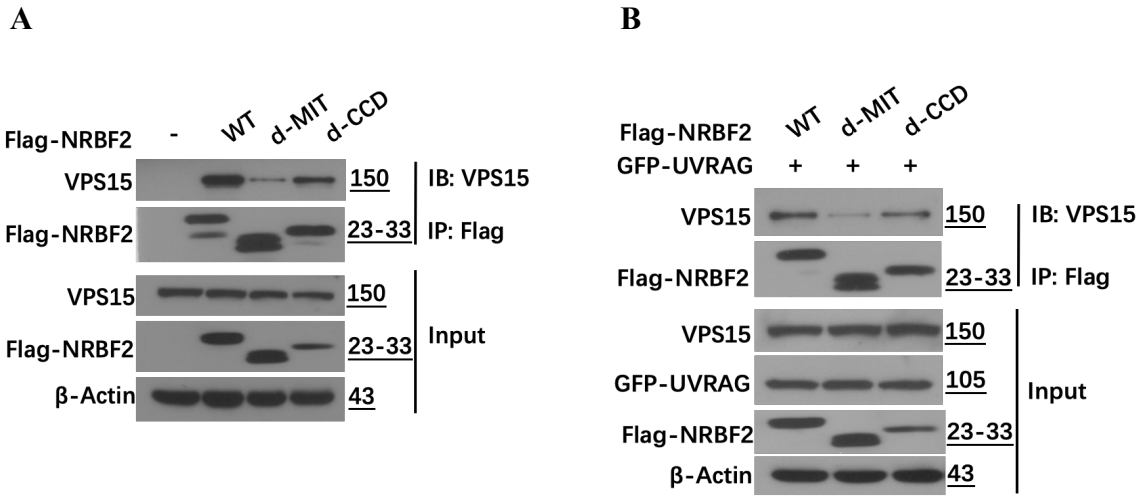

Figure 6.4 Characterization the functional domain of NRBF2 for binding to Vps15 by Co-IP assays. (A) Characterization *in vivo* potency of binding endogenous Vps15 between NRBF2-WT and NRBF2 domain deletion constructs. (B) Characterization *in vivo* potency of binding endogenous Vps15 between NRBF2-WT and NRBF2 domain

deletion constructs in face of UVRAG competition.

6.3. The CC domain of NRBF2 is critical for its competition with UVRAG

Based on the finding that NRBF2 CC domain is beneficial for its binding to Vps15, we reason that the oligomeric state of CC domain may be a critical factor for enhancing the NRBF2-Vps15 interaction.

6.3.1. Mutations in the CC domain to generate monomeric and tetrameric NRBF2 constructs

To verify our hypothesis, a series of NRBF2 constructs with various oligomeric states were generated. For the monomeric construct, the NRBF2-5A as described in chapter 4.6 was employed for the Co-IP assay to compare its binding affinity for endogenous Vps15 with the dimeric NRBF2-WT. In terms of the NRBF2 constructs with higher oligomeric state, we decided to make use of the CC domain of yeast transcription factor GCN4, a well-studied model system for coiled-coil structures. Based on the structural information of GCN4 at high resolution, it is well known that the preferred oligomerization state of GCN4 leucin zipper can be changed from dimeric (GCN4-P1) to trimeric or tetrameric (GCN4-P-L1) when the amino acids in the *a* and *d* position were mutated accordingly. Following these observations, we engineered an artificial NRBF2 dimer (NRBF2-GCN4-dimer) as well as a NRBF2 tetramer (NRBF2-GCN4-tetramer) by replacing the CC domain with GCN4-P1 and GCN4-P-L1

respectively.

Firstly, the oligomeric states of NRBF2-GCN4-dimer and NRBF2-GCN4-tetramer were characterized *in vitro*. The constructs NRBF2-GCN4-dimer and NRBF2-GCN4-tetramer were expressed in *E. coli,* and proteins of high purity were obtained via the general purification procedure described previously. Subsequently, light scattering was used to investigate the oligomeric states of these two proteins. The results show the measured molecular weights of NRBF2-GCN4-dimer and NRBF2-GCN4-tetramer are 63.8kDa and 123.8kDa (Figure 6.5 A and B), and the theoretical molecular weights of these two constructs are both around 31kDa, indicating these two constructs form a dimer and a tetramer respectively as expected.

A

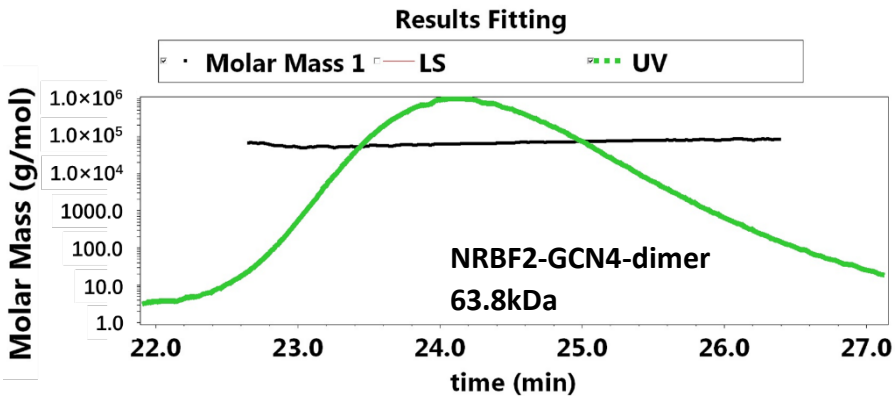

B

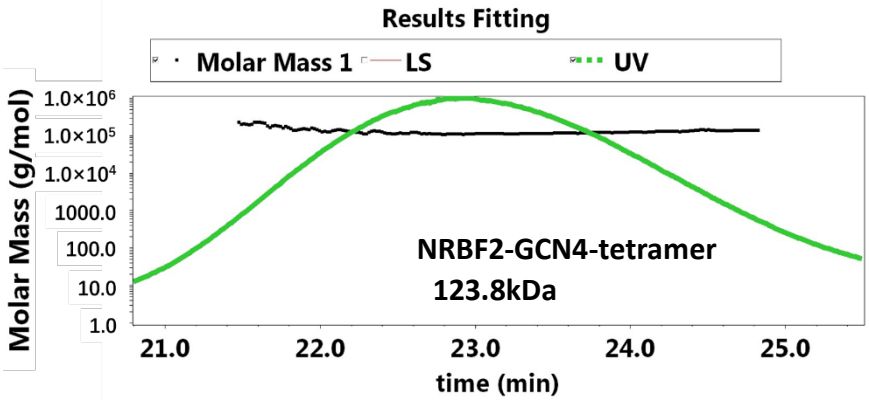

Figure 6.5 Characterization the oligomeric states of NRBF2-GCN4-dimer and NRBF2-GCN4-tetramer by light scattering.

6.3.2 Monomeric NRBF2 shows weakened competition with UVRAG in terms of binding to Vps15

We firstly compared the binding affinity for endogenous Vps15 between the dimeric NRBF2-WT and the monomeric NRBF2 mutant (NRBF2-5A). Flag-NRBF2-WT and Flag-NRBF2-5A mutant were transfected into HEK293T cells, and the cells were collected and lysed after 48 hours expression. The binding affinity of NRBF2-WT and NRBF2-5A for Vps15 were characterized by Co-IP, and the results show the levels of Vps15 pulled down by dimeric NRBF2-WT and that by monomeric NRBF2-5A were similar (Figure 6.6 A), while under UVRAG overexpression, monomeric NRBF2-5A pulled down much less Vps15 compared to NRBF2-WT (Figure 6.6 B), indicating the disruption of NRBF2 self-association weakened its competitiveness for binding Vps15 in face of UVRAG overexpression.

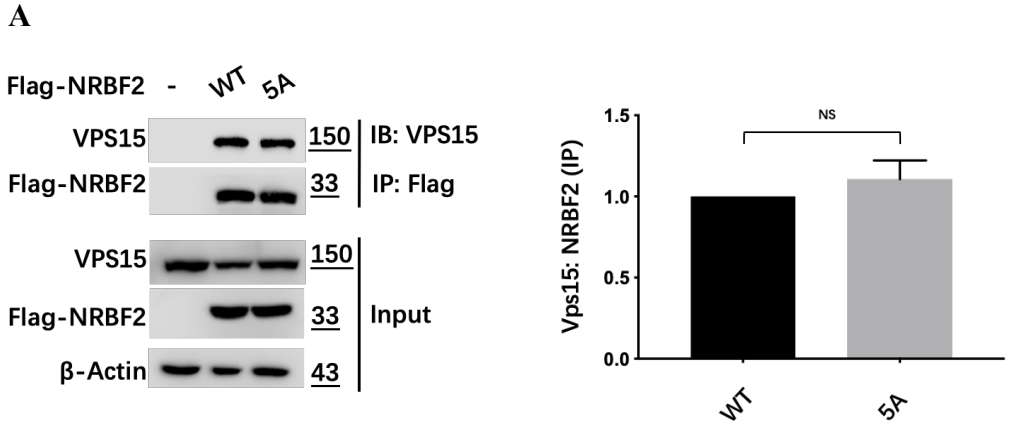

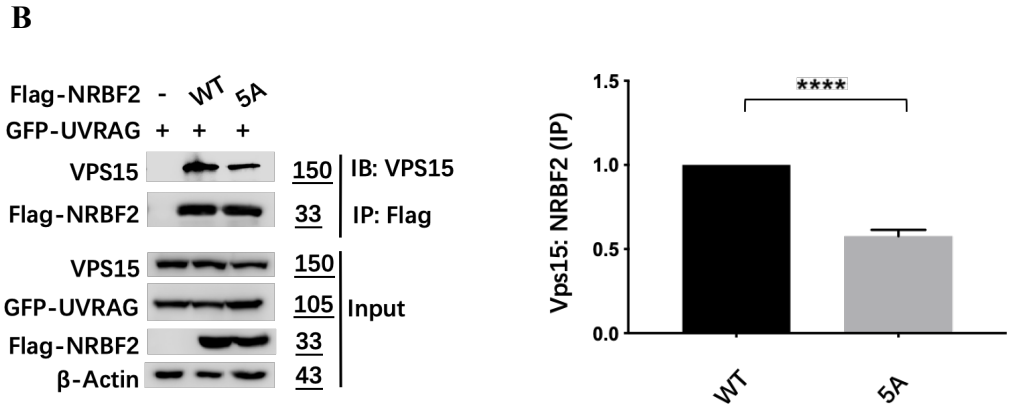

Figure 6.6 Investigating the effects of the oligomeric state of NRBF2 on the NRBF2-Vps15 interaction by Co-IP assays and corresponding histograms. (A) Co-IP experiment to measure the amount of endogenous Vps15 pulled down by transient transfection of Flag-tagged NRBF2-WT and 5A mutant in HEK293T cells. (B) Co-IP experiment to measure the amount of endogenous Vps15 pulled down by transient co-transfection of Flag-tagged NRBF2-WT or 5A mutant with GFP-tagged UVRAG in HEK293T cells.

6.3.3. Tetrameric NRBF2 shows strengthened competitive advantage over UVRAG in terms of binding to Vps15

So far, our Co-IP data have confirmed that the dimeric NRBF2-WT is more competitive than the monomeric NRBF2-5A mutant in terms of competing against UVRAG for Vps15 binding. For the next step, we assessed the competitiveness of the NRBF2-GCN4-dimer and NRBF2-GCN4-tetramer constructs by Co-IP. The results showed that, in presence of over-expressed UVRAG, NRBF2-WT and NRBF2-GCN4-

dimer pulled down similar amount of Vps15. Interestingly, the level of Vps15 pulled down by NRBF2-GCN4-tetramer is almost doubled compared to the two dimeric NRBF2 constructs. Taken together, these results confirm our hypothesis that NRBF2 with higher oligomeric state is more competitive against UVRAG in terms of binding to Vps15. It is possible that the oligomeric state of NRBF2 as mediated by its CC domain is beneficial for its binding to Vps15 because it effectively enhances the local abundance of MIT domain to promote the interaction between NRBF2 and Vps15.

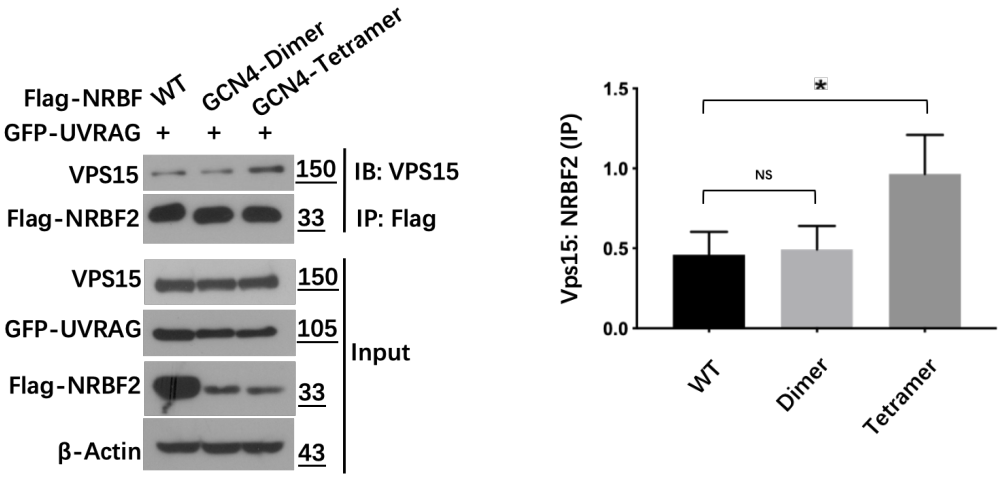

Figure 6.7 Investigating the effects of the oligomeric state of NRBF2 on the NRBF2-Vps15 interaction in face of UVRAG competition by Co-IP assay and corresponding histogram.

6.4 The competition between NRBF2 and UVRAG doesn't affect the Beclin1-Atg14L interaction

Our previous studies have shown that, for the competition between Atg14L and UVRAG in terms of Beclin1 binding, UVRAG is the stronger binding partner and readily outcompetes Atg14L *in vivo*. For our NRBF2 study, we have demonstrated that

NRBF2 competes with UVRAG in terms of binding to endogenous Vps15. Given that UVRAG is engaged in two competitions, we wonder if the NRBF2: UVRAG competition would have any effect on the Atg14L: UVRAG competition.

To address this question, GFP-NRBF2, GFP-UVRAG, and Flag-Atg14L were transiently transfected into HEK293T cells. Cells were collected and lysed 48 hours post-transfection for Co-IP assay. As shown in Figure 6.8 A, Flag-Atg14L pulled down significant amount of endogenous Beclin1 but barely did so in presence of over-expressed GFP-UVRAG. This data is in agreement with our previous findings that Atg14L is less competitive than UVRAG in terms of binding to endogenous Beclin1. We then repeated the Co-IP experiments in presence of over-expressed NRBF2. Our data shows that similar amount of endogenous Beclin1 was pulled down by Atg14L either in absence or presence of over-expressed NRBF2, suggesting that the NRBF2: UVRAG competition for endogenous Vps15 doesn't affect the Atg14L: UVRAG competition for Beclin1 (Figure 6.8 B).

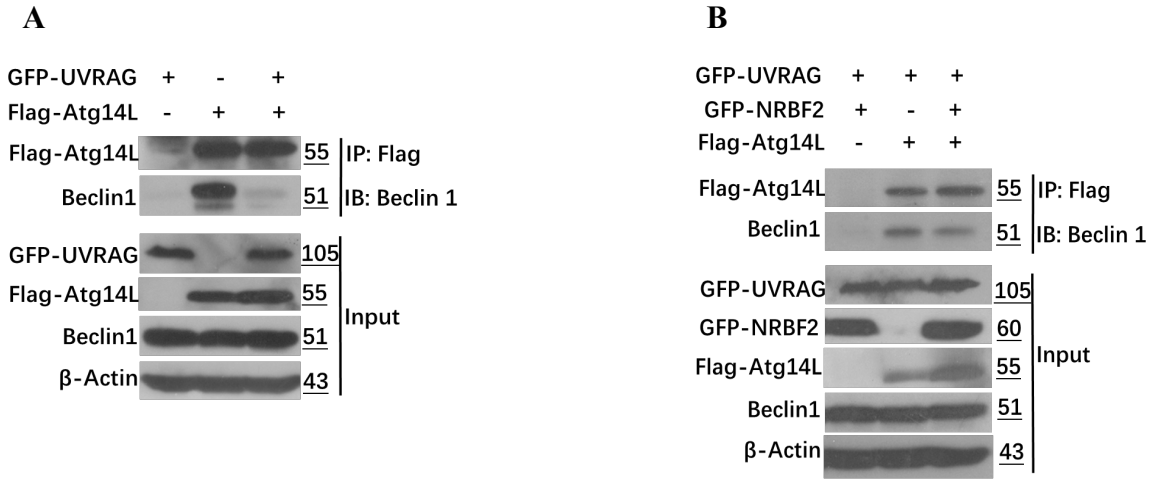

Figure 6.8 Investigating the effects of NRBF2 on the Atg14L: UVRAG competition

for endogenous Beclin1 by Co-IP assays. (A) Competitive Co-IP assay to characterize *in vivo* potency of binding endogenous Beclin1between Atg14L and UVRAG. (B) NRBF2 was additionally expressed to probe its effects on the binding between Atg14L and Beclin1 in face of UVRAG competition.

6.5 The competition between NRBF2 and UVRAG doesn't affect the Atg14L-Vps15 interaction

6.5.1 The competition between NRBF2 and UVRAG doesn't affect the Atg14L-Vps15 interaction (under normal condition)

As NRBF2 does not enhance Atg14L's binding for Beclin1 in face of UVRAG competition, we next examined the idea whether NRBF2 affects Atg14L's competitive binding for other two members in the PI3KC3 complex, Vps15 and Vps34, in face of UVRAG overexpression. Firstly, the Co-IP assay confirmed that both Atg14L and UVRAG could pull down Vps15 and Vps34 (Figure 6.9 A). But the level of Vps15 and Vps34 pulled down by Atg14L was significantly reduced in presence of UVRAG overexpression (Figure 6.9 B). Given that Atg14L doesn't have extensive interactions with either Vps15 or Vps34 as shown by X-ray and cryo-EM studies, it is possible the observed competition between Atg14L and UVRAG for endogenous Vps15/Vps34 was actually for Beclin1 instead.

We then repeated these competitive Co-IP experiments in presence of over-

expressed NRBF2. Our data shows that the addition of NRBF2 didn't enhance the amount of Vps15/Vps34 pulled down by Atg14L, regardless of whether UVRAG was over-expressed or not (Figure 6.9 C and D). These results are consistent with the findings of the previous sections, i.e. NRBF2 does not affect the Atg14L: UVRAG competition for Beclin1, hence it doesn't affect the Atg14L- Vps15/Vps34 interaction mediated by Beclin1 either.

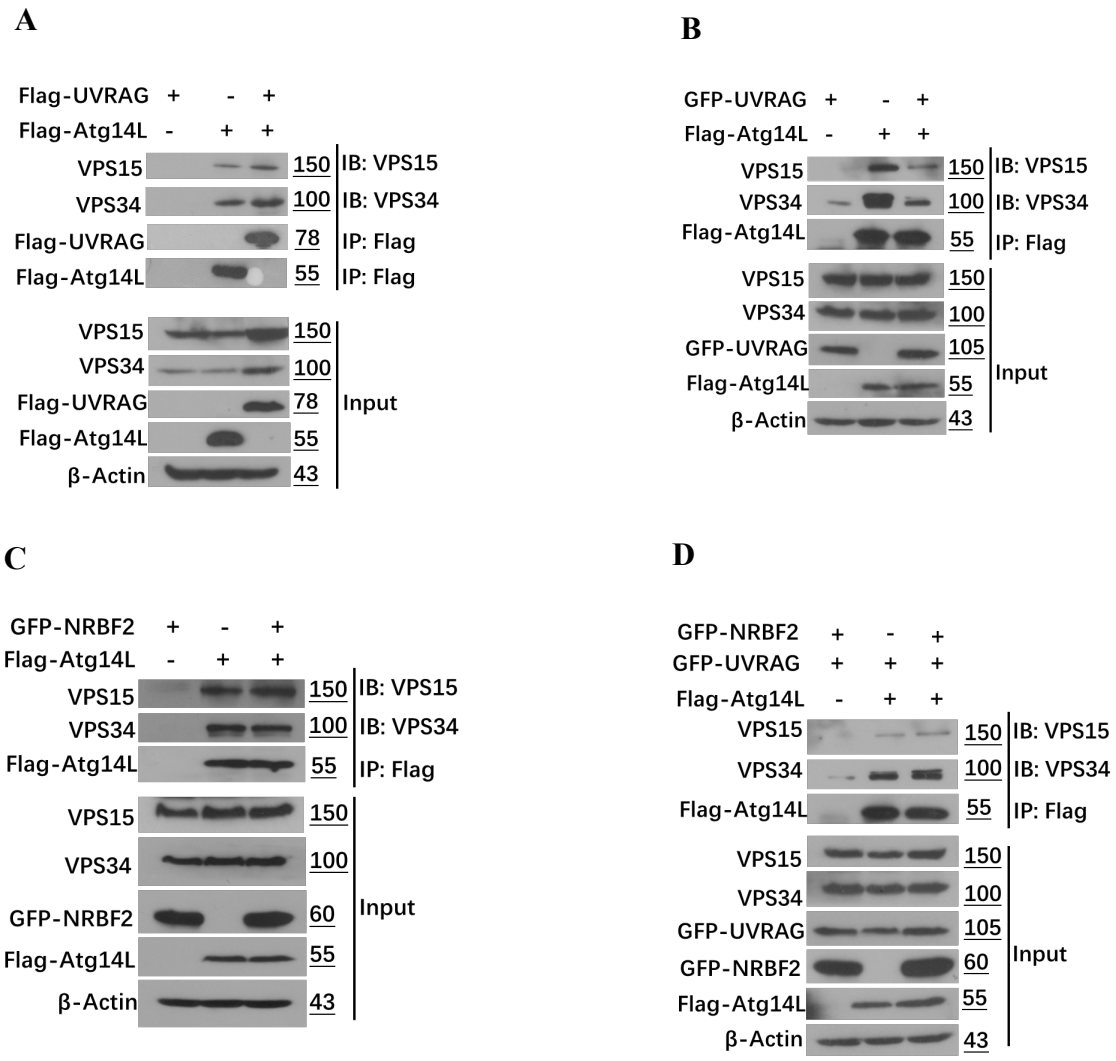

Figure 6.9 Investigating the effects of NRBF2 on the Atg14L: UVRAG competition for endogenous Vps15/Vps34 under normal condition by Co-IP assays. (A) Co-IP assay shows that both Atg14L and UVARG binds to Vps15/Vps34. (B) Competitive

Co-IP assay to characterize *in vivo* potency of binding endogenous Vps15/Vps34 between Atg14L and UVRAG. (C) The effects of NRBF2 overexpression on the binding between Atg14L and Vps15/Vps34. (D) The effects of NRBF2 overexpression on the binding between Atg14L and Vps15/Vps34 in face of UVRAG competition.

6.5.2 The competition between NRBF2 and UVRAG doesn't affect the Atg14L-Vps15 interaction (under EBSS starvation and rapamycin treatment)

It was reported previously that NRBF2 can induce autophagy more significantly under starvation or rapamycin treatment than under normal condition (Lu *et al.*, 2014). Besides, it has been reported that NRBF2 becomes dephosphorylated upon nutrient starvation and only this dephosphorylated form can upregulate the kinase activity of PI3KC3 complex I and enhance autophagy flux (Ma *et al.*, 2017). Taking note of this finding, we wondered if our Co-IP results would be different if conducted under starvation condition. To address this question, GFP-NRBF2, GFP-UVRAG, and Flag-Atg14L were transfected into HEK293T cells accordingly. Rapamycin (100nM) treatment and EBSS starvation were conducted respectively for five hours before cells were collected for subsequent Co-IP assay. The results were shown in Figure 6.10. Similar to the results under normal condition, NRBF2 did not o enhance the interaction between Atg14L and Vps15/Vps34 in face of UVRAG competition either under starvation or after rapamycin treatment.

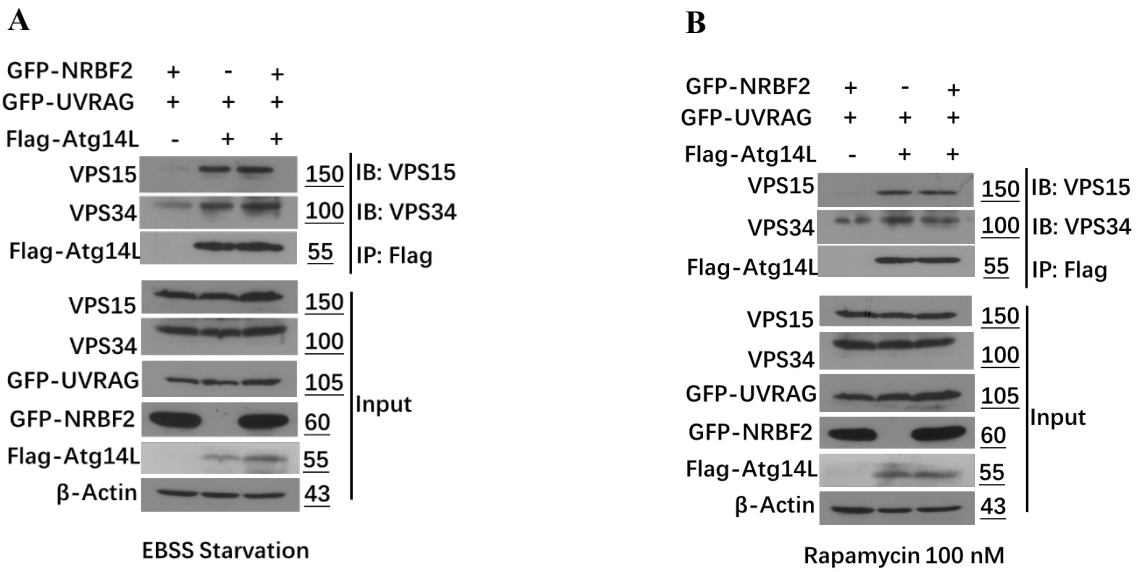

Figure 6.10 Investigating the effects of NRBF2 on the Atg14L: UVRAG competition for endogenous Vps15/Vps34 under EBSS starvation (A) or rapamycin treatment (B).

Chapter 7: Cell-based studies to investigate the functional significance of NRBF2 CC domain in autophagy regulation

So far, several studies have reported consistent results that NRBF2, or the yeast homology Atg38, plays a positive role in regulating autophagy (Zhong *et al.*, 2014,Cao *et al.*, 2014,Lu *et al.*, 2014). However, one paper showed contradictory results with NRBF2 exerting negative effect on autophagy (Zhong *et al.*, 2014). Here, we used cell-based autophagy assays to further investigate the regulatory role of NEBF2 on cellular autophagic activity. In particular, we are interested in delineating the roles of MIT domain, investigated the role of each domain of NRBF2 in regulating autophagy, as well as the effects of NRBF2's oligomeric state on autophagy.

7.1 The role of NRBF2 in regulating p62 degradation and LC3 co-localization

To determine the role of NRBF2 in regulating autophagy, we investigated the effects of NRBF2 on standard autophagy markers including the autophagy substrate p62 and the lipidated form of protein light-chain 3 LC3-II. Firstly, the autophagic flux in mouse neuroblastoma Neuro-2a (N2a) WT and NRBF2 KO cells was characterized respectively. For N2a WT cells, EBSS starvation led to noticeable reduction of p62 level compared to normal condition. Similarly, the LC3-II level was significantly increased as well (Fig. 7.1A). These data confirm that starvation can readily induce autophagy in N2a WT cells. In contrast, for N2a NRBF2 knockout cells. EBSS starvation failed to induce reduction of p62 and no increase of LC3-II, suggesting that

autophagic response to starvation is impaired (Figure 7.1A). Furthermore, the level of endogenous p62 in N2a knockout cells under normal homeostatic condition is significantly higher than that in wild-type, and this elevation is readily rescued by transient over-expression of NRBF2 (Figure 7.1B). Taken together, our data suggest that NRBF2 plays a positive role in regulating autophagy, particularly in terms of regulating the level of endogenous p62 under normal and starvation conditions.

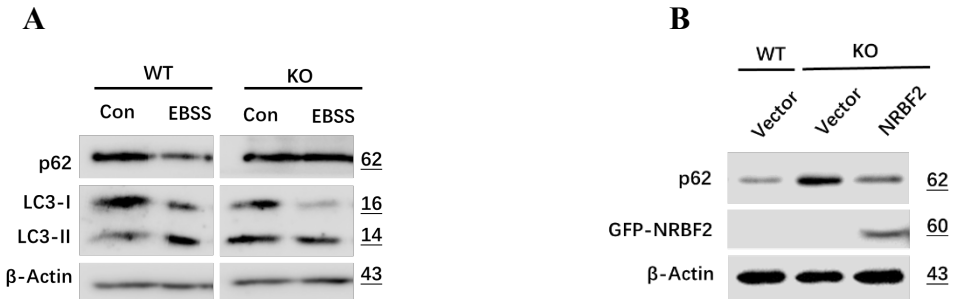

Figure 7.1 NRBF2 is a positive regulator in promoting p62 degradation. (A) Western blot to probe the autophagy fluxes in N2a WT cells and NRBF2 KO cells. (B) Western blot to probe the effect of NRBF2 on regulating p62 degradation.

Next, NRBF2-d-MIT and NRBF2-d-CCD were respectively transfected into NRBF2 KO N2a cells to probe the function of each domain in autophagy regulation. As shown in Figure 7.2, the overexpression of NRBF2-d-MIT failed to rescue the elevation of p62 level mediated by NRBF2 knockout, while the overexpression of NRBF2-d-CCD reduced the p62 level noticeably. In summary, these data show MIT domain of NRBF2 is responsible and indispensable for its function in promoting p62 degradation.

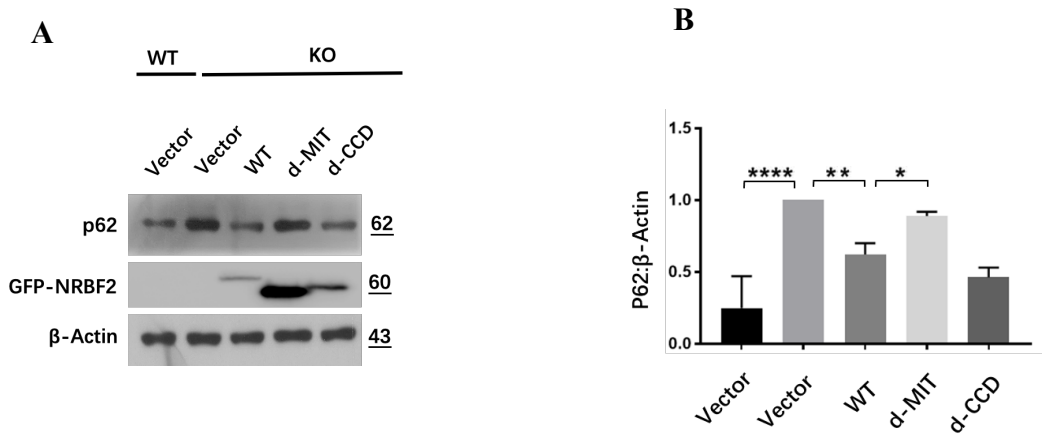

Figure 7.2 Characterization the role of NRBF2 functional domain in regulating p62 degradation by western blot (A) and corresponding histogram (B).

To better understanding the role of NRBF2 in autophagy, we next investigated the co-localization of NRBF2 and LC3 puncta by confocal. We used HeLa cells with stable expression of GFP-tagged LC3 for this study. Plasmids carrying mCherry-tagged NRBF2 WT, NRBF2-dMIT and NRBF2-dCCD were transfected into HeLa-GFP-LC3 cells respectively. After 24-48 hours expression, these cells were treated with rapamycin (100nM, 3hrs) and then processed for imaging study. As shown in Figure 7.3, the expression pattern of GFP-LC3 showed a diffusive pattern throughout the cell with distinct puncta in cytosol. For mCherry-tagged NRBF2, a similar punctate pattern was observed as well. Additionally, the puncta of GFP-LC3 and mCherry-NRBF2 overlapped well (Fig. 7.3). For mCherry-NRBF2-d-MIT construct, fewer puncta were observed as compared to NRBF2 wild-type, although the co-localization pattern with GFP-LC3 was maintained. For mCherry-NRBF2-d-CCD, the expression pattern was diffusive throughout the cytosol. As a result, its co-localization with GFP-LC3 puncta

was lost. Taken together, the imaging data suggest that both MIT domain and CC domain of NRBF2 are important for the punctate pattern of over-expressed NRBF2 in cytosol and its co-localization with GFP-LC3 puncta. In particular, CC domain is indispensable for the formation of NRBF2 puncta.

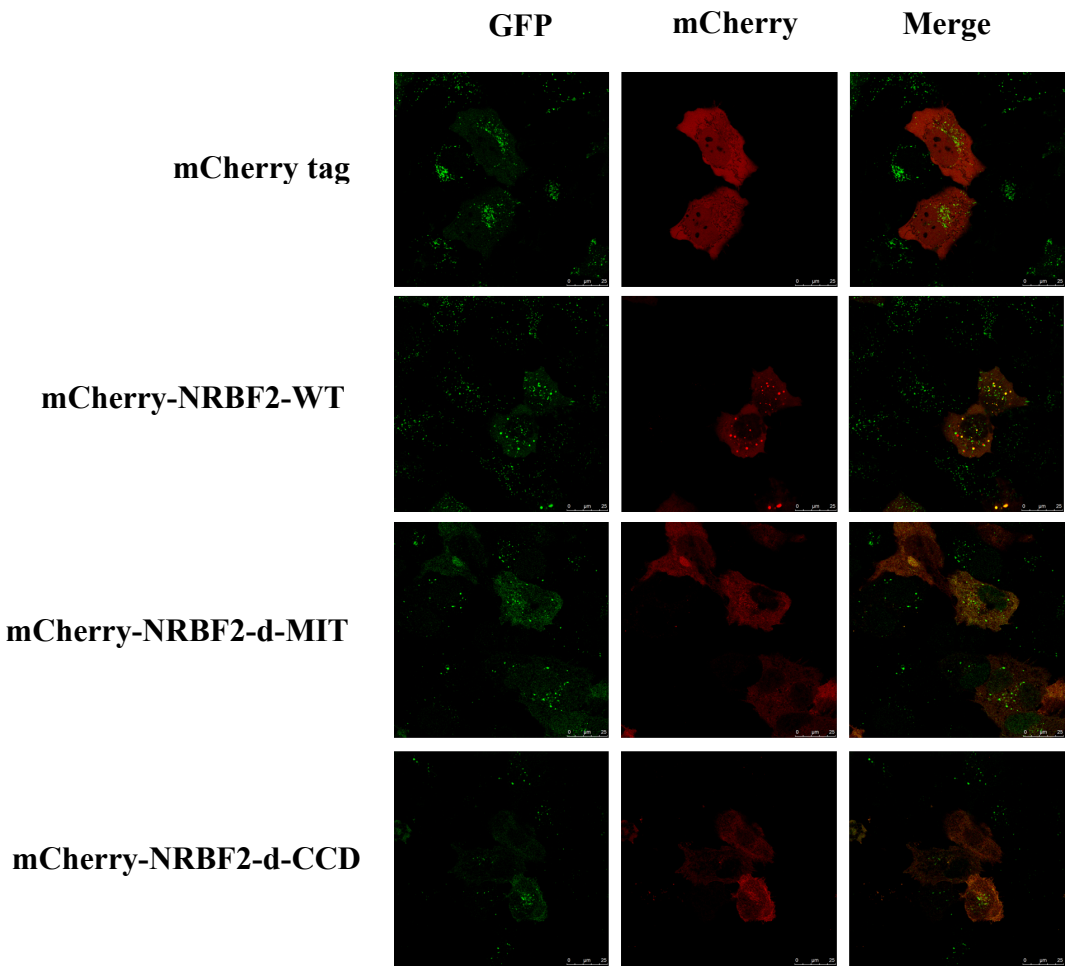

Figure 7.3 Characterization the effects of NRBF2's functional domain on its colocalization with LC3 puncta by confocal (rapamycin 100nM, 3hrs).

In our Co-IP studies in the previous chapter, we have demonstrated that the oligomeric state of NRBF2 affects its binding to endogenous Vps15. Now we would like to investigate whether the oligomeric state of NRBF2 affects its function in

regulating autophagy. NRBF2-WT and NRBF2 monomer mutants were transfected into N2a NRBF2 KO cells respectively for subsequent western blot assay. The result shows that while wild-type NRBF2 would rescue the elevated level of endogenous p62 in N2a NRBF2 knockout cells, monomeric mutants of NRBF2 failed to do so (Figure 7.4 A&B). We also investigated whether NRBF2 with engineered oligomeric state, i.e. NRBF2-GCN4-dimer and NRBF2-GCN4-tetramer would further enhance the rescue effect as compared to NRBF2-WT. As shown in Figure 7.4 C&D, NRBF2-GCN4-dimer exerted similar impact as compared NRBF2-WT in rescuing the elevated level of p62. Interestingly, NRBF2-GCN4-tetramer showed stronger impact in the rescue efficiency as compared to NRBF2-GCN4-dimer and NRBF2-WT. These results suggest that the oligomeric state of NRBF2 is beneficial for maintaining p62 turnover under homeostatic condition. Replacing the dimeric CC domain in NRBF2 with GCN-tetramer appears to bring additional benefit, probably because of its higher-order oligomeric state.

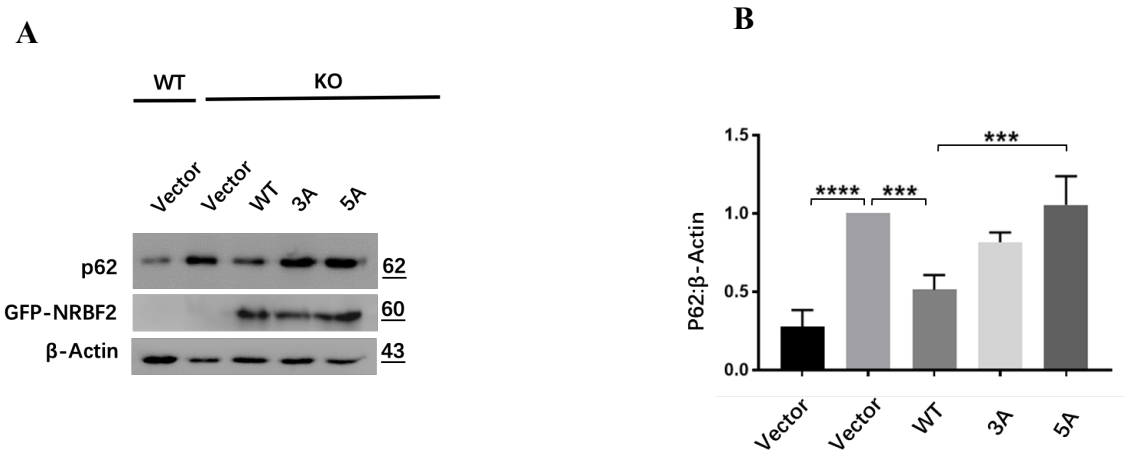

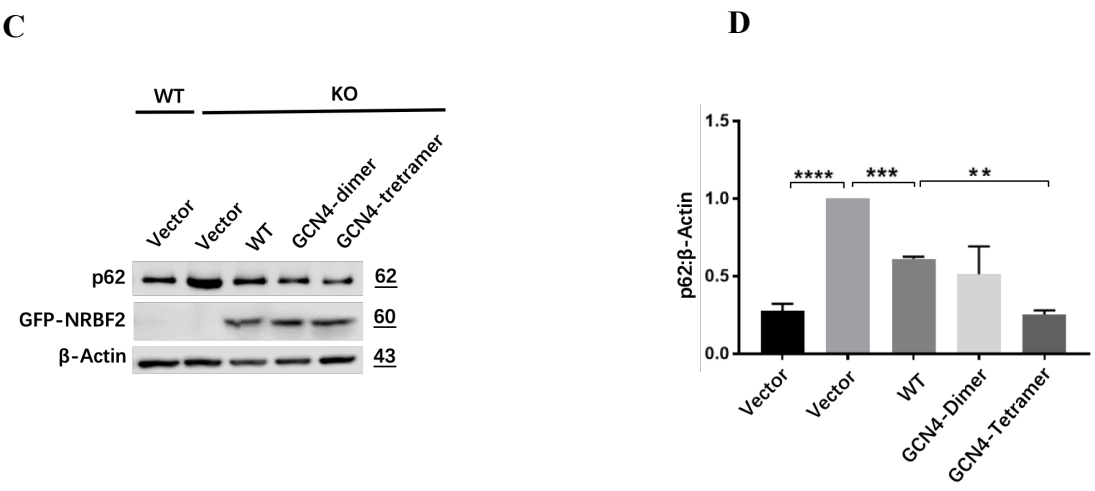

Figure 7.4 Characterization the roles of NRBF2 oligomeric state in regulating p62 degradation by western blot (A) and corresponding histogram (B).

Subsequently, the colocalization of LC3 puncta and these NRBF2 constructs were investigated. As shown in Figure 7.5, both monomeric (3A and 5A mutants) and oligomeric NRBF2 constructs with GCN4 modification showed intracellular distribution pattern as compared to NRBF2 wild type. For NRBF2-3A and 5A, their distribution pattern was totally diffusive with no puncta formed in cytosol. For NRBF2-GCN4-dimer and -tetramer, only large-sized puncta with no diffusive background visible. Besides, these puncta co-localize perfectly with GFP LC3 puncta. Additionally, NRBF2-GCN4-tetramer led to more puncta formation as compared to NRBF2-GCN4-dimer.

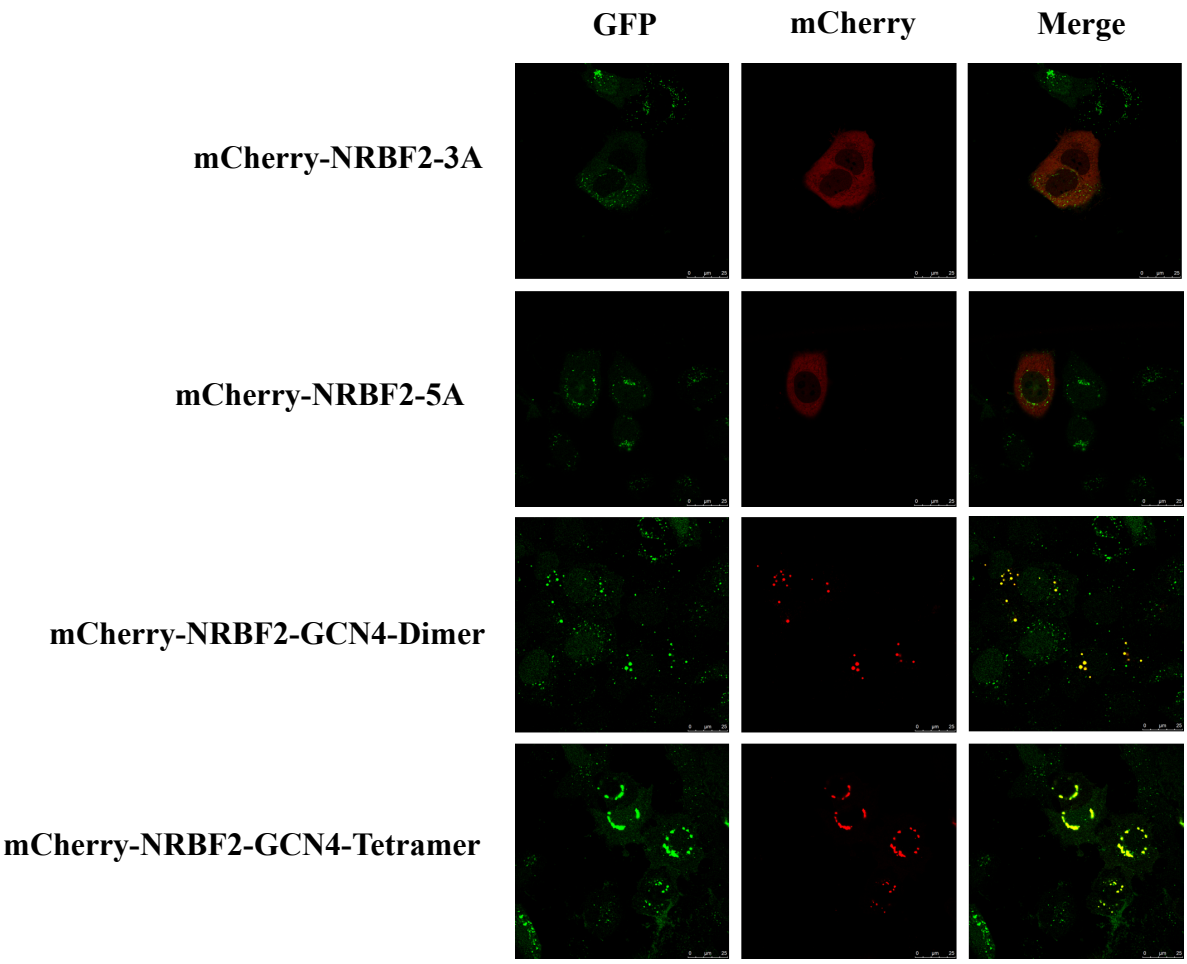

Figure 7.5 Characterization the effects of NRBF2's oligomeric state on its colocalization with LC3 puncta by confocal (rapamycin 100nM, 3hrs).

Taken together, our imaging studies reveal that the oligomeric state of NRBF2 as mediated by its CC domain is closely relative to its efficiency in promoting p62 degradation and its co-localization to GFP-LC3 puncta.

Chapter 8: Discussion and future studies

The Beclin1-Vps34 complex is a key component of the mammalian autophagy machinery. A notable feature of this complex is the large variety of biochemical compositions found *in vivo*. As the essential scaffolding protein within the complex, Beclin1 recruits either Atg14L or UVRAG in mutually exclusive manner, leading to the formation of the Atg14L-containing complex I or UVRAG-containing complex II. Besides Atg14L and UVRAG, a variety of modulating molecules have been reported to associate with either complex I or II to form biochemically and functionally distinct Beclin1-Vps34 subcomplexes so that the activity of Vps34 can be tightly regulated in response to specific cellular context (Funderburk *et al.*, 2010). How the endogenous pool of the Beclin1-Vps34 core complex is dynamically partitioned into these subcomplexes is not well understood.

NRBF2, the focus of my thesis study, is a newly identified critical regulator of the Atg14L-containing complex I. NRBF2 is essential for autophagy execution because it enhances the lipid kinase activity of complex I during the early stage of autophagy induction. The molecular mechanism of how NRBF2 specifically interacts with complex I and enhance its activity is not clear.

Two previous studies have provided some crucial information in terms of how NRBF2 associates with complex I. Through negative stain EM analysis, both studies have confirmed that NRBF2, or its yeast homolog Atg38, is located at the base of the

V-shaped complex I. Additionally, their HDX-MS profiling and Co-IP experiments suggest that the MIT domain of NRBF2 is indispensable for its association with complex I.

However, the two studies reported inconsistent findings regarding the CC domain of NRBF2 and how it affects the biochemical stoichiometry of the NRBF2-associated complex I. The study by Young et. al. stated that NRBF2 binds to the Atg14L-containing complex I with very high affinity and this strong interaction leads led to dimerization of complex I, i.e. the dimeric NRBF2 could link two copies of complex I, with each MIT domain engaging one complex I (Young *et al.*, 2016). However, the study of Ohashi et. al. reported that, for the yeast system, the homodimeric Atg38 only interacted with one copy of complex I. For mammalian system, the stoichiometry of NRBF2-associated complex I was variable and depended on the relative abundance of individual constituents (Ohashi *et al.*, 2016). In fact, the exact stoichiometry of NRBF2-associated complex I *in vivo* is unknown. The biological significance of different stoichiometric states, if any, is also not studied.

Here my thesis work has provided additional information to help delineate the molecular mechanism of NRBF2 with particular focus on the CC domain.

First of all, we determined the crystal structure of the CC domain of NRBF2. The structure reveals two straight helices wrapped around each other in parallel fashion,

conforming to the architecture of a canonical coiled-coil dimer. The dimer interface of NRBF2 contains multiple leucine-zipper pairings, rendering the dimeric structure highly stable. This structure with canonical coiled-coil interface is in stark contrast to the asymmetric coiled-coil dimer of Atg38, with one helix being straight and the other bent in the middle at an angle of approximately 40°. Given that Atg38 dimer is only associated with one copy of complex I while NRBF2 can link two copies of complex I, we are tempted to propose that the higher stability of the CC domain of NRBF2 is the reason for its ability to dimerize complex I.

Secondly, we used a series of Co-IP experiments to confirm that NRBF2 and UVRAG are mutually exclusive binding partners for endogenous Vps15. The competition between NRBF2 and UVRAG involves the MIT domain of NRBF2 and the C2 domain of UVRAG respectively because these two domains associate with similar areas of Vps15. Additionally, the oligomeric state of NRBF2 as determined by its CC domain also affects the NRBF2 *vs.* UVRAG competition. Using our structural findings as guidance, we mutated the hydrophobic leucine residues in the CC domain to alanine to generate monomeric NRBF2 constructs. By replacing the CC domain with the GCN4 tetramer, we also obtained tetrameric NRBF2. For the monomeric, dimeric and tetrameric NRBF2 CC constructs we generated, monomeric NRBF2 is the least competitive against UVRAG in terms of binding to Vps15. Dimeric construct is better while the tetrameric construct is most competitive. These results uncover a previously unappreciated role for the CC domain in terms of enhancing NRBF2's competitiveness

against UVRAG for Vps15 binding.

Furthermore, we also used competitive Co-IP to investigate the relationship between two competition events that affect the relative abundance of complex I *vs.* complex II. The first competition event is the one between Atg14L and UVRAG for endogenous Beclin1, which was reported in our previous study (Wu *et al.*, 2018). The second is the one between NRBF2 and UVRAG for endogenous Vps15, which is the focus of my thesis. Our data show that the Atg14L *vs.* UVRAG competition plays a dominant role in terms of determining the relative abundance of complex I *vs.* complex II. This is because UVRAG mutants with weakened competitiveness against Atg14L also shows less binding to Vps15 in presence of NRBF2 over-expression. However, over-expression of NRBF2 does not benefit Atg14L in its competition against UVRAG for endogenous Beclin1.

Lastly, we tested the impact of the CC domain of NRBF2 on autophagy by transfecting monomeric, dimeric and tetrameric NRBF2 constructs into NRBF2 knockout cells and assessing its autophagic flux by monitoring autophagy marker p62. Our data show that monomeric NRBF2 is least effective in terms of rescuing the knockout phenotype while dimeric and tetrameric constructs lead to full recovery and even enhancement of the autophagy activity.

For works in future, the following aspects will be explored:

Based on our previous finding that MIT domain of NRBF2 is indispensable for its binding to Vps15, we plan to design a series of mutations at the MIT domain to probe the molecular mechanism of NRBF2-Vps15 interaction. Once the Vps15-binding sites on NRBF2-MIT have been identified, cell-based experiments will be conducted to investigate the effects of mutational perturbation of NRBF2-Vps15 interaction on regulating autophagy, including the colocalization of NRBF2 mutants to GFP-LC3 puncta and the degradation of endogenous p62. Besides, the liposome-binding assay will be applied to probe the roles of NRBF2 in regulating the lipids kinase activity.

In summary, my thesis work has provided additional structural and biochemical information to help understand the functional role of NRBF2 within the context of the Beclin1-Vps34 complex. Our data confirms that NRBF2 is a specific modulator of the Atg14L-containing complex I because NRBF2 and UVRAG are incompatible binding partners for Vps15. Additionally, the oligomeric state of NRBF2 as determined by its CC domain is critical for its function because it may facilitate the dimerization and even high-order assembly of complex I to promote the lipid kinase activity of Vps34.

Reference

Kiffin, R., Bandyopadhyay, U., and Cuervo, A. M. (2006) Oxidative stress and autophagy. *Antioxidants & redox signaling* **8**, 152-162

Meléndez, A., and Levine, B. (2009) Autophagy in C. elegans. *WormBook*. 10.1895/wormbook.1.147.1

Mathew, R., Karantza-Wadsworth, V., and White, E. (2007) Role of autophagy in cancer. *Nature Reviews Cancer* **7**, 961

White, E. (2012) Deconvoluting the context-dependent role for autophagy in cancer. *Nature Reviews Cancer* **12**, 401

Nakahira, K., and Choi, A. M. K. (2013) Autophagy: a potential therapeutic target in lung diseases. *Am J Physiol Lung Cell Mol Physiol* **305**, L93-L107

Wirth, M., Joachim, J., and Tooze, S. A. (2013) Autophagosome formation—The role of ULK1 and Beclin1–PI3KC3 complexes in setting the stage. *Seminars in Cancer Biology* **23**, 301-309

Jaber, N., and Zong, W.-X. (2013) Class III PI3K Vps34: essential roles in autophagy, endocytosis, and heart and liver function. *Annals of the New York Academy of Sciences* **1280**, 48-51

Anding, A. L., and Baehrecke, E. H. (2014) Vps15 is required for stress induced and developmentally triggered autophagy and salivary gland protein secretion in Drosophila. *Cell Death And Differentiation* **22**, 457

Kang, R., Zeh, H. J., Lotze, M. T., and Tang, D. (2011) The Beclin 1 network regulates autophagy and apoptosis. *Cell Death And Differentiation* **18**, 571

Zhong, Y., Wang, Q. J., Li, X., Yan, Y., Backer, J. M., Chait, B. T., Heintz, N., and Yue, Z. (2009) Distinct regulation of autophagic activity by Atg14L and Rubicon associated with Beclin 1–phosphatidylinositol-3-kinase complex. *Nature Cell Biology* **11**, 468

Kim, Y.-M., Jung, Chang H., Seo, M., Kim, Eun K., Park, J.-M., Bae, Sun S., and Kim, D.-H. (2015) mTORC1 Phosphorylates UVRAG to Negatively Regulate Autophagosome and Endosome Maturation. *Molecular Cell* **57**, 207-218

Rostislavleva, K., Soler, N., Ohashi, Y., Zhang, L., Pardon, E., Burke, J. E., Masson, G. R., Johnson, C., Steyaert, J., Ktistakis, N. T., and Williams, R. L. (2015) Structure and flexibility of the endosomal Vps34 complex reveals the basis of its function on membranes. *Science* **350**, aac7365

Baskaran, S., Carlson, L.-A., Stjepanovic, G., Young, L. N., Kim, D. J., Grob, P., Stanley, R. E., Nogales, E., and Hurley, J. H. (2014) Architecture and dynamics of the autophagic phosphatidylinositol 3-kinase complex. *Elife* **3**, e05115

Yasumo, H., Masuda, N., Furusawa, T., Tsukamoto, T., Sadano, H., and Osumi, T. (2000) Nuclear receptor binding factor-2 (NRBF-2), a possible gene activator protein interacting with nuclear hormone receptors11The present nucleotide sequence is available on the DDBJ/EMBL/GenBank databases with the accession number AB024930. *Biochimica et Biophysica Acta (BBA) - Gene Structure and Expression* **1490**, 189-197

Zhong, Y., Morris, D. H., Jin, L., Patel, M. S., Karunakaran, S. K., Fu, Y.-J., Matuszak, E. A., Weiss, H. L., Chait, B. T., and Wang, Q. J. (2014) Nrbf2 protein suppresses autophagy by modulating Atg14L protein-containing Beclin 1-Vps34 complex architecture and reducing intracellular phosphatidylinositol-3 phosphate levels. *J Biol Chem* **289**, 26021-26037

Cao, Y., Wang, Y., Abi Saab, W. F., Yang, F., Pessin, J. E., and Backer, J. M. (2014) NRBF2 regulates macroautophagy as a component of Vps34 Complex I. *Biochem J* **461**, 315-322

Lu, J., He, L., Behrends, C., Araki, M., Araki, K., Wang, Q. J., Catanzaro, J. M., Friedman, S. L., Zong, W.-X., and Fiel, M. I. (2014) NRBF2 regulates autophagy and prevents liver injury by modulating Atg14L-linked phosphatidylinositol-3 kinase III activity. *Nature communications* **5**, 3920

Young, L. N., Cho, K., Lawrence, R., Zoncu, R., and Hurley, J. H. (2016) Dynamics and architecture of the NRBF2-containing phosphatidylinositol 3-kinase complex I of autophagy. *Proceedings of the National Academy of Sciences* **113**, 8224

Ohashi, Y., Soler, N., García Ortegón, M., Zhang, L., Kirsten, M. L., Perisic, O., Masson, G. R., Burke, J. E., Jakobi, A. J., Apostolakis, A. A., Johnson, C. M., Ohashi, M., Ktistakis, N. T., Sachse, C., and Williams, R. L. (2016) Characterization of Atg38 and NRBF2, a fifth subunit of the autophagic Vps34/PIK3C3 complex. *Autophagy* **12**, 2129-2144

Young, L. N., Goerdeler, F., and Hurley, J. H. J. P. o. t. N. A. o. S. (2019)

Structural pathway for allosteric activation of the autophagic PI 3-kinase complex I. **116**, 21508-21513

Zhang, G., Annan, R. S., Carr, S. A., and Neubert, T. A. (2010) Overview of Peptide and Protein Analysis by Mass Spectrometry. *Current Protocols in Protein Science* **62**, 16.11.11-16.11.30

Jachimska, B., Wasilewska, M., and Adamczyk, Z. (2008) Characterization of Globular Protein Solutions by Dynamic Light Scattering, Electrophoretic Mobility, and Viscosity Measurements. *Langmuir* **24**, 6866-6872

Günther, H. (2013) *NMR spectroscopy: basic principles, concepts and applications in chemistry*, John Wiley & Sons

Hong, M., Zhang, Y., and Hu, F. (2012) Membrane protein structure and dynamics from NMR spectroscopy. *Annual review of physical chemistry* **63**, 1-24

Greenfield, N. J. (2006) Using circular dichroism spectra to estimate protein secondary structure. *Nat Protoc* **1**, 2876-2890

Pierce, M. M., Raman, C. S., and Nall, B. T. (1999) Isothermal Titration Calorimetry of Protein–Protein Interactions. *Methods* **19**, 213-221

Newman, J. R., and Keating, A. E. (2003) Comprehensive identification of human bZIP interactions with coiled-coil arrays. *Science* **300**, 2097-2101

Lovatt, M., Cooper, A., and Camilleri, P. (1996) Energetics of cyclodextrin-induced dissociation of insulin. *European biophysics journal* **24**, 354-357

Leslie, A. G. J. A. C. S. D. B. C. (2006) The integration of macromolecular

diffraction data. **62**, 48-57

Evans, P. J. A. C. S. D. B. C. (2006) Scaling and assessment of data quality. **62**, 72-82

Adams, P. D., Grosse-Kunstleve, R. W., Hung, L.-W., Ioerger, T. R., McCoy, A. J., Moriarty, N. W., Read, R. J., Sacchettini, J. C., Sauter, N. K., and Terwilliger, T. C. J. A. C. S. D. B. C. (2002) PHENIX: building new software for automated crystallographic structure determination. **58**, 1948-1954

McCoy, A. J., Grosse-Kunstleve, R. W., Adams, P. D., Winn, M. D., Storoni, L. C., and Read, R. J. J. J. o. a. c. (2007) Phaser crystallographic software. **40**, 658-674

Murshudov, G. N., Vagin, A. A., and Dodson, E. J. J. A. C. S. D. B. C. (1997) Refinement of macromolecular structures by the maximum-likelihood method. **53**, 240-255

Emsley, P., and Cowtan, K. J. A. C. S. D. B. C. (2004) Coot: model-building tools for molecular graphics. **60**, 2126-2132

Park, J.-M., Jung, C. H., Seo, M., Otto, N. M., Grunwald, D., Kim, K. H., Moriarity, B., Kim, Y.-M., Starker, C., Nho, R. S., Voytas, D., and Kim, D.-H. (2016) The ULK1 complex mediates MTORC1 signaling to the autophagy initiation machinery via binding and phosphorylating ATG14. *Autophagy* **12**, 547-564

Wold, M. S., Lim, J., Lachance, V., Deng, Z., and Yue, Z. (2016) ULK1-mediated phosphorylation of ATG14 promotes autophagy and is impaired in

Huntington's disease models. *Molecular Neurodegeneration* **11**, 76

Li, X., He, L., Che, K. H., Funderburk, S. F., Pan, L., Pan, N., Zhang, M., Yue, Z., and Zhao, Y. (2012) Imperfect interface of Beclin1 coiled-coil domain regulates homodimer and heterodimer formation with Atg14L and UVRAG. *Nature communications* **3**, 662

Wu, S., He, Y., Qiu, X., Yang, W., Liu, W., Li, X., Li, Y., Shen, H.-M., Wang, R., and Yue, Z. (2018) Targeting the potent Beclin 1–UVRAG coiled-coil interaction with designed peptides enhances autophagy and endolysosomal trafficking. *Proceedings of the National Academy of Sciences* **115**, E5669-E5678

Ma, X., Zhang, S., He, L., Rong, Y., Brier, L. W., Sun, Q., Liu, R., Fan, W., Chen, S., and Yue, Z. (2017) MTORC1-mediated NRBF2 phosphorylation functions as a switch for the class III PtdIns3K and autophagy. *Autophagy* **13**, 592-607

Funderburk, S. F., Wang, Q. J., and Yue, Z. (2010) The Beclin 1–VPS34 complex – at the crossroads of autophagy and beyond. *Trends in Cell Biology* **20**, 355-362

Ohashi, Y., Soler, N., García Ortegón, M., Zhang, L., Kirsten, M. L., Perisic, O., Masson, G. R., Burke, J. E., Jakobi, A. J., and Apostolakis, A. A. J. A. (2016) Characterization of Atg38 and NRBF2, a fifth subunit of the autophagic Vps34/PIK3C3 complex. **12**, 2129-2144

Wu, S., He, Y., Qiu, X., Yang, W., Liu, W., Li, X., Li, Y., Shen, H.-M., Wang,

R., and Yue, Z. J. P. o. t. N. A. o. S. (2018) Targeting the potent Beclin 1–UVRAG coiled-coil interaction with designed peptides enhances autophagy and endolysosomal trafficking. **115**, E5669-E5678